



저작자표시-비영리-변경금지 2.0 대한민국

이용자는 아래의 조건을 따르는 경우에 한하여 자유롭게

- 이 저작물을 복제, 배포, 전송, 전시, 공연 및 방송할 수 있습니다.

다음과 같은 조건을 따라야 합니다:



저작자표시. 귀하는 원저작자를 표시하여야 합니다.



비영리. 귀하는 이 저작물을 영리 목적으로 이용할 수 없습니다.



변경금지. 귀하는 이 저작물을 개작, 변형 또는 가공할 수 없습니다.

- 귀하는, 이 저작물의 재이용이나 배포의 경우, 이 저작물에 적용된 이용허락조건을 명확하게 나타내어야 합니다.
- 저작권자로부터 별도의 허가를 받으면 이러한 조건들은 적용되지 않습니다.

저작권법에 따른 이용자의 권리는 위의 내용에 의하여 영향을 받지 않습니다.

이것은 [이용허락규약\(Legal Code\)](#)을 이해하기 쉽게 요약한 것입니다.

[Disclaimer](#)

공학박사 학위논문

Development of Plasma Information  
Based Virtual Metrology (PI-VM) for  
Drifting Deposition Process

플라즈마 정보기반의 표류증착공정용  
가상계측방법론 개발

2018년 8월

서울대학교 대학원

에너지시스템공학부

노 현 준

## **Abstract**

# **Development of Plasma Information Based Virtual Metrology (PI-VM) for Drifting Deposition Process**

Hyun-Joon Roh

Department of Energy Systems Engineering  
The Graduate School  
Seoul National University

In semiconductor-fabrication industry, virtual metrology (VM) is one of promising technology to achieve advanced process control (APC) for plasma-assisted process because it can provide metrology data for every wafer. VM is defined as the technology of prediction of metrology variables using process state (equipment and sensor) and wafer state variables. However, prediction reliability of VM is very sensitive to the quality of data and the selection of data mining technique, causing the limitation of its APC applications. Also, the required prediction reliability of VM is getting higher as the critical dimension of semiconductor devices sharply shrinks. In line with this trend, development of phenomenological-based VM

which includes information about the plasma-assisted process reactor is important in the sophisticated control of semiconductor and display device manufacturing. Note that reactor is defined as process vessels that are used in semiconductor manufacturing industries for carrying out chemical reactions with assistance of plasma.

The wafer state variables of plasma-assisted process, especially plasma-enhanced chemical vapor deposition (PECVD), are governed by the influx of reactive species on wafer, such as radicals, metastables, and ions. These influxes are mainly produced by electron-impact collision reactions with collision partners and destructed by reactions at reactor-wall. Thus, the wafer state variables are complex function of electron-energy distribution function (EEDF) which governs reaction rate constant ( $\text{m}^3\text{s}^{-1}$ ) in plasma-volume, and reactor-wall condition which governs reaction rate at reactor-wall, such as recombination probability.

The plasma-assisted process often drifts with the operation time caused from the phenomena related to the gradual deposition of byproducts or fragments of feedstock gas on reactor-wall. This drift of reactor-wall condition changes the flux of reactive species through the desorption of residues or deactivation of reactive species at reactor-wall. It also changes the gas composition in plasma and EEDF through additional elastic and inelastic collision processes. The changed EEDF induces the variation of influx of reactive species. Therefore, the reliable VM should include the variables that represent EEDF and reactor-wall condition. This concern is important specifically for the long-term application of VM.

In this dissertation, two plasma-information (PI) variables are defined as the state variables of plasma-assisted processes affecting the flux of reactive species: Monitoring variable for reactor-wall condition (named  $\text{PI}_{\text{wall}}$ ) which represents the film buildup on reactor-wall, and another variable for plasma-volume (named  $\text{PI}_{\text{volume}}$ ) which corresponds to electron density and electron temperature (or EEDF). These PI variables are determined by using plasma spectroscopy which analyzes the optical emission spectra based on the excitation equilibria in

plasma.  $PI_{\text{wall}}$  is determined by analyzing the light transmittance at the contaminated window based on line-intensity ratios from the same upper energy level. In the development of  $PI_{\text{wall}}$ , it is assumed that the film deposition on quartz window is roughly following that of reactor-wall surface.  $PI_{\text{volume}}$  is determined by analyzing line-intensity ratios from different upper energy levels based on collisional-radiative model (CRM).

The evaluation of influence of each variable on PI-VM for single-layer nitride PECVD shows that the electron density affects the formation of N containing species through governing the collision reaction with low threshold energy. It also shows that the electron temperature affects the formation of Si containing species through electron-impact collisions with high threshold energy. Meanwhile,  $PI_{\text{wall}}$  affects the formation of N containing species, especially near the reactor-wall.

PI-VM is applied to predict layer-to-layer nitride film thickness in nitride/oxide multi-layer PECVD used for 3D NAND fabrication in the mass production line. The evaluation of influence of each variable on PI-VM demonstrates that  $PI_{\text{wall}}$  is the highest contributing variable in whole layers and  $PI_{\text{volume}}$  contributes in the latter region of layers. In the trend of increasing the number of nitride/oxide layers to increase device density, PI-VM offers provide the key phenomena of plasma to be managed. Therefore, PI-VM is expected to provide the fundamentals to develop advanced process control (APC) and fault detection and classification (FDC) for plasma-assisted processes. Also, it provides the way to apply the plasma spectroscopy in the basic plasma diagnostics technology to plasma-assisted process.

**Keywords:** plasma-information, reactor-wall condition, optical emission spectroscopy (OES), virtual metrology (VM), plasma-enhanced chemical vapor deposition (PECVD).

**Student ID:** 2011-21094

# Contents

<b>Abstract.....</b>	<b>i</b>
<b>Contents .....</b>	<b>iv</b>
<b>List of Tables.....</b>	<b>vii</b>
<b>List of Figures.....</b>	<b>viii</b>
<b>Chapter 1 . Introduction.....</b>	<b>1</b>
1.1 Virtual metrology (VM) for plasma-assisted processes of semiconductor manufacturing.....	1
1.2 Degradation of VM reliability due to absence of view on the drift of plasma-assisted process.....	2
<b>Chapter 2 . Objectives and Strategy .....</b>	<b>6</b>
<b>Chapter 3 . Development of PI-VM to Predict the Property of Deposited Film in Plasma-enhanced</b>	

<b>Chemical Vapor Deposition (PECVD) .....</b>	<b>1 1</b>
<b>3.1 Procedure of PI-VM development.....</b>	<b>1 1</b>
<b>3.2 Experimental setups.....</b>	<b>1 4</b>
<b>Chapter 4 . Determination of PI Variables by Using</b>	
<b>Plasma Spectroscopy.....</b>	<b>2 4</b>
<b>4.1 Plasma spectroscopy .....</b>	<b>2 4</b>
<b>4.2 Relative calibration of the spectroscopic system .....</b>	<b>2 8</b>
<b>4.3 Selection criteria of emission lines and reaction data .....</b>	<b>3 1</b>
<b>4.4 Development of monitoring variable for reactor-wall condition..</b>	<b>3 4</b>
<b>4.5 Development of monitoring variable for plasma-volume .....</b>	<b>4 8</b>
<b>Chapter 5 . Application of PI-VM to Predict the</b>	
<b>Property of Nitride Film .....</b>	<b>6 4</b>
<b>5.1 PI-VM for nitride film in single-layer PECVD .....</b>	<b>6 5</b>
<b>5.2 PI-VM for the nitride film in multi-layer PECVD .....</b>	<b>7 5</b>
<b>Chapter 6 . Conclusion.....</b>	<b>8 2</b>
<b>Appendix A: Theoretical background of plasma</b>	
<b>spectroscopy .....</b>	<b>8 4</b>

A.1 Atomic and molecular energy levels.....	8 4
A.2 Excitation equilibria in plasmas.....	9 1
<b>Appendix B: Diagnostics of <math>PI_{Volume}</math> in non-Maxwellian</b>	
<b>plasmas.....</b>	<b>9 6</b>
B.1 Analytical EEDF functions.....	9 6
B.2 Argon CRM.....	1 0 0
B.3 Diagnostics of tail-depleted EEDF.....	1 0 7
B.4 Diagnostics of tail-enhanced EEDF.....	1 1 3
<b>Bibliography.....</b>	<b>1 2 7</b>
<b>초    록.....</b>	<b>1 4 0</b>

## List of Tables

Table 3-1. Experimental setups. LP means Langmuir probe, THK means film thickness, $n$ means refractive index, and L2L means layer-to-layer. ....	1 5
Table 3-2. Process recipe of single-layer PECVD. Heater temperature was maintained at 400°C. Dry CLN means dry cleaning step.....	1 7
Table 3-3. Process recipe of multi-layer PECVD for coupon test. All step has 10-20 mm gap size between electrode and 2-4 Torr operating pressure. The frequency of remote source was 400 kHz and that of CCP was 13.56 MHz. For oxide PECVD, 370 kHz power was additionally applied to top electrode. ....	2 2
Table 3-4. Coupon test condition .....	2 2
Table 4-1. Information about line-intensities used to monitor the wavelength-dependent transmittance on window. $\lambda$ is wavelength, and $A_{pk}$ is the radiative decay coefficient. All information is based on [42] .....	3 9
Table 4-2. Information about line-intensities used to monitor $PI_{\text{volume}}$ . Headings are the same as for Table 4-1. Again, all information is based on [42].....	5 2
Table 4-3. Used reaction rates for $N_2$ CRM.....	5 7
Table 5-1. Monitored line-intensities to develop PI-VM for single-layer nitride PECVD. .	6 8
Table 5-2. Performance evaluation of PI-VM for single-layer nitride PECVD.....	6 9
Table 5-3. Determined variables set depending on the inclusion on PI variables. $Z$ means magnitude of impedance measured at RF matcher. ....	7 7
Table 5-4. Performance evaluation of PI-VM for multi-layer nitride PECVD.....	7 9

## List of Figures

Figure 2-1. The scope of reactor for plasma-assisted process in this dissertation. The reactor for plasma-assisted process consists of plasma and reactor-wall the forms the boundary condition. Plasma-information (PI) variables are composed of reactor-wall monitoring variable (named  $PI_{Wall}$ ) which represents the film buildup on reactor-wall and plasma volume monitoring variable (named  $PI_{Volume}$ ) which represents the electron-impact collision reactions in plasma. PI-VM is constructed by implementing PI variables on VM. Here,  $V$  is the discharge volume;  $A$  is area for particle loss;  $n_{gas}$  is density of neutral gas;  $\sigma$  is collision cross section;  $v_e$  is electron speed;  $n_e$  is electron density;  $f(E)$  is EEDF;  $E$  is electron energy;  $T_e$  is electron temperature for Maxwellian EEDF;  $K_{desorp.}$  is desorption rate constant;  $n_{residue}$  is surface density of film deposition on reactor-wall;  $A_0$  is effective diffusion length;  $D_0$  is neutral diffusion coefficient;  $\gamma$  is surface loss probability;  $\bar{v}i$  is average speed of reactive species;  $s_i$  is sticking coefficient;  $M_i$  is mass of reactive species;  $\rho_i$  is mass density of film; and  $R$  is reaction rate on wafer which is proportional to flux of reactive species ( $1/4n_i\bar{v}i$ );..... 9

Figure 2-2. Comparison of the mechanism for gradual film deposition on reactor wall. a) Si etch plasma. b)  $SiN_xH_y$  deposition plasma ..... 1 0

Figure 2-3. Experimental verification procedure to develop PI-VM. Here, THK means film thickness, and  $n$  means refractive index. .... 1 0

Figure 3-1. Flow chart of PI-VM development. Selections of PI variables, their parametrization method, and a regression model are required to develop PI-VM..... 1 2

Figure 3-2. Experimental condition of helicon plasma. a) Schematic diagram of the helicon plasma. Magnetic coil was excluded in figure to improve visibility. b) Measured electron

density. c) Measured electron temperature. ....	1 4
Figure 3-3. Schematic of narrow-gap capacitively coupled plasma (CCP) for single-layer PECVD. ....	1 7
Figure 3-4. Measurement position of single-layer PECVD by using ellipsometry. ....	1 8
Figure 3-5. Schematic of narrow-gap capacitively coupled plasma (CCP) for multi-layer PECVD. ....	1 9
Figure 3-6. Process sequence of multi-layer PECVD. ....	2 0
Figure 3-7. Measurement of wafer state variables (wafer #175). (a) STEM image for the thickness representing the sets of the nitride and oxide layers. (b) EDS analysis for oxygen fraction at the first nitride layer on wafer. The shaded area shows the existence of oxynitride film at the first nitride layer on wafer. ....	2 1
Figure 4-1. Calibrated spectral irradiance of deuterium-halogen light source. a) Halogen light source (Wolfram Halogen 6390-DZA). b) Deuterium-halogen light source (Deuterium DOS 650 TJ). ....	2 8
Figure 4-2. Measured emission intensity of deuterium-halogen lamp. a) Halogen light source. b) Deuterium-halogen light source. 2-channel spectrometers (AvaSepc-2048 & AvaSpec-3648) was used. ....	2 9
Figure 4-3. Conversion factor for 2-channel spectrometers (AvaSepc-2048 & AvaSpec-3648). ....	3 0
Figure 4-4. Line-intensities used to monitor the wavelength-dependent transmittance on window. Among $N_2$ SPS, emissions from $N_2(C^3\Pi_u, \nu = 0)$ and $N_2(C^3\Pi_u, \nu = 1)$ are used, because they have relatively large intensity providing reasonable SNR. ....	3 7
Figure 4-5. Comparison of measured $N_2$ emission spectrum. a) Helicon ( $N_2$ 5 mTorr, 13.56 MHz 800 W). b) Single-layer PECVD (4 Torr, 13.56 MHz 720 W, $N_2$ 3000sccm). c) Multi-layer PECVD (Wafer #175, layer 1). ....	4 0

Figure 4-6. Validation of transmittance monitoring model at clean quartz window. (Helicon) The error bar is standard deviation of measured transmittance for all pressure and power variation condition in Table 3-1. The inserted graph shows the transmittance of a typical quartz window ( <a href="https://www.janis.com">https://www.janis.com</a> ).....	4 1
Figure 4-7. Superposition of N <sub>2</sub> SPS and N <sub>2</sub> FNS. a) Emission spectrum of helicon plasma between 350 nm and 360 nm (N <sub>2</sub> 5 mTorr, 13.56 MHz 800 W). b) Normalized intensity ratio between 357.6 nm and 337.0 nm. Here, only peak intensities of 357.6 nm and 337.0 nm are used without deconvolution.....	4 2
Figure 4-8. Normalized intensity ratio to evaluate the influence of radiation trapping on N <sub>2</sub> SPS (Helicon).....	4 3
Figure 4-9. Transmittance monitoring at contaminated quartz window. (Multi-layer PECVD) The error bar is standard deviation of measured transmittance with in a nitride PECVD. ...	4 4
Figure 4-10. STEM image for coupons established at reactor wall. a) Bare Al coupon before PECVD. b) deposited coupon after pre-coating process. c) Deposited coupon after 14 pairs nitride/oxide PECVD.....	4 5
Figure 4-11. EDS data for the deposited coupon after 14 pairs nitride/oxide PECVD.....	4 5
Figure 4-12. Analysis of STEM data. a) Composition of film on reactor wall when 14 pairs nitride/oxide layers are deposited. b) Variation of film thickness on reactor wall. ....	4 6
Figure 4-13. Correlation between $PI_{Wall}$ and $F_O$ of equation (3.5). (b) Variation of $PI_{Wall}$ with increasing layer and wafer number. The vertical dash lines are inserted to distinguish each wafer. ....	4 7
Figure 4-14. Partial diagram of potential energy curves of molecular nitrogen [44]. $R$ means internuclear distance.....	4 9
Figure 4-15. Partial energy diagram for the first vibrational state of each electronic state [56]. a) N <sub>2</sub> . b) N <sub>2</sub> <sup>+</sup> . FPS = first positive system, SPS = second positive system, 4.PG = fourth positive	

system, VK = Vegard–Kaplan system, IRA = infrared afterglow system, WB = Wu–Benesch system, HK = Herman–Kaplan system, GK = Goldstein–Kaplan system, GHG = Gaydon–Herman Green system, HIR = Herman infrared system, LBH = Lyman–Birge–Hopfield. FNS = first negative system, SNS = second negative system, JI = Janin–d’Incan system and MA = Meinel’s auroral system. Radiative transitions important for optical diagnostics are highlighted in blue..... 5 0

Figure 4-16. Wavelengths of N<sub>2</sub> SPS to determine PI<sub>Volume</sub>. ..... 5 2

Figure 4-17. Flow chart of N<sub>2</sub> CRM to determine PI variables. .... 5 3

Figure 4-18. Determination of PI<sub>Volume</sub> by using N<sub>2</sub> CRM for 1<sup>st</sup> layer at wafer #175. a) Determined VDF by using emission model. b) Percentage of production for each vibrational state. ‘eV’, ‘eA’, and ‘AA’ represent electron-impact excitation from ground state, that from metastable state, and metastable pooling reaction, respectively. .... 6 2

Figure 5-1. Measured emission spectrum of deposition step in single-layer nitride PECVD (4 Torr, 13.56 MHz 720 W, and N<sub>2</sub> 3000sccm). ..... 6 5

Figure 5-2. Measured emission spectrum of cleaning step in single-layer nitride PECVD. 6 6

Figure 5-3. Wafer state variables depending on process condition. a) power scan. b) pressure scan. c) N<sub>2</sub> flow rate scan. d) deposition time scan. Values in figure are wafer-averaged. Detailed recipes are shown in Table 3-2. .... 6 7

Figure 5-4. Uniformity of wafer state variables depending on process condition. a) power scan. b) pressure scan. c) N<sub>2</sub> flow rate scan. d) deposition time scan. Values in figure are normalized by that of wafer center position. .... 6 7

Figure 5-5. Prediction result of PI-VM for single-layer PECVD. Black rectangles and red circles represent measured and predicted property of nitride film, respectively. a) Mean thickness. b) Mean refractive index. c) Uniformity of thickness. d) Uniformity of refractive index. The vertical dash lines are inserted to distinguish condition of recipe scan. .... 7 0

Figure 5-6. Contribution of variables on wafer state. a) Contribution on mean nitride thickness. b) Contribution on mean refractive index..... 7 2

Figure 5-7. Contribution of variables on the uniformity of wafer state. a) Contribution on the uniformity of nitride thickness. b) Contribution on the uniformity of refractive index. .... 7 3

Figure 5-8. Influence of reactor wall condition on the uniformity of nitride film. a) W2W variation of  $PI_{Wall}$  depending on wafer number. b) W2W variation of uniformity depending on wafer number. The plotted data was originated from the deposition time scan recipe. .... 7 4

Figure 5-9. L2L and W2W variation of nitride film thickness (wafer state variable). The vertical dash lines are inserted to distinguish each wafer. The error bar in the measured thickness originates from the pixel resolution of STEM image. .... 7 5

Figure 5-10. L2L and W2W variation of wafer and process state variables. a) measured film thickness. b)  $PI_{Wall}$ . c) Tune position of matcher. d) VAT position. e) Electron density. f) Electron temperature. g) Resistance measured at matcher. h) Load position of matcher. The figures were sorted in descending order of correlation with measured film thickness. .... 7 6

Figure 5-11. Comparison of three VM models. Black rectangles show the measured thickness. Red circles, green upper triangles, and blue lower triangles represent  $VM_{Equipment}$ ,  $PI_{Wall}$ -VM, and  $PI_{Total}$ -VM, respectively. The vertical dash lines are inserted to distinguish each wafer. The error bar in the measured thickness originates from the pixel resolution of STEM image. . 7 8

Figure 5-12. Performance evaluation of VM models. (a) Comparison of  $R^2$  and  $Q^2$  depending on the inclusion of PI variables on VM. A value larger than 0.5 represents a sound VM model. (b) Variable influence on projection (VIP) of  $PI$ - $VM_{Total}$ . A VIP larger than 0.8 means that the variable is important. .... 8 0

Figure 5-13.  $R^2$  of VM Models depending on the region of layers. Left figure:  $R^2$  of the first half-layers; right figure:  $R^2$  of the remaining half-layers. .... 8 1

# Chapter 1 . Introduction

## 1.1 Virtual metrology (VM) for plasma-assisted processes of semiconductor manufacturing

As the critical dimension of semiconductor devices sharply decreases to nanoscale, subtle distortion of plasma due to variation in the environment of process reactor can cause deviation of wafer state variables, such as etch depth and deposited film thickness. In line with this situation where more precise control of plasma-assisted process is required than in the past, advanced process control (APC) in wafer-to-wafer (W2W) scale is regarded as the next step in factory automation to assure a high quality and throughput [1].

In semiconductor equipment and materials international (SEMI) standard, APC is defined as the manufacturing discipline for applying control strategies and/or employing analysis and computation mechanisms to recommend optimized machine settings and detect faults and determine their cause [2]. APC includes the following techniques: run-to-run (R2R) control, fault detection (FD), fault classification (FC), fault prediction (FP), statistical process control (SPC). Ideally, APC can be achieved by using measured wafer state (metrology variable), desired results and information about the substrate to be processed (pre-metrology variable). Thus, it is necessary the measured metrology variables to develop the APC.

Practically, APC for plasma-assisted process has been implemented based on lot-to-lot control, where a lot is composed of up to 25 wafers, since direct metrology (DM) can measure only 1–3 wafers per a lot due to a slow time response and high cost of metrology tools [1]. Therefore, a method to measure the metrology variables for every wafer are required to cope

with drift or deviation of wafer state variable in W2W scale.

As a potential solution, virtual metrology (VM) is defined as the prediction of metrology variables using process state (equipment and sensor variables) and wafer state variables [3]. Equipment variables are defined as chamber-related process variables such as temperature, pressure, gas flows, and power which are collected from built-in sensors [4]. Also, sensor variables are defined as the variables collected from additional sensors such as optical emission spectroscopy (OES), plasma impedance monitors (PIMs) [4]. Therefore, VM has potential to improve process control because the metrology variables for every wafer can be predicted by using process state variables after constructing VM model.

However, the prediction reliability of VM should be guaranteed to successfully implement VM for APC applications [5]. The prediction reliability should also be maintained for a long time to apply APC over a wide range of time scale, from W2W to within preventative maintenance (PM) cycle or between other PM cycles.

## **1.2 Degradation of VM reliability due to absence of view on the drift of plasma-assisted process**

The wafer state variables of plasma-assisted process, especially plasma-enhanced chemical vapor deposition (PECVD), are governed by the influx of reactive species on wafer, such as radicals, metastables, and ions. This influx is mainly determined by electron-impact collision reactions with collision partners, such as feedstock gas, byproducts, or residues. Thus, the wafer state variables are complex function of electron-energy distribution function (EEDF) which governs reaction rate constant ( $\text{cm}^3\text{s}^{-1}$ ), and reactor-wall condition which act as loss

boundary of reactive species. Also, the behavior of plasma-assisted process drifts with the operation time due to gradual deposition of byproducts or fragments of feedstock gas on reactor-wall. This well-known drift of reactor-wall condition changes the flux of reactive species through the desorption of residues or deactivation of reactive species at reactor-wall. It also changes EEDF by affecting gas phase chemistry in plasma, resulting in a secondary variation of flux of reactive species. Thus, implementation of first-principle or simulation techniques on VM is practically impossible, because the complicate modeling for process-reactor requires much calculation time.

Instead, many studies have developed empirical prediction model using raw data sets of process state and wafer state variables, by regarding the plasma-assisted process reactor as black-box. Principal-component-analysis (PCA) and stepwise-selection methods are commonly adopted for the statistical selection of variables [6-8]. Also, the prediction models have been developed that are divided into *linear models* and *nonlinear models*. The typical linear models are principal component regression (PCR) and partial least squares regression (PLSR) [9]. For the nonlinear models, artificial neural network (ANN), Gaussian process regression (GPR), and support vector machine (SVM) have been developed [10-13]. Also, the ensemble methods, such as importance sampling and rules ensembles, have been developed to obtain better prediction accuracy by combining multiple models into one [14]. However, as required prediction reliability of VM is getting higher with shrinking device size, these models have problems with prediction reliability that fail to satisfy the required reliability from industry [15] or degrade over time according to the drift of process reactor [16]. In line with this trend, implementation of domain knowledge on VM or development of phenomenological-based VM which includes information about the environment of process reactor is important in plasma-assisted process.

In recent years, a phenomenological-based process diagnostic technique has been

proposed that makes novel variables, named plasma-information (PI) variables to represent the state of the plasma-assisted process [15]. These PI variables was obtained from the analysis of OES under the consideration of reactions in plasma volume, sheath, and wafer. Then, PI-VM was developed to predict etch rate in the oxide etch process by adopting PCR as regression model. Here, PI-VM is defined as VM model whose input variables are composed of PI, OES and equipment variables. This work demonstrated the drastic enhancement of prediction accuracy because PI variables can present the nature of plasma assisted process. However, PI-VM still contains the problem of degradation of prediction reliability due to the lack of monitoring method for reactor-wall condition [17]. Also, there is a limit to the use of PI-VM for monitoring technology for plasma-assisted process, because it cannot correct the distortion of OES spectrum due to contamination of window which is one of major cause to limit the application of OES analysis technology to plasma-assisted processes.

Some novel sensor techniques have been developed to monitor reactor-wall condition. *Anna et al.* developed an optical method based on Multiple Total Internal Reflection-Fourier Transform Infrared (MTIR-FTIR) spectroscopy [18]. This method measured the properties of thin films deposited on internal reflection crystal (IRC) installed near the reactor-wall. The thickness was then measured using an infrared (IR) beam and a Fourier Transform Infrared (FTIR) spectrometer. *Kim et al.* proposed a method to monitor the thickness of a dielectric film on the floated planar-type probe near the reactor-wall by applying the two frequencies of sinusoidal voltage signals on the probe [19]. However, these methods have some limitation to adopt in process monitoring technology because they require the invasive sensor components.

In statistics, alternative indirect methods were developed by adapting a model-update strategy. Specifically, moving-window-based VM model were proposed by *A. A. Khan* and *J. R. Moyne* [5]. Also, divide-and-conquer model, such as the growing structure multiple model system (GSMMS) [20], have been proposed and a set of linear models was employed

to describe the nonlinear dynamic dependency of the reactor-wall condition. However, these methods require a large computing power to recalculate VM, limiting their applications in practical usage.

To maintain prediction reliability in the long time, VM should contain phenomenological variables which can monitor the drift of reactor-wall and plasma volume individually. Therefore, the non-invasive method for these phenomenological variables should be developed by interpreting equipment or sensor variables based on its physical mechanism.

## Chapter 2 . Objectives and Strategy

This dissertation develops the framework of VM using PI variables as input variables (defined as PI-VM) to recognize the process drift by determining PI variables with adaption of plasma spectroscopy. PI variables are defined as the environmental factors of plasma-assisted processes affecting the flux of reactive species. Figure 2-1 shows the scope of reactor for plasma-assisted process defined as process vessels that are used in semiconductor manufacturing industries for carrying out chemical reactions with assistance of plasma [21]. The reactor for plasma-assisted process consists of plasma and reactor-wall the forms the boundary condition for reactive species. The reactor-wall condition can drift with increase of deposition of byproducts or fragments of feedstock gas on reactor-wall. This well-known drift of reactor-wall condition changes the flux of reactive species through the desorption of residues or deactivation of reactive species at reactor-wall. It also changes EEDF by affecting gas phase chemistry in plasma, resulting in a secondary variation of flux of reactive species ( $R$  in Figure 2-1) through electron-impact collision reactions.

Therefore, plasma-information (PI) variables are composed of reactor-wall monitoring variable (named  $PI_{\text{Wall}}$ ) which represents the film buildup on reactor-wall and plasma volume monitoring variable (named  $PI_{\text{Volume}}$ ) which corresponds to electron density and electron temperature (or EEDF) representing the electron-impact collision reactions in plasma. These PI variables are individually monitored with adaption of plasma spectroscopy considering the excitation equilibria in plasma.  $PI_{\text{Wall}}$  is monitored by determining the light transmittance at the contaminated quartz window through line-intensity ratios from same upper energy level. In the development of  $PI_{\text{Wall}}$ , it is assumed that the film deposition on quartz window near

reactor-wall is roughly following that of reactor-wall surface.  $PI_{\text{Volume}}$  is determined by analyzing line-intensity ratios from different upper energy levels based on collisional-radiative model (CRM), after correcting the effect of window contamination. CRM determines  $PI_{\text{Volume}}$  by reversing the fact that the contributions of excitation reactions, such as electron-impact and heavy-particle collisions, are different depending on the energy level.

To evaluate the feasibility of the concept of PI-VM, specific plasma-assisted process should be selected to verify the performance of PI-VM. The two criteria for selecting the target plasma-assisted process are as follows: (1) The process with sufficient drift of reactor-wall condition should be selected to represent the plasma-assisted process where the behavior drifts with the operation time. (2) The process contains specific gas which have reliable reaction cross section about electron-impact and heavy-particle collisions to assure the reliability of plasma spectroscopy.

Figure 2-2 shows the mechanism of film deposition on reactor-wall for plasma-assisted etch and deposition process. In the etching process, dissociated or ionized fragments from the byproducts of etching reaction are deposited on the reactor-wall. On the other hand, in the deposition process, the deposition reaction occurs with the same mechanism both on the wafer and reactor-wall, although there is a difference of deposition reaction 'rate'. That is, PECVD process generally has larger amount of deposition on reactor wall than that of etching process. Among PECVD, silicon nitride/oxide multi-layer PECVD, the first step in 3D-NAND flash-memory fabrication, is one of most notorious drifting process. This process has not only wafer-to-wafer (W2W) drift in PM cycle as other processes, but also layer-to-layer (L2L) drift in single wafer. It is originated from that nitride/oxide pair is deposited alternatively in a chamber without dry-cleaning and pre-coating processes for a certain period. Also, silicon nitride PECVD (nitride PECVD) has advantage over other PECVD processes for the 2<sup>nd</sup> criteria, since it generally contains  $N_2$  gas as feed gas.  $N_2$  gas has been used for a long time in

plasma discharge, and many researchers have studied to obtain reliable set of reaction cross sections. Therefore, this dissertation develops PI-VM for silicon nitride PECVD in multi-layer PECVD as representative plasma-assisted process where the behavior drifts with the operation time.

The framework of PI-VM will be proven as following experimental verification procedure (Figure 2-3). Firstly, the monitoring reasonability of PI variables is validated by using the laboratory plasmas which have clean quartz window. The methodologies for determining non-Maxwellian EEDF are verified by using inductive coupled plasma (ICP) for tail-depleted EEDF and very-high-frequency capacitive plasma (VHF-CCP) for tail-enhanced EEDF (Appendix B). Here, argon atomic emission lines are analyzed by considering excitation kinetics in plasma (Appendix A). Also, the methodologies for determining Maxwellian EEDF and  $PI_{\text{wall}}$  are verified by using helicon plasma. Here, nitrogen molecular emission lines are analyzed by considering additional degree of freedom, vibrational distribution function (VDF). Secondly, the meaning of PI variables on the formation of nitride film in single-layer PECVD is interpreted by constructing VM models using PI variables (named PI-VM) for thickness and refractive index (Applied Materials, P-5000). Finally, the concept of PI-VM is applied to predict layer-to-layer nitride film thickness in nitride/oxide multi-layer PECVD used for 3D NAND fabrication in the mass production line (Wonik IPS, MAHA). Graphs in Figure 2-3 will be discussed in chapter 4 and 5.

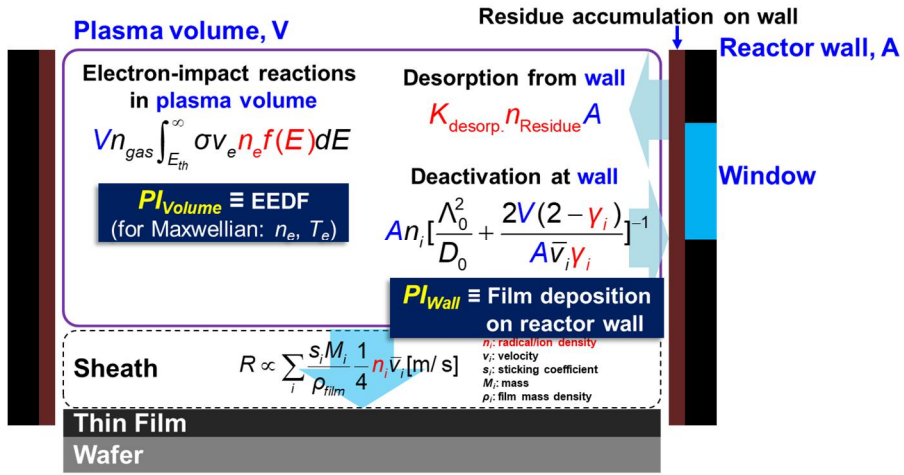


**Figure 2-1.** The scope of reactor for plasma-assisted process in this dissertation. The reactor for plasma-assisted process consists of plasma and reactor-wall the forms the boundary condition. Plasma-information (PI) variables are composed of reactor-wall monitoring variable (named PI<sub>Wall</sub>) which represents the film buildup on reactor-wall and plasma volume monitoring variable (named PI<sub>Volume</sub>) which represents the electron-impact collision reactions in plasma. PI-VM is constructed by implementing PI variables on VM. Here,  $V$  is the discharge volume;  $A$  is area for particle loss;  $n_{\text{gas}}$  is density of neutral gas;  $\sigma$  is collision cross section;  $v_e$  is electron speed;  $n_e$  is electron density;  $f(E)$  is EEDF;  $E$  is electron energy;  $T_e$  is electron temperature for Maxwellian EEDF;  $K_{\text{desorp.}}$  is desorption rate constant;  $n_{\text{residue}}$  is surface density of film deposition on reactor-wall;  $\Lambda_0$  is effective diffusion length;  $D_0$  is neutral diffusion coefficient;  $\gamma$  is surface loss probability;  $\bar{v}_i$  is average speed of reactive species;  $s_i$  is sticking coefficient;  $M_i$  is mass of reactive species;  $\rho_i$  is mass density of film; and  $R$  is reaction rate on wafer which is proportional to flux of reactive species ( $1/4 n_i \bar{v}_i$ );



**Si etch (Ar/Cl<sub>2</sub> plasma):**  
Residue accumulation due to **byproducts**

**Nitride PECVD (SiH<sub>4</sub>/N<sub>2</sub>/NH<sub>3</sub> plasma):**  
Residue accumulation due to **feed gases**

**Figure 2-2.** Comparison of the mechanism for gradual film deposition on reactor wall. a) Si etch plasma. b) SiN<sub>x</sub>H<sub>y</sub> deposition plasma.

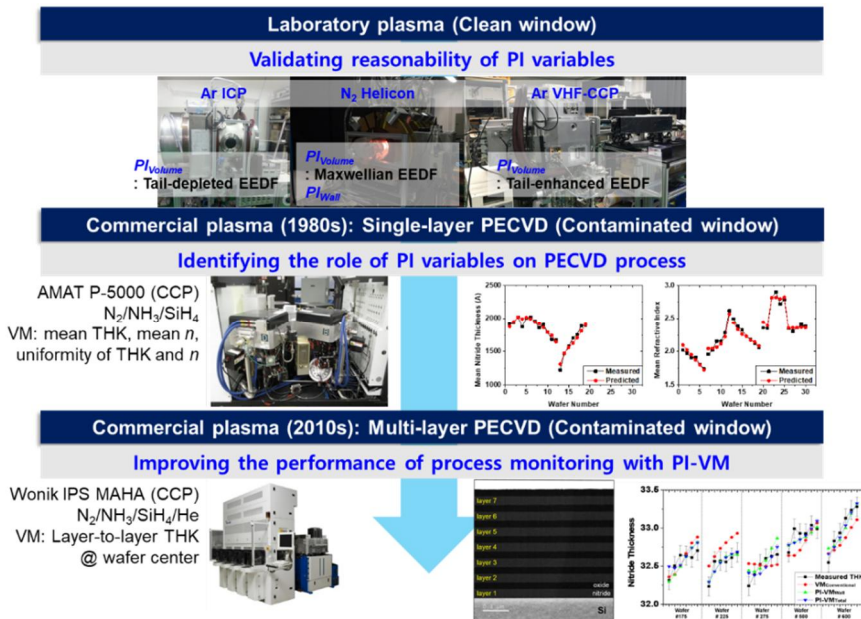


**Figure 2-3.** Experimental verification procedure to develop PI-VM. Here, THK means film thickness, and  $n$  means refractive index.

# **Chapter 3 . Development of PI-VM to Predict the Property of Deposited Film in Plasma-enhanced Chemical Vapor Deposition (PECVD)**

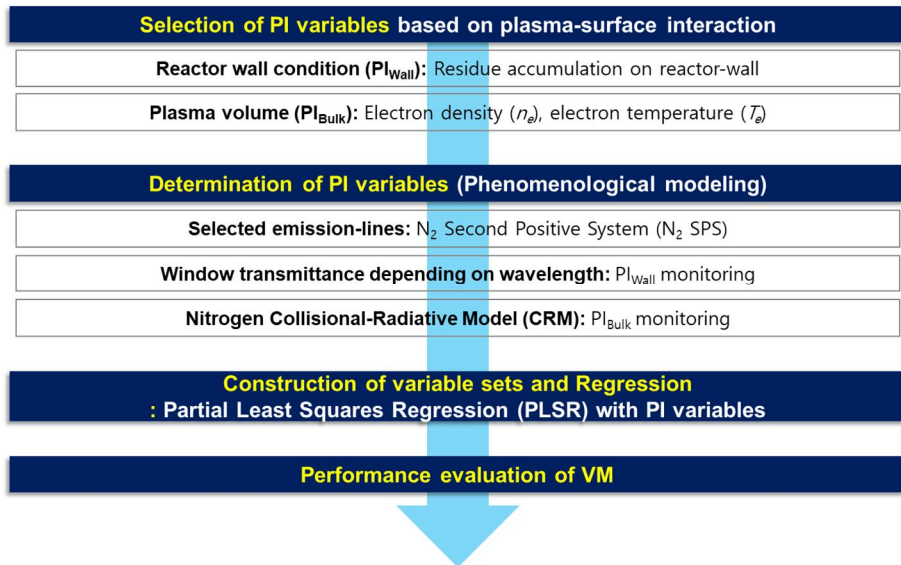
## **3.1 Procedure of PI-VM development**

Figure 3-1 shows the procedure of PI-VM development to predict the properties of deposited film. First, PI variables are selected under the consideration of the plasma-surface interaction on wafer. As mentioned Chapter 2,  $PI_{Volume}$  and  $PI_{Wall}$  are selected because they change the flux of reactive species through variation of EEDF and the desorption of residues or deactivation of reactive species at reactor-wall.

PI variables are determined by analyzing the phenomenology of sensor signals (Phenomenological modeling). OES and PIMs can be used to determine PI variables, because they can monitor the state of plasma non-invasively. In this dissertation, OES are used to determine PI variables. To analyze OES, a careful consideration should be performed based on the excitation kinetics in plasma [22]. Specifically, the line-intensities from OES are analyzed as a function of the excitation-rate coefficients; that is, the convolution-integral values of the radical density, the electron density, and the electron temperature. In addition to the dependency of these plasma properties, the wavelength-dependent optical transmittance is also considered in the analysis of line-intensities. Finally, a check regarding signal-to-noise ratio (SNR) of emission lines is conducted because it causes a great distortion in analysis. The details will be discussed in Chapter 4.

Input variable set for PI-VM is constructed by adding PI variables on the selected variable

set for statistical-based VM. The selected variable set for statistical-based VM is determined by using the conventional exhaustive search, because the number of process state variables of this dissertation is not large ( $\leq 20$  variables). Note that statistical variables selection methods, such as PCA and stepwise-selection methods, can be used to reduce the number of variables if it is too large to use exhaustive search. Also, a relatively simple linear model was used for regression, since the major purpose of this dissertation is the proposal of a novel methodology to obtain PI variables. Among linear models, PLSR was chosen as the regression model, since it is more robust for noise and correlation between variables than PCR [23].  $k$ -fold cross-validation was selected as validation method since only small number of records were available in this dissertation [14].  $k$ -fold cross-validation creates a  $k$ -fold partition of data. Then modeling and validation are performed  $k$  times. For each modeling and validation, only  $(k - 1)$ -folds are used as training sets and one different fold is used for validation set.



**Figure 3-1.** Flow chart of PI-VM development. Selections of PI variables, their parametrization method, and a regression model are required to develop PI-VM.

The performances of VM models are evaluated using  $R^2$ ,  $Q^2$  values [24] and mean absolute percentage error (MAPE) for validation records.  $R^2$  is the well-known coefficient of determination, indicating the goodness of fit of training records, as follows:

$$R^2 = 1 - \frac{\sum_{i=\text{Training}} (y_i - \hat{y}_i)^2}{\sum_{i=\text{Training}} (y_i - \bar{y})^2}, \quad (3.1)$$

where  $y_i$  is the metrology variable;  $\hat{y}_i$  is the predicted one from VM model; and  $\bar{y}$  is the mean measured metrology variable.  $Q^2$  indicates the  $R^2$  for the validation records, as follows:

$$Q^2 = 1 - \frac{\sum_{i=\text{Validation}} (y_i - \hat{y}_i)^2}{\sum_{i=\text{Validation}} (y_i - \bar{y})^2}. \quad (3.2)$$

The general requirements for a sound VM model are as follows [24]; the values of both  $R^2$  and  $Q^2$  should be high (at least 0.5 [25]) and the difference between  $R^2$  and  $Q^2$  should not be too large. If the difference is too large, VM model is over-fitted. MAPE for validation records is defined as follows:

$$\text{MAPE} = \frac{\sum_{i=\text{Validation}} |(y_i - \hat{y}_i) / y_i|}{N_{\text{Validation}}} \times 100(\%), \quad (3.3)$$

where  $N_{\text{Validation}}$  is size of validation records. MAPE closer to zero means the better performance of VM model. Also, the effect of each variable on the best VM model was then evaluated using an analysis of variable influence on projection (VIP) of each variable  $k$  [24]:

$$[\text{VIP}(k)]^2 = j \times \sum_a W_{ak}^2 \text{SSY}\%(a) / \text{SSY}\%(\text{cum}), \quad (3.4)$$

where  $j$  is the number of variables;  $a$  is the number of PLS components;  $W$  is the PLS weight;  $\text{SSY}\%(a)$  is the explained sum of squares (SS) of the  $a^{\text{th}}$  PLS component; and  $\text{SSY}\%(\text{cum})$  is the total SS of the  $Y$  that is explained by the model. VIP is the cumulative measure of the influence of each variable  $k$  on the model. In general, a VIP larger than 0.8 indicates that the variable is important.

## 3.2 Experimental setups

Table 3-1 describes experimental setups used in this thesis. As mentioned in Chapter 2, the monitoring reasonability of PI variables is validated by using the laboratory plasma (Helicon in Table 3-1). Then, the meaning of PI variables on the formation of nitride film in single-layer PECVD is interpreted by constructing PI-VM for thickness and refractive index (Applied Materials, P-5000). Finally, the concept of PI-VM is applied to predict layer-to-layer nitride film thickness in nitride/oxide multi-layer PECVD used for 3D NAND fabrication in the mass production line (Wonik IPS, MAHA).

Figure 3-2(a) shows a schematic diagram of the helicon plasma. A twisted Nagoya type coil was connected to a 13.56 MHz power supply via an L-type matching network. A 146 mm in diameter in length grounded cylindrical SUS chamber was placed next to the quartz. Note that only H-mode plasma was used to evaluate the reasonability of PI monitoring without utilizing magnetic field.

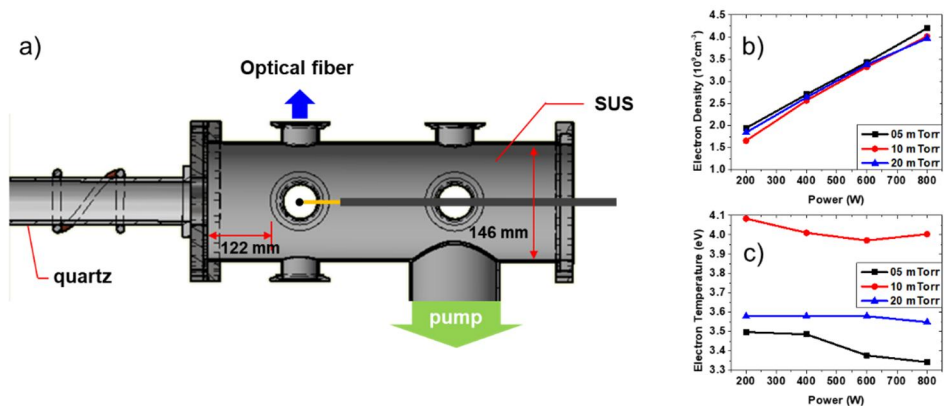


**Figure 3-2.** Experimental condition of helicon plasma. a) Schematic diagram of the helicon plasma. Magnetic coil was excluded in figure to improve visibility. b) Measured electron density. c) Measured electron temperature.

**Table 3-1.** Experimental setups. LP means Langmuir probe, THK means film thickness,  $n$  means refractive index, and L2L means layer-to-layer.

<b>Condition</b>	<b>Helicon (in H-mode)</b>	<b>Single-layer PECVD (CCP)</b>	<b>Multi-layer PECVD (CCP)</b>
RF frequency	13.56	13.56	27.12+0.37
Power (W)	200-800	300-720	850
Pressure (mTorr)	5-20	4000-5500	3500
Gas composition	N <sub>2</sub>	N <sub>2</sub> /NH <sub>3</sub> /SiH <sub>4</sub> =5-30/1/2.85	N <sub>2</sub> /NH <sub>3</sub> /SiH <sub>4</sub> /He =200/10/1/83.33
Heater temperature (°C)	-	400	560
Sensors	LP, OES (AvaSpec-2048&AvaSpec-3648)	OES (KSP-SM245)	PIM (Zcos $\theta$ , Zsin $\theta$ , $\theta$ ), OES (KSP-SM245)
Equipment variables	-	Power, pressure, flow rate, heater temperature	forward/reflected power (27.12 MHz), load/tune position (27.12 MHz), pressure, throttle- valve (VAT) position
Wafer state variables	-	Mean THK and $n$ , uniformity of THK and $n$	L2L THK at wafer center
Number of wafers	-	Processed: 30 Measured: 30	Processed: ~650 Measured: 5
Notes	Laboratory plasma	Applied Materials, P-	Wonik IPS, MAHA

The planar-type Langmuir probe was located 122 mm from boundary between quartz and SUS and radially center position. The volume-integrated emission spectra in the 200–950 nm wavelength (AvaSpec-2048 & AvaSpec-3648, Avantes, The Netherlands) were observed through the quartz window aligned at 122 mm from boundary between quartz and SUS. 2-channel spectrometer was used to improve wavelength resolution. The wavelength resolution of the spectrometer is 0.18-0.22 nm for 200–450 nm and 0.3-0.36 for 450-950nm at full-width at half-maximum (FWHM). The emission spectrum was measured by setting the integration time as 75 msec with 20 times average for 200–450 nm region and 150 msec with 10 times average for 450-950nm region. Also, tungsten-halogen light source (AvaLight-DH-CAL, Avantes, The Netherlands) was used for a relative-intensity calibration of spectroscopic system. Figure 3-2(b) and (c) shows measured electron density and temperature by using Langmuir probe in this experimental condition. The electron density increases from  $1.5 \times 10^9 \text{ cm}^{-3}$  to  $4.0 \times 10^9 \text{ cm}^{-3}$  according to power and the electron temperature decreases as pressure increases.

Figure 3-3 shows a schematic diagram of the narrow-gap capacitively coupled plasma (CCP) for the nitride single-layer PECVD. The showerhead electrode was connected to 13.15 MHz power via a matching network. The bottom electrode was connected to a heater to keep the wafer at a constant temperature. The gap distance of interelectrode was fixed at less than 10 mm. Base pressure was  $4.0 \times 10^{-3}$  Torr and 200mm wafer was processed

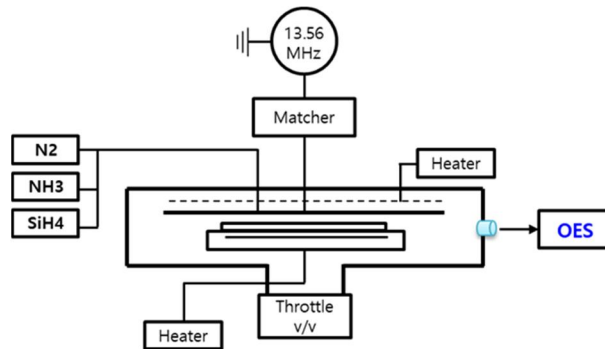


**Figure 3-3.** Schematic of narrow-gap capacitively coupled plasma (CCP) for single-layer PECVD.

In single-layer PECVD process, the volume-integrated emission spectra of the nitride PECVD in the 300–850 nm wavelength (SM245, Korea Spectral Products, Republic of Korea) were observed through the quartz window aligned at the bottom electrode. The emission spectrum was measured by setting the integration time of spectrometer as 10 msec with 10 times average. Also, the spectrum was recorded every 200 msec. The wavelength resolution of the spectrometer is approximately 1 nm at full-width at half-maximum (FWHM). Tungsten-halogen light source (AvaLight-DH-CAL, Avantes, The Netherlands) was used for a relative-intensity calibration of spectroscopic system. Table 3-2 shows process recipe of single-layer PECVD. There were some steps to stabilize the wafer process, such as wafer-in, stable, pre-deposition, haze elimination, and cleaning steps. In this thesis, the recipe of deposition step was changed to construct VM.

**Table 3-2.** Process recipe of single-layer PECVD. Heater temperature was maintained at 400°C. Dry CLN means dry cleaning step.

Step	Process time (sec)	Pressure (Torr)	Power (W)	Gas (sccm)
Wafer-in	10	Base	0	N <sub>2</sub> =3000

Stable	10	4.3	0	$N_2/SiH_4=3000/40$
Pre-deposition	2	4.3	50	$N_2/SiH_4=3000/40$
Deposition	5-60	4-5.5	300-720	$N_2/NH_3/SiH_4$ =500-3000/100/285
Haze elimination	2	4.3	720	$N_2/NH_3=4000/100$
Pump	10	Base	0	-
Dry CLN	30	5.5	1000	$CF_4/N_2O=1550/455$

After wafer process, ellipsometry was used to measure thickness (THK) and refractive index ( $n$ ) at 633.0 nm. Figure 3-4 shows the measured position of ellipsometry. In this thesis, averaged value of THK and  $n$ , center-to-edge ratio of THK and  $n$  were used as wafer state variables.

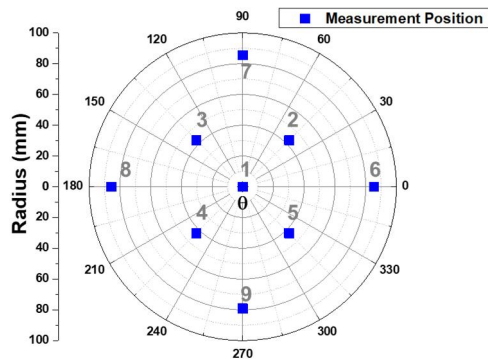


**Figure 3-4.** Measurement position of single-layer PECVD by using ellipsometry.

Figure 3-5 shows a schematic diagram of the narrow-gap capacitively coupled plasma (CCP) for the nitride/oxide multi-layer PECVD. The showerhead electrode was connected to 27.12 MHz and 370 kHz powers via a matching network. The bottom electrode was connected to a heater to keep the wafer at a constant temperature. The gap distance of

interelectrode was fixed at less than 10 mm.

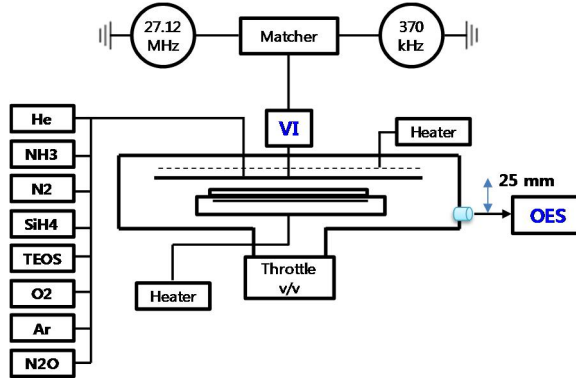


**Figure 3-5.** Schematic of narrow-gap capacitively coupled plasma (CCP) for multi-layer PECVD.

In multi-layer PECVD process, only nitride PECVD was monitored because oxide PECVD was difficult to measure emissions due to small emission intensity. The volume-integrated emission spectra of the nitride PECVD in the 300–850 nm wavelength (SM245, Korea Spectral Products, Republic of Korea) were observed through the quartz window aligned at 25 mm below the bottom electrode. The wavelength resolution of the spectrometer is approximately 1 nm at full-width at half-maximum (FWHM). Tungsten-halogen light source (AvaLight-DH-CAL, Avantes, The Netherlands) was used for a relative-intensity calibration of spectroscopic system. PIM sensor monitored current, voltage, and phase( $\theta$ ). In addition, forward/reflected powers of 27.12 MHz, load/tune-capacitor position of the matcher, operating pressure, and throttle-valve (VAT) position were monitored. Approximately 600 wafers were processed, and 7 stacks were deposited per a wafer. Here, one stack is composed of one pair of nitride/oxide film layer and the nitride film was deposited prior to the oxide-film deposition. Figure 3-6 shows process sequence of multi-layer PECVD. Dry-cleaning (CLN) and pre-coating processes of reactor-wall were conducted before the first nitride film deposition. Then nitride and oxide PECVD were conducted alternatively. The recipe of nitride

deposition step is expressed in Table 3-1.

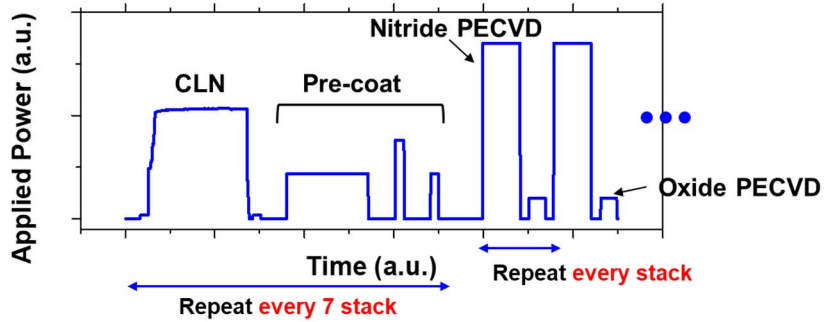


Figure 3-6. Process sequence of multi-layer PECVD.

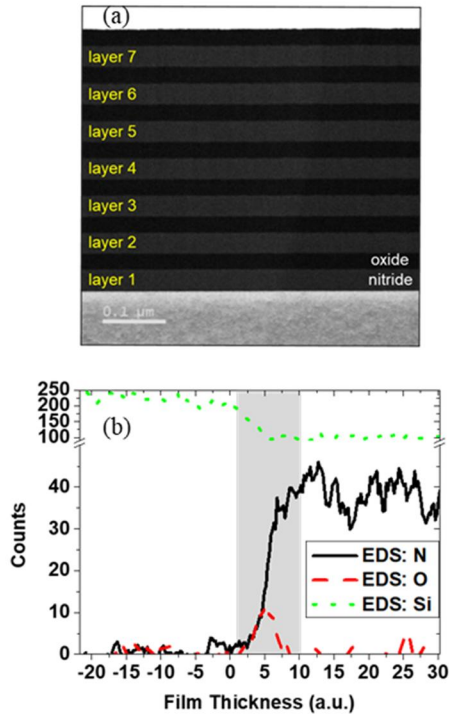
For the development of PI-VM, L2L thickness of five wafers at every 100<sup>th</sup> wafer was measured from a scanning transmission electron microscope (STEM) image, having a 0.25-nm pixel resolution, as shown in Figure 3-7(a). Note that in multi-layer PECVD process, only five wafers were allowed for analysis by the manufacturer (#175, #225, #275, #500, #600). Also, the first nitride layer was excluded from thickness measurement due to uncertainty of STEM signal caused by silicon (Si) signal from the wafer. Finally, the total number of records (thicknesses of nitride layer) was limited to 30 records (equal to 5 wafers multiplied by 6 layers).

Figure 3-7(b) shows depth profiles of the nitrogen (N), oxygen (O), and silicon (Si) in the first nitride layer measured by energy dispersive X-ray spectroscopy (EDS). It is noteworthy that the oxygen signal was observed in the first nitride layer. It is expected that oxygen was deposited on wafer after desorbed from oxynitride film which was deposited on reactor-wall during the pre-coating process. That is, the O signal in the first nitride layer shows the effect of reactor-wall condition on process result. The fraction of the O at the first layer ( $F_O$ ) is obtained by averaging the intensity of the EDS signal in shaded region, as follows:

$$F_O = \frac{\langle O \rangle}{(\langle N \rangle + \langle O \rangle + \langle Si \rangle)} \times 100 \% , \quad (3.5)$$

where the angle brackets represent the averaged value at the shaded area of Figure 3-7(b).

The  $F_O$  will be discussed in Chapter 4 to validate that  $PI_{Wall}$  can monitor the drift of the reactor-wall condition.



**Figure 3-7.** Measurement of wafer state variables (wafer #175). (a) STEM image for the thickness representing the sets of the nitride and oxide layers. (b) EDS analysis for oxygen fraction at the first nitride layer on wafer. The shaded area shows the existence of oxynitride film at the first nitride layer on wafer.

The coupon tests were conducted to interpret the amount of film deposition on reactor-wall depending on equipment time and the major process at reactor that drifts the wafer state. Table 3-3 shows process recipe for coupon test. After dry cleaning process, silicon nitride and oxide films are deposited on reactor wall through pre-coat 1 and 2 steps. Then, multi-layer

PECVD processes are conducted. The aluminum plate ( $\text{Al}_2\text{O}_3$ , 7 mm x 7 mm) was used as coupon because it is the matter of reactor-wall.

**Table 3-3.** Process recipe of multi-layer PECVD for coupon test. All step has 10-20 mm gap size between electrode and 2-4 Torr operating pressure. The frequency of remote source was 400 kHz and that of CCP was 13.56 MHz. For oxide PECVD, 370 kHz power was additionally applied to top electrode.

Step	Source	Power (W)	Gas composition
Dry CLN	Remote	200-500	$\text{NF}_3/\text{Ar}/\text{He}$
Pre-coat 1	CCP	-	$\text{SiH}_4/\text{He}/\text{N}_2$
Pre-coat 2	CCP	-	$\text{TEOS}/\text{He}/\text{O}_2$
Nitride PECVD	CCP	300-400	$\text{SiH}_4/\text{N}_2/\text{NH}_3/\text{He}$
Oxide PECVD	CCP	500-800 (<50 for 370 kHz)	$\text{TEOS}/\text{Ar}/\text{O}_2$

STEM and EDS were used to detect thickness and composition of film deposited on three coupons. The treatment condition of each coupon is described in Table 3-4. First coupon is ‘pristine’ which has thin native oxide layer. Second coupon represents the state of reactor-wall after dry cleaning and pre-coating processes. Third coupon represents the state of reactor-wall after 14 pairs silicon nitride/oxide PECVD processes.

**Table 3-4.** Coupon test condition.

Coupon name	Treatment condition
Pristine	Bare $\text{Al}_2\text{O}_3$ coupon with native oxide
Pre-coat	Coupon establishment (vacuum break) → Dry CLN & precoat → coupon removal (Vacuum break)

---

14 pairs

Coupon establishment (vacuum break) → Dry CLN & precoat

→ 14 pairs multi-layer PECVD → coupon removal (Vacuum break)

---

## Chapter 4 . Determination of PI Variables by Using Plasma Spectroscopy

### 4.1 Plasma spectroscopy

Plasma *emission* spectroscopy or optical emission spectroscopy (OES) is the study of electromagnetic radiation emitted from ionized plasma, called emission spectra [26]. It is one of the most established and oldest diagnostic tools in astrophysics, plasma physics [27]. It is also being adopted to monitor the state of plasma-assisted process for semiconductor manufacturing. Generally, spectrometer measures line-of-sight or volume averaged emission spectra although some techniques have been proposed to measure spatially resolved emissions in radial direction [28, 29]. Emission spectra in visible spectral range can be measured easily by the connected optical fiber and spectrometer at quartz window, because the visible light can penetrate in air and quartz window [30]. Nowadays, OES sensor is one of major monitoring sensor of plasma-assisted process for semiconductor manufacturing since it is itself non-invasive meaning that there is no perturbation of the plasma by the diagnostic tool. Plasma spectroscopy can measure particle densities (excited states, radicals, molecules, electrons, ions), temperatures (atoms, molecules, ions, electrons), and electric/magnetic fields by analyzing the emissions from atoms, molecules, and ions [31].

Among emissions, line-emission or bound-bound emission is the transition from specific upper energy level  $p$  state to lower energy level  $k$  state. The line-intensity is quantified as the number of photons per unit volume per unit time ( $\text{m}^{-3}\text{s}^{-1}$ ):

$$I_{pk} = S(\lambda)T(\lambda)n_p A_{pk} \theta_{pk}, \quad (4.1)$$

where,  $S(\lambda)$  is wavelength-dependent sensitivity of spectroscopic system,  $T(\lambda)$  is wavelength-dependent transmittance on window,  $n_p$  is the number density of  $p$  state ( $\text{m}^{-3}$ ),  $A_{pk}$  is the radiative decay coefficient or Einstein coefficient ( $\text{s}^{-1}$ ), and  $\theta_{pk}$  is the photon escape factor which is a function of the number density of the lower state  $k$ . Here, the optical escape factor indicates the degree of radiation trapping ( $0 \leq \theta_{pk} \leq 1$ ). If the optical escape factor is 1, the radiation trapping is not present in the plasma. While in the case of  $\theta_{pk} = 0$ , the light cannot be emitted out of the plasma.

$S(\lambda)$  in equation (4.1) is a function of the total system efficiency of spectrometer which is the combination of optical fiber transmission, grating and mirror efficiency, detector quantum efficiency and coating sensitivities. Total system efficiency of spectrometer can be calibrated by using standard calibrated light sources, visible spectral range for tungsten-halogen lamp. and UV range for deuterium lamp. Calibration method is divided into absolute and relative calibration. In absolute calibration, measured intensity (voltage or counts/s) is converted into  $\text{W}/(\text{m}^2\text{sr})$  or  $\text{photons}/(\text{m}^2\text{s})$ . It can be used when the solid angle and volume of plasma measured by spectrometer are well defined, such as atmospheric pressure plasma jet (APPJ). The low-pressure plasma is hard to use absolute calibration because the plasma is spread widely in the reactor which makes difficult to define solid angle and plasma volume. Instead, line-ratio method which compared the intensity ratio of two emission lines are used after relative calibration of total system efficiency of spectrometer. On the other hand, quartz window established at plasma-assisted process can be contaminated due to film deposition on window. This window contamination effect can change the transmittance on window ( $T(\lambda)$ ) depending on the thickness, refractive index, and extinction coefficient of thin film. It makes difficult to apply plasma spectroscopy to the plasma-assisted process for semiconductor manufacturing, because the vacuum cannot be broken during the process to calibrate window.

The population density of excited level  $n_p$  in equation (4.1) is determined by population kinetics in plasma which considers generation and destruction reaction of  $p$  state in plasma. The dominant population and de-population reaction for  $p$  state are a function of the thermodynamic equilibrium (TE) of corresponding energy state. Appendix A briefly discuss the classification criteria of excitation equilibria. The proper assumption of TE of each energy state is required to determine PI variables based on the line-intensity ratio method. First, low-temperature and low-pressure plasma in continuous wave (CW) mode generally belongs to ionizing plasma. In ionizing plasma, the electron-impact ionization is larger than recombination of ion-electron pair, because the generated plasma is dominantly destructed through three-body recombination at reactor wall. In the ionizing plasmas, TE or balance of energy state can be classified as corona balance (CB), excitation saturation balance (ESB), partial local thermodynamic equilibrium (PLTE), and local thermodynamic equilibrium (LTE) regime depending on electron density and temperature [32]. The boundary between ESB and PLTE regime is determined whether the atomic state distribution function (ASDF) of excited state is following Saha-Boltzmann distribution or not. On the other hand, the boundary between CE and ESB regime is determined when the collisional destruction equals to radiative destruction. Assuming  $T_e^* = T_d / Z^2 = 1 \text{ eV}$  and charge number  $Z=1$ , the approximated condition is given as [32]:

$$N_e^* p_{cr}^9 = 9 \times 10^{23} \text{ m}^{-3}, \quad (4.2)$$

where  $N_e^*$  is  $n_e / Z^7$ ,  $p_{cr}$  is the effective quantum number of boundary. Here, the effective quantum number  $p^*$  is determined as:

$$p^* = Z \sqrt{R / (E_{ion}^g - E_{ion}^p)}, \quad (4.3)$$

where  $R$  is Rydberg energy (13.6 eV),  $E_{ion}^g$  is ionization threshold energy from ground state, and  $E_{ion}^p$  is ionization threshold energy from  $p$  state. If  $p^*$  is smaller than  $p_{cr}$ , the energy state belongs to the CE regime. In [32], the RHS of equation (4.2) can be varied within a factor

5 for  $0.1 \leq T_e^* \leq 100$ . Note that electron-impact excitation is one of most important reaction in low-temperature and low-pressure plasma where most process for semiconductor manufacturing occurs. The rate constant ( $\text{m}^3\text{s}^{-1}$ ) for electron-impact excitation ( $Q_{exc}$ ) is described as the convolution integral of energy-dependent excitation cross-section with EEDF [33]:

$$Q_{exc} = \sqrt{\frac{2}{m_e}} \int_{E_{th}}^{\infty} \sigma_{exc}(E) f(E) \sqrt{E} dE, \quad (4.4)$$

where  $m_e$  is electron mass (kg),  $E_{th}$  is threshold energy (eV),  $\sigma_{exc}$  is excitation cross section, and  $f(E)$  is EEDF.

In summary, volume-integrated line-emission of plasma-assisted process is described as a non-linear function of transmittance and the integral which includes information about the density of excited states and EEDF in plasma. The population of excited states are related to each other. Therefore, the determination of plasma information variable is a numerical optimization problem to minimize the error between measured and expected line-intensities. To efficiently converge the optimization problem, the following two points should be considered. Firstly, it is important to select emission lines which is sensitive to specify the plasma information variable and can effectively distinguish the terms constructed as an independent function of each plasma information variables. To do this, the classification of excitation equilibria of each energy state should be preceded. Secondly, the reaction information, such as excitation cross-section and form of EEDF, should be selected to account for the excitation equilibria of selected energy state reasonably. In this chapter, the method to determine  $PI_{\text{Volume}}$  and  $PI_{\text{Wall}}$  will be discussed based on the criteria for selecting appropriate emission line and reaction data.

## 4.2 Relative calibration of the spectroscopic system

Relative calibration evaluates the spectral sensitivity of the spectroscopic system along the wavelength axis. It provides a relative sensitivity for each wavelength of spectroscopic system, allowing the application of line-intensity ratio method, although it does not provide an absolute value of emissivity ( $\text{Wm}^{-2}\text{sr}^{-1}$ ) or emission intensity ( $\text{photons}(\text{m}^3\text{s}^{-1})$ ). Figure 4-1 shows calibrated spectral irradiance of deuterium-halogen light source (AvaLight-DH-CAL, Avantes, The Netherlands) which has CC-VIS/NIR diffuser as entrance of the light source. UV calibration was performed from national physical laboratory (NPL) and VIS/NIR calibration was performed from national institute of standards and technology (NIST).

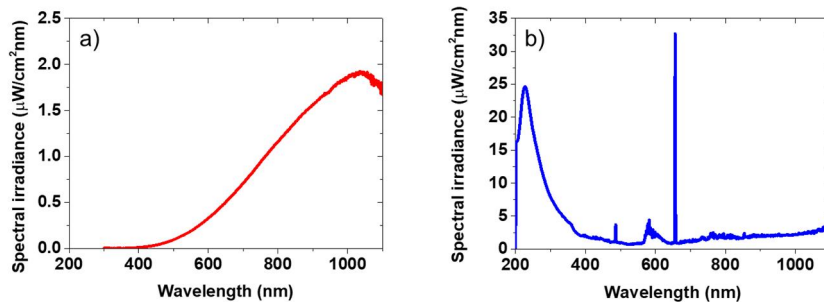


**Figure 4-1.** Calibrated spectral irradiance of deuterium-halogen light source. a) Halogen light source (Wolfram Halogen 6390-DZA). b) Deuterium-halogen light source (Deuterium DOS 650 TJ).

Figure 4-2 shows example of measured spectrum for the deuterium-halogen light source. It shows that the spectral sensitivity of the spectroscopic system is not constant especially in low-wavelength and high-wavelength region.

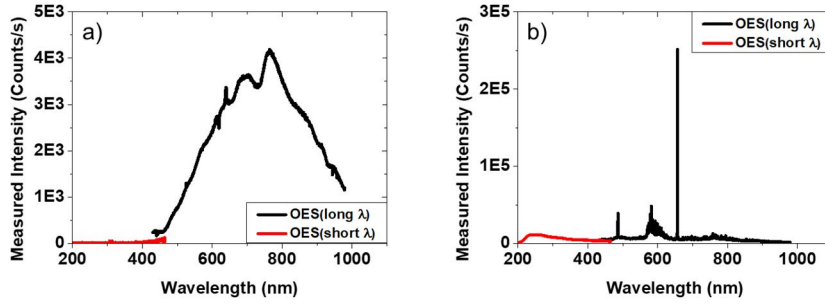


**Figure 4-2.** Measured emission intensity of deuterium-halogen lamp. a) Halogen light source. b) Deuterium-halogen light source. 2-channel spectrometers (AvaSpec-2048 & AvaSpec-3648) was used.

The conversion factor,  $C(\lambda)=1/S(\lambda)$ , is obtained by dividing spectral irradiance by measured spectrum intensity with considering their unit:

$$C(\lambda) = \frac{IR_{cal}(\lambda)}{I_{measured}(\lambda)} \frac{4\pi\lambda}{hc}, \quad (4.5)$$

where  $IR_{cal}$  is calibrated spectral irradiance ( $\mu\text{Wcm}^{-2}\text{nm}^{-1}$ ),  $I_{measured}$  is measured intensity of deuterium-halogen lamp (Counts  $\text{s}^{-1}$ ),  $h$  is Planck constant ( $\text{m}^2\text{kg s}^{-1}$ ), and  $c$  is speed of light ( $\text{m s}^{-1}$ ). Then, one can determine relatively calibrated emission spectrum by multiplying conversion factor as follows:

$$I_{calibrated}(\lambda) = C(\lambda)I_{measured}(\lambda) = \frac{I_{measured}(\lambda)}{S(\lambda)}. \quad (4.6)$$

Figure 4-3 shows the example of conversion factor for 2-channel spectrometers. Note that conversion factor is large in the short and long wavelength region meaning that spectral sensitivity of spectrometer in those wavelength regions is low. It means that the spectral response (or quantum efficiency) of CCD is low in those wavelength regions. For short wavelength, many photons are absorbed at the gate structures before they can be detected in the depleted region. On the other hand, photons with longer wavelengths have a low

probability of absorption by the silicon and can pass through the depletion region without being detected due to their low energy.

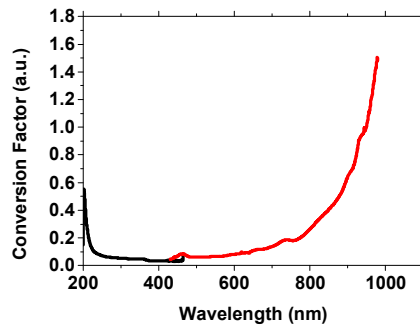


**Figure 4-3.** Conversion factor for 2-channel spectrometers (AvaSpec-2048 & AvaSpec-3648).

### **4.3 Selection criteria of emission lines and reaction data**

The line-intensity ratio method for plasma-assisted processes is developed by selecting two or more emission lines which have different trend of variation depending on the variation of target PI variable. Selecting emission lines that can sensitively determine PI variables is the most important option in plasma spectroscopy. There is no model that can account for all phenomena in plasma, and it is practically impossible to obtain qualified cross-sections for all reactions. For example, emission model is difficult to use plasma uniformity as a variable, and to obtain a precise reaction cross-section for high-lying states. That is, if the emission lines that are insensitive to PI variables are selected, the second order phenomena that is not considered in the established emission model can weaken the reliability of PI monitoring method. Also, the line-emissions from resonance state, the energy level capable of emitting light to ground state, is not selected to monitor PI variables. Note that the radiation trapping effect of resonance states offers a sensitive pressure dependence of resonance states deepening the complexity of emission model.

The hardware specification of spectrometer acts as additional criterion for the selection of emission line to monitor PI variables. The hardware specification of spectrometer affects the selection of line emissions by determining signal-to-noise ratio (SNR) and wavelength resolution of spectrometer. The wavelength resolution is described as full width half maximum (FWHM), which is defined as the width of the peak at 50% of the maximum intensity. Typical spectrometers used in plasma-assisted processes have symmetrical Czerny-Turner design with CCD (charge-coupled device) array. The range of FWHM is 0.2 ~ 20 nm

(generally less than 2 nm) and the range of SNR is 250:1~1000:1 depending on grating, slit size, number of pixels, CCD type. The selected emission lines should be able to distinguish with other emission lines. In case of using overlapped emissions, it requires the reliable emission model which can include the modeling about all overlapped emissions. Also, the selected lines should have a sufficient SNR to permit monitoring of the variation of target plasma-assisted process.

Proper reaction constants or cross-sections should be considered to develop emission model. In low-pressure and low-temperature plasma, step-excitation, which is the excitation from the lowest metastable or resonance states, should be considered in emission model. Also, for the transition to these states, the radiation trapping effect should be considered, because their large density induces significant reabsorption of photon. On the other hand, for excitation reaction from ground state, not only direct excitation but also the cascade effect, transition from high-lying states, should be considered in emission model or reaction-cross sections.

Therefore, the information about reaction should be selected with the following criteria:

(1) For excitation from ground state, the cascade effect should be considered. It is sensitively affected by the population of high-energy tail of EEDF due to its high threshold energy. That is, the reaction rate should be determined through the convolution integral of cross-section and EEDF. If there is no cross-section where the cascade effect is considered, PI variables can be determined by using the full CRM including particle balance for the high-lying states and direct excitation cross-section. But it greatly increases the complexity of emission model.

(2) For step excitation, only reactions of dipole-allowed type with each metastable and

resonance state are considered, because density of lowest metastable and resonance states is much smaller than that of ground state ( $10^{-6}\sim 10^{-4}$  in low-temperature plasma). An approximated formula of rate constant ( $\text{m}^3\text{s}^{-1}$ ) expressed as a function of electron temperature can be used if the cross-section data cannot exist because the threshold energy is much lower than excitation from ground state. If there is no approximated formula of rate constant, the emission lines which are spin-forbidden to the lowest metastable and resonance states can be selected to minimize the influence of step excitation.

## 4.4 Development of monitoring variable for reactor-wall condition

The reactor-wall condition often alters wafer state variables by changing the influx of reactive species through desorption, deactivation, or sputtering. For example, SiOCl contaminated wall increases etch rate, especially at wafer edge, because it increases Cl density at wafer edge through the reduction of recombination of Cl radicals [34]. The desorption of F radicals from AlF<sub>x</sub> reactor-wall increases undercut of etch profile by inhibiting the formation of passivation layer [35]. The plasma community has been studying the mechanism how the films build up on the reactor-wall and how the plasma is perturbed due to reactor wall condition by using surface analysis techniques, such as X-ray photoelectron spectroscopy (XPS) or Fourier-transform infrared spectroscopy (FTIR) [35-37]. The numerical simulations have been carried out to analyze the influence of plasma-wall interaction on wafer state variables depending on reactor-wall condition [38-40]. Recently, some sensor techniques have been developed to monitor reactor-wall condition during plasma-assisted processing, as mentioned earlier. These techniques monitor electrically or optically the variation of film deposited on the materials, such as floating planar-type probe and internal reflection crystal (IRC), inserted near the reactor-wall [18, 19]. However, these methods have some limitation to adopt in process monitoring technology because they require the invasive sensor components

In the aspect of plasma spectroscopy, deposition of film on window (or window clogging effect) act as a major hurdle to apply plasma spectroscopy to the monitoring technology for plasma-assisted process. Importantly, the window clogging effect changes the light transmittance on window which depend on the range of wavelength. Note that relative

calibration of spectroscopic system cannot consider the effect of film deposition on window to wavelength-dependent sensitivity, because the standard light source cannot be installed in the reactor. Therefore, a novel method is required to calibrate the emission spectrum by diagnosing non-invasively the variation of wavelength-dependent transmittance.

This work develops  $PI_{\text{Wall}}$  which can monitor the variation of wavelength-dependent transmittance on window non-invasively. In the development of  $PI_{\text{Wall}}$ , it is assumed that the deposition of residue on quartz window and reactor-wall are similar despite of their different sticking probability for reactive species. More assumption is that the optical transmittance through the deposited window is varied with the film-thickness on the quartz, representing the reactor wall condition. This work utilized that the light transmittance is attenuated as the deposition or clogging of window increases. In the nitride/oxide multi-layer PECVD, some oxynitride film could be deposited on window. Note that the attenuation of OES signal in oxynitride film is higher for low wavelengths because of large refractive index and extinction coefficient for this wavelength region [41]. When film deposition on window was increased, a greater attenuation of OES signal occurred for the lights at lower wavelength than those of the higher wavelength. Therefore, the line-intensity ratios of lower and higher wavelengths can be to monitor the film deposition on quartz-window, representing the reactor-wall condition.

The molecular emission of  $N_2$  gas, which is the main gas in the nitride PECVD, was considered in the development of PI variables. Especially,  $N_2$  second positive system (SPS) was chosen.  $N_2$  SPS is the band spectrum emitted during transition from  $N_2(C^3\Pi_u, \nu = 0-4)$  to  $N_2(B^3\Pi_g, \nu' = 0-21)$  states. Here,  $\nu$  and  $\nu'$  are the vibrational numbers of each state, respectively. There are two reasons to choose  $N_2$  SPS for the construction of PI variables, as follows: (1)  $N_2$  SPS offers relatively large emission intensities, and the overlap with the intensities from other electronic states is negligible. (2) The complexity of phenomenological model can be minimized because the radiation-trapping effect of  $N_2$  SPS is relatively small.

Here, radiation trapping means the self-absorption or reabsorption of the photon when it passes through plasma. Note that this phenomenon has a positive correlation with the density of lower state for radiative transition. Radiation-trapping effect can be significant when the transition occurs to metastable states which has relatively large density in plasma [22]. For N<sub>2</sub> SPS, the radiation-trapping effect can be neglected in this work because the lower states of N<sub>2</sub> SPS are the non-metastable states.

After correcting the relative calibration of spectroscopic system, the wavelength-dependent transmittance on window,  $T(\lambda)$ , is expressed as follows:

$$T(\lambda) \propto \frac{I_{pk}}{S(\lambda)n_p A_{pk} \theta_{pk}} . \quad (4.7)$$

The key idea is that if radiation-trapping effect is negligible, the line-intensity ratios from same upper state represents the wavelength-dependent transmittance, because  $n_p$  term in equation (4.7) can be neglected:

$$\frac{T(\lambda_{pk})}{T(\lambda_{pl})} \propto \left( \frac{I_{pk}}{S(\lambda_{pk})A_{pk}} \right) / \left( \frac{I_{pl}}{S(\lambda_{pl})A_{pl}} \right) . \quad (4.8)$$

The requirements of line selection for transmittance monitoring is as follows. Firstly, the line-emissions that can neglect the radiation trapping should be selected. Secondly, the selected line-emissions should be sufficiently distinguishable from other emissions to minimize the superposition effect with other line-emissions. Thirdly, the selected line-emissions should have enough SNR to indicate the drift of transmittance reasonably.

As mentioned earlier and will be discussed in chapter, N<sub>2</sub> SPS are used to determine transmittance, because they can neglect radiation-trapping effect. Also,  $p^*/p_{cr}$ , of N<sub>2</sub>(C<sup>3</sup>Π<sub>u</sub>,  $\nu = 0$ ) and N<sub>2</sub>(C<sup>3</sup>Π<sub>u</sub>,  $\nu = 1$ ) is about 0.23 meaning that the line-intensities from N<sub>2</sub>(C<sup>3</sup>Π<sub>u</sub>,  $\nu = 0$ ) and

$N_2(C^3\Pi_u, v = 1)$  are CB-like emissions. That is, radiative decay is dominant destruction mechanism. Figure 4-4 and Table 4-1 shows used  $N_2$  SPS line-intensities.

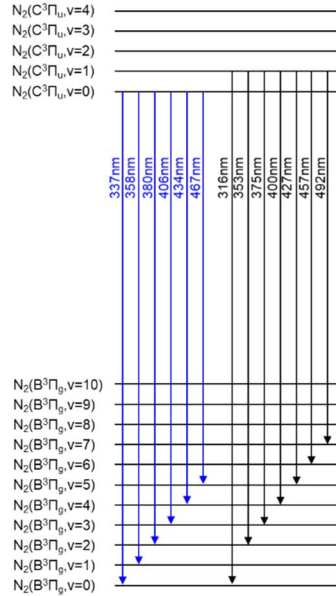


**Figure 4-4.** Line-intensities used to monitor the wavelength-dependent transmittance on window. Among  $N_2$  SPS, emissions from  $N_2(C^3\Pi_u, v = 0)$  and  $N_2(C^3\Pi_u, v = 1)$  are used, because they have relatively large intensity providing reasonable SNR.

Among  $N_2$  SPS, emissions from  $N_2(C^3\Pi_u, v = 0)$  and  $N_2(C^3\Pi_u, v = 1)$  are used, because they have relatively large intensity providing reasonable SNR.  $PI_{wall}$  is defined as the transmittance ratio between 426.8nm and 399.7nm or between 380.4nm and 357.6 nm as follows:

$$PI_{wall} = \frac{T(426.8nm)}{T(399.7nm)} \text{ or } \frac{T(380.4nm)}{T(357.6nm)}. \quad (4.9)$$



**Table 4-1.** Information about line-intensities used to monitor the wavelength-dependent transmittance on window.

$\lambda$  is wavelength, and  $A_{pk}$  is the radiative decay coefficient. All information is based on [42]

<b>Transition</b>	<b><math>\lambda</math> (nm)</b>	<b><math>A_{pk}</math> (<math>10^6 \text{ s}^{-1}</math>)</b>
$\text{N}_2(\text{C}^3\Pi_{u,v=0}) \rightarrow \text{N}_2(\text{B}^3\Pi_{g,v=0})$	337.0	13.1
$\text{N}_2(\text{C}^3\Pi_{u,v=0}) \rightarrow \text{N}_2(\text{B}^3\Pi_{g,v=1})$	357.6	8.84
$\text{N}_2(\text{C}^3\Pi_{u,v=0}) \rightarrow \text{N}_2(\text{B}^3\Pi_{g,v=2})$	380.4	3.56
$\text{N}_2(\text{C}^3\Pi_{u,v=0}) \rightarrow \text{N}_2(\text{B}^3\Pi_{g,v=3})$	405.8	1.10
$\text{N}_2(\text{C}^3\Pi_{u,v=0}) \rightarrow \text{N}_2(\text{B}^3\Pi_{g,v=4})$	434.3	0.292
$\text{N}_2(\text{C}^3\Pi_{u,v=0}) \rightarrow \text{N}_2(\text{B}^3\Pi_{g,v=5})$	466.5	0.0698
$\text{N}_2(\text{C}^3\Pi_{u,v=1}) \rightarrow \text{N}_2(\text{B}^3\Pi_{g,v=0})$	315.8	11.9
$\text{N}_2(\text{C}^3\Pi_{u,v=1}) \rightarrow \text{N}_2(\text{B}^3\Pi_{g,v=2})$	353.6	5.54
$\text{N}_2(\text{C}^3\Pi_{u,v=1}) \rightarrow \text{N}_2(\text{B}^3\Pi_{g,v=3})$	375.4	4.93
$\text{N}_2(\text{C}^3\Pi_{u,v=1}) \rightarrow \text{N}_2(\text{B}^3\Pi_{g,v=4})$	399.7	2.43
$\text{N}_2(\text{C}^3\Pi_{u,v=1}) \rightarrow \text{N}_2(\text{B}^3\Pi_{g,v=5})$	426.8	0.898
$\text{N}_2(\text{C}^3\Pi_{u,v=1}) \rightarrow \text{N}_2(\text{B}^3\Pi_{g,v=6})$	457.3	0.278
$\text{N}_2(\text{C}^3\Pi_{u,v=1}) \rightarrow \text{N}_2(\text{B}^3\Pi_{g,v=7})$	491.7	0.076888

$\text{PI}_{\text{Wall}}$  represents the ratio of wavelength-dependent transmittance which is a function of film thickness, refractive index, and extinction coefficient. If the property of film deposited on window is changed by recipe tuning, the value of  $\text{PI}_{\text{Wall}}$  can be changed. To analyze these factors separately, transmittance and reflectance analysis in the full wavelength region are required by using the additional light source. However, in the specific recipe, the fact that  $\text{PI}_{\text{Wall}}$  increases according to the buildup of the film on window remains unchanged. When window is clean,  $\text{PI}_{\text{Wall}}$  equals 1. As window is clogged,  $\text{PI}_{\text{Wall}}$  increases because the line intensity of

denominator is more attenuated than that of numerator.

Figure 4-5 shows the example of measured spectrum in three experimental setups. Helicon plasma which have clean window shows large intensities in low wavelength region, because the emissions in 300–400 nm region has large radiative decay coefficient (Table 4-1). Those intensities are weak in single- and multi-layer PECVD processes so that window contamination attenuates the emissions in 300–400 nm. The attenuation of multi-layer PECVD is more severe than that of single-layer PECVD. Note that Figure 4-5(c) is plotted as column bar because manufacturer provided only peak intensities.

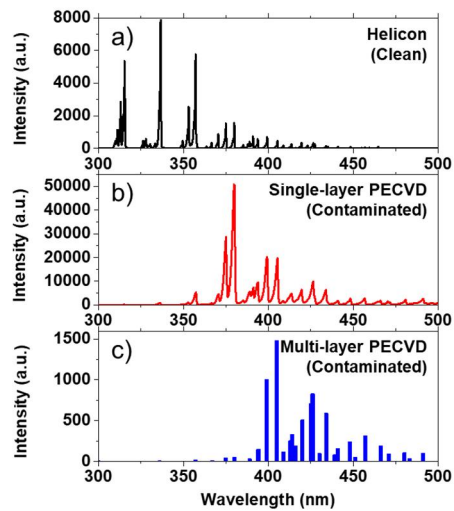


**Figure 4-5.** Comparison of measured N<sub>2</sub> emission spectrum. a) Helicon (N<sub>2</sub> 5 mTorr, 13.56 MHz 800 W). b) Single-layer PECVD (4 Torr, 13.56 MHz 720 W, N<sub>2</sub> 3000sccm). c) Multi-layer PECVD (Wafer #175, layer 1).

Figure 4-6 shows the measured transmittance spectrum at clean quartz window established near the wall of helicon plasma by using equations (4.8) and (4.9). The error bar indicates standard deviation of measured transmittance for all pressure and power variation condition in Table 3-1 and Figure 3-2. The inserted graph in Figure 4-6 shows the

transmittance of a typical quartz window (<https://www.janis.com>). The spectrum is plotted assuming the transmittance of quartz window at 405.8 nm as 95.3% considering typical transmittance of quartz window, because the absolute value of transmittance is not known value. Figure 4-6 shows that the transmittance monitoring model well illustrates the tendency to decrease of transmittance as the wavelength gets lower. That is, reasonable transmittance can be determined by using transmittance monitoring model based on OES.

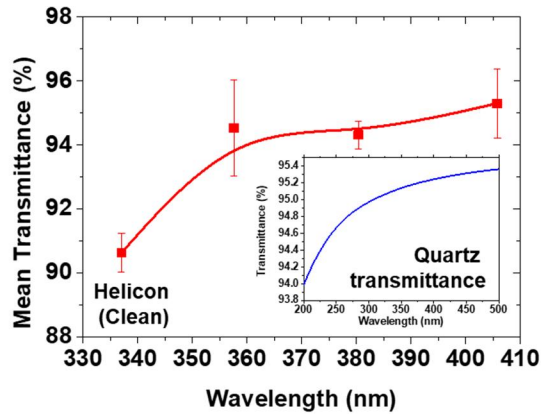


**Figure 4-6.** Validation of transmittance monitoring model at clean quartz window. (Helicon) The error bar is standard deviation of measured transmittance for all pressure and power variation condition in Table 3-1. The inserted graph shows the transmittance of a typical quartz window (<https://www.janis.com>).

The standard deviations depend on used wavelength and the relative large standard deviation at 405.8 nm was originated from its small intensity. To use 405.8 nm as emission-line for monitoring, SNR should be improved by increasing integration time of spectrometer or improving sensitivity of spectroscopic system.

The large standard deviation of 357.6nm emission is originated by superposition of N<sub>2</sub> SPS and N<sub>2</sub> first negative system (FNS). N<sub>2</sub> FNS is the band spectrum emitted during transition from N<sub>2</sub><sup>+</sup>(B<sup>2</sup>Σ<sub>u</sub><sup>+</sup>, ν = 0–10) to N<sub>2</sub><sup>+</sup>(X<sup>2</sup>Σ<sub>g</sub><sup>+</sup>, ν' = 0–21) states. Here, ν and ν' are the

vibrational numbers of each state, respectively. Figure 4-7 shows measured emission spectrum (a) and normalized intensity ratio between 357.6 nm and 337.0 nm (b). As shown in Figure 4-7(a), band head of transition from  $N_2(C^3\Pi_u, \nu = 0)$  to  $N_2(B^3\Pi_g, \nu' = 1)$  state (357.6nm) and band head of transition from  $N_2^+(B^2\Sigma_u^+, \nu = 1)$  to  $N_2^+(X^2\Sigma_g^+, \nu' = 0)$  state (358.0nm) are superposed within wavelength resolution. Although the magnitude of  $N_2$  FNS is small due to small ionization ratio in this plasma, emission intensities of  $N_2$  FNS obviously increase with increasing electron density due to the excitation from ground state  $N_2$  ion. Therefore, a spectrometer which cannot isolate  $N_2$  SPS and  $N_2$  FNS sufficiently is hard to use 357.6nm for developing the transmittance monitoring model, as shown in Figure 4-7(b). Note that the isolation issue of emission lines should also be satisfied for  $N_2$  first positive system (FPS), the band spectrum emitted during transition from  $N_2(B^3\Pi_g, \nu = 0-21)$  to  $N_2(A^3\Sigma_u^+, \nu' = 0-21)$  states.

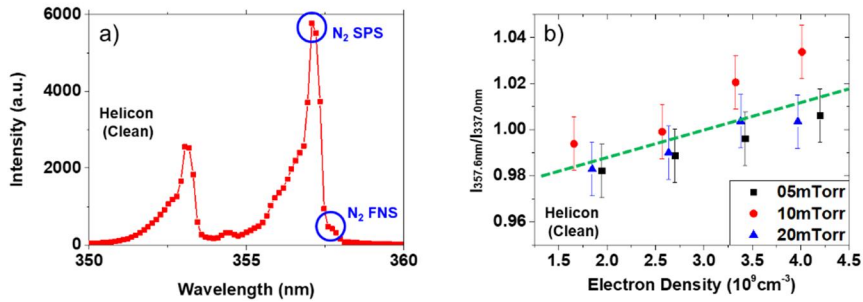


**Figure 4-7.** Superposition of  $N_2$  SPS and  $N_2$  FNS. a) Emission spectrum of helicon plasma between 350 nm and 360 nm ( $N_2$  5 mTorr, 13.56 MHz 800 W). b) Normalized intensity ratio between 357.6 nm and 337.0 nm. Here, only peak intensities of 357.6 nm and 337.0 nm are used without deconvolution.

As mentioned earlier, the selected line-emissions should have small radiation trapping effect. Figure 4-8 verifies that  $N_2$  SNS can be selected from this criterion. In Figure 4-8, line-emissions of 380.4 nm and 337.0 were selected as examples after considering the second and

third requirements of line selection: distinguishable from other emissions and enough SNR. As mentioned earlier, radiation trapping effect has a positive correlation with the density of lower energy state of radiative transition. Also, the population of that energy state generally has positive correlation with electron density, because their major generation source is electron-impact excitation. That is, the increase of electron density can change the line-intensity ratio from same upper energy level, such as  $I_{380.4nm}/I_{337.0nm}$ , by influencing radiation trapping for each emission. However, the normalized line-intensity ratio in Figure 4-8 does not show the variation depending on the increase of electron density. Therefore, it is confirmed that the radiation trapping effect on N<sub>2</sub> SPS can be neglected in low-density/low-pressure plasma.

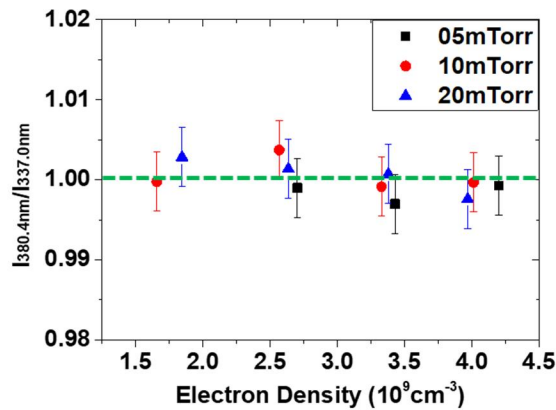
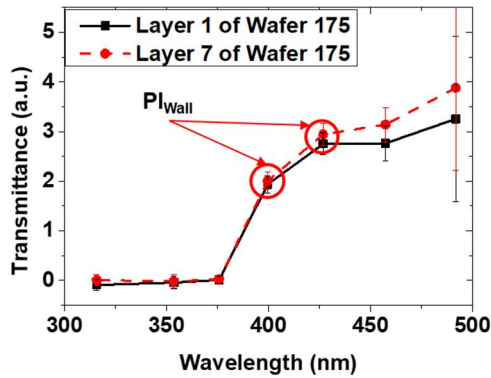


**Figure 4-8.** Normalized intensity ratio to evaluate the influence of radiation trapping on N<sub>2</sub> SPS (Helicon).

Figure 4-9 shows determined transmittance spectrum at contaminated quartz window of multi-layer PECVD by analyzing line-emissions based on equation (4.8). Black rectangle and red circle represent the mean transmittance of first-layer and seventh-layer of wafer 175, respectively. As briefly mentioned earlier, both spectra show very low transmittance values at the wavelength lower than 400 nm, while the drastic increase exists above 400 nm. It deduced from the deposition of a thick oxynitride film on window during pre-coating process. The

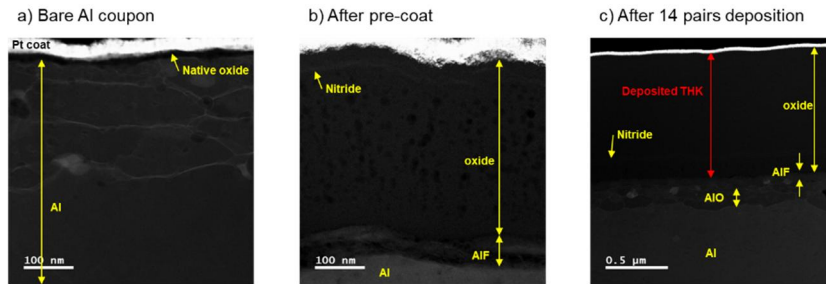
slope of transmittance variation depending on wavelength increases with the layer number, implying the drift of reactor-wall condition during this multi-layer process.

The transmittance spectrum in Figure 4-9 does not show severe interference fringes. Therefore, the variation of reactor-wall condition can be monitored by using the ratio of two line-intensities.  $PI_{Wall}$  is defined as the line-intensity ratio between 426.8 nm and 399.7 nm because they have relatively large SNR as shown in Figure 4-9.



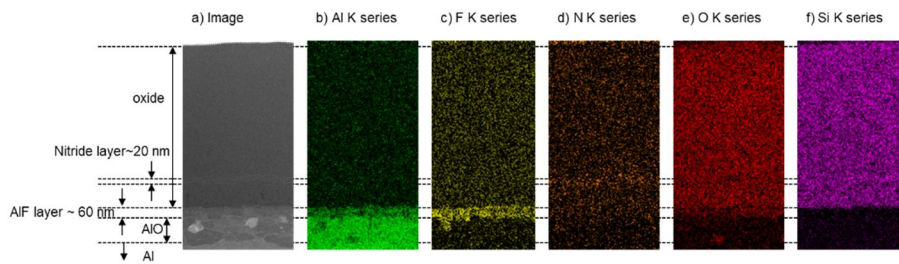
**Figure 4-9.** Transmittance monitoring at contaminated quartz window. (Multi-layer PECVD) The error bar is standard deviation of measured transmittance with in a nitride PECVD.

Figure 4-10 shows the measured STEM image (Dark Field) for coupons established at reactor wall to confirm the component deposited on the reactor wall and its variation during the multi-layer PECVD. Here, very bright region represents Pt coating. Bare Al coupon is composed of Al with native oxide layer (~ 20nm). After pre-coating or PECVD processes, many layers are deposited as shown in Figure 4-10(b) and (c). AlO and AlF layers are originated from dry cleaning step. During pre-coating step, silicon oxide is dominantly deposited and there is a thin nitride layer (~20nm) in the middle of oxide film.



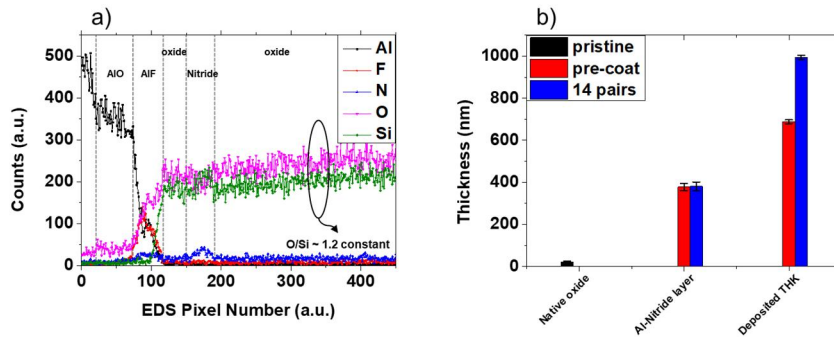
**Figure 4-10.** STEM image for coupons established at reactor wall. a) Bare Al coupon before PECVD. b) deposited coupon after pre-coating process. c) Deposited coupon after 14 pairs nitride/oxide PECVD.

Note that each layer is named by considering its major composition as shown in Figure 4-11. ‘Deposited THK’ is defined as the total thickness of silicon oxide containing nitride layer which means the depth between Pt coating and AIF layer.



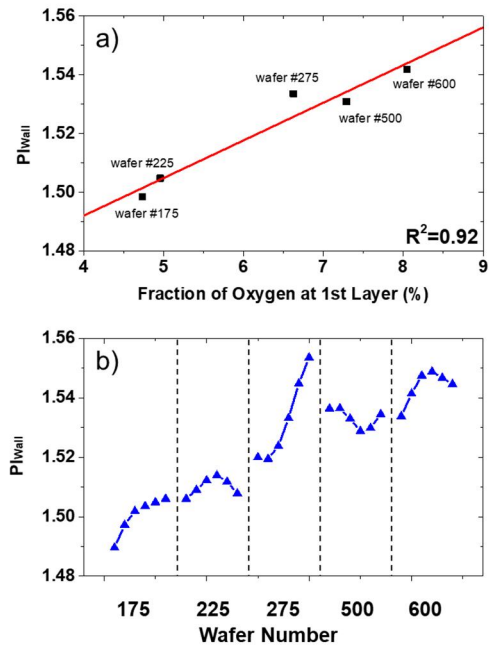
**Figure 4-11.** EDS data for the deposited coupon after 14 pairs nitride/oxide PECVD.

Figure 4-12(a) shows the depth profile of deposited film on reactor wall. In the deposited oxide film, the relative ratio between O and Si is relatively constant. Figure 4-12(b) shows that the pre-coating process deposits the oxide film about 600 nm. It causes the low transmittance values at the wavelength lower than 400 nm in Figure 4-9. Multi-layer PECVD obviously increases the thickness of deposited film on reactor wall as shown the slope variation of transmittance variation depending on wavelength in Figure 4-9.



**Figure 4-12.** Analysis of STEM data. a) Composition of film on reactor wall when 14 pairs nitride/oxide layers are deposited. b) Variation of film thickness on reactor wall.

Figure 4-13(a) shows the correlation between  $F_O$  from EDS analysis and  $PI_{Wall}$ . Here,  $PI_{Wall}$  along the  $y$ -axis is the wafer-averaged value and the  $x$ -axis is  $F_O$ . The red line represents fitted value, showing linear correlation. As explained previously, O data in Figure 3-7 would come from the accumulated residue on reactor-wall. Thus, the high linear correlation with  $R^2 = 0.92$  implies that  $PI_{Wall}$  is a sound indicator for the drift of the reactor-wall condition. Figure 4-13(b) represents the trend of  $PI_{Wall}$  during L2L and W2W processes.  $PI_{Wall}$  increases as the layer number increases. As expected in Figure 4-12, the variation of  $PI_{Wall}$  in L2L process becomes serious because any cleaning process was carried out during multi-layer PECVD processes. For the W2W process, the reactor-wall condition drifts as equipment time increases, leading to the requirement of a stronger cleaning process to maintain the reactor-wall condition consistently.



**Figure 4-13.** Correlation between  $PI_{Wall}$  and  $F_O$  of equation (3.5). (b) Variation of  $PI_{Wall}$  with increasing layer and wafer number. The vertical dash lines are inserted to distinguish each wafer.

## 4.5 Development of monitoring variable for plasma-volume

Plasma *emission* spectroscopy diagnoses properties of non-equilibrium plasma through detailed interpretation of emission spectra with the consideration of the dominant population and depopulation processes of excited states. For molecular spectroscopy, required interpretation is more complex than atomic spectroscopy, because electronic transitions are coupled with vibrational and rotational transition. That is, the vibrational and rotational freedom makes CRM consider many reactions, such as vibrational energy transfer.

Many researchers have been studies Molecular nitrogen ( $N_2$ ) plasma spectroscopy from low-pressure to atmospheric plasma [43-54].  $N_2$  is a predominant constituent of Earth's atmosphere playing a central role in auroras [43], in understanding the kinetics of radicals in the upper atmosphere [44]. Also, low-pressure nitrogen plasma has a wide range of applications in semiconductor industry. For example,  $N_2$  is a part of gas mixture in PECVD for hydrogenated silicon nitride ( $SiN_xH_y$ ) films which are used as a protective layer for integrated circuits [45], a mask layer for selective dry etching [46]. Nitrogen plasma can be used as N atom source for the growth of semiconducting III-V nitrides [47], TiN film growth [48], nitridation process to form oxynitride film [49].

Figure 4-14 shows partial energy diagram for  $N_2$  as a function of internuclear distance [44]. The curves represent specific electronic energy state and gradation of each curve is their vibrational energy states. Here, rotational levels are omitted since their energy gap is too small to represent in figure. For diatomic molecules, the electronic states are labeled with letters: X means ground state, while the excited states with same multiplicity ( $2S+1$ , where  $S$ =total spin)

as the ground state are labeled as A, B, C, and so on, in order of increasing energy [55]. Also, the excited states with different multiplicity from that of ground state are labeled as a, b, c, and so on, in order of increasing energy [55].

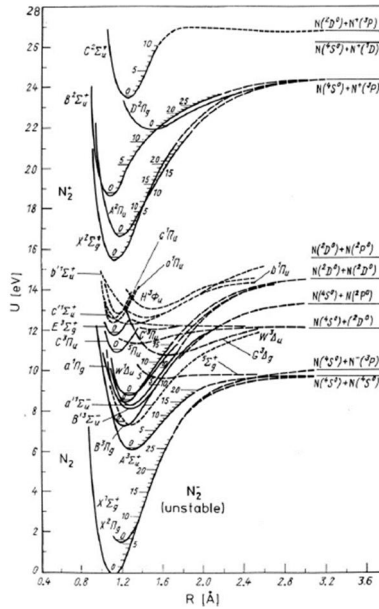


**Figure 4-14.** Partial diagram of potential energy curves of molecular nitrogen [44].  $R$  means internuclear distance.

Figure 4-15 shows partial energy diagram for the first (lowest) vibrational state,  $v=0$ , of each electronic state to easily indicate their threshold energy and important radiations [56]. In the typical low-temperature nitrogen plasma, FPS, SPS and FNS are most intensive radiations. Note that electron-impact excitation from  $N_2(A^3\Sigma_u^+)$  state is one of important excitation mechanism in  $N_2$  plasma since the state is metastable. The radiative life times of FPS, SPS, and FNS are 11.3-3.84  $\mu$ s, 37.1-40.4 ns, and 62.3-87.5 ns, respectively.

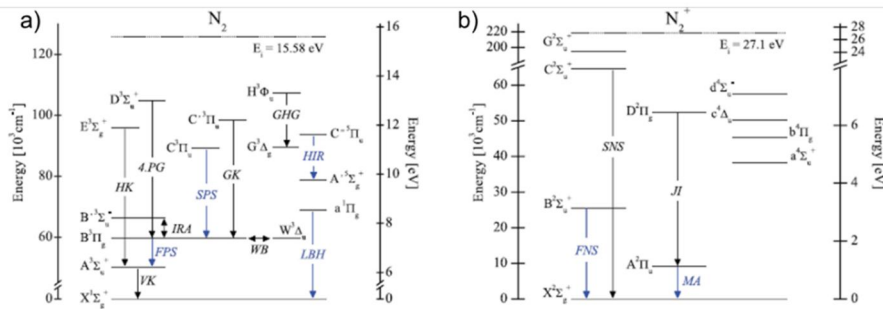


**Figure 4-15.** Partial energy diagram for the first vibrational state of each electronic state [56]. a)  $N_2$ . b)  $N_2^+$ . FPS = first positive system, SPS = second positive system, 4.PG = fourth positive system, VK = Vegard–Kaplan system, IRA = infrared afterglow system, WB = Wu–Benesch system, HK = Herman–Kaplan system, GK = Goldstein–Kaplan system, GHG = Gaydon–Herman Green system, HIR = Herman infrared system, LBH = Lyman–Birge–Hopfield. FNS = first negative system, SNS = second negative system, JI = Janin–d’Incan system and MA = Meinel’s auroral system. Radiative transitions important for optical diagnostics are highlighted in blue

Studies for  $N_2$  plasma spectroscopy generally analyzed the emission from  $N_2$  FPS, SPS or FNS by using CRM to determine electron density and electron temperature [50-54].

Non-Maxwellian EEDF of DC glow discharge (50-500 mTorr) was calculated by using  $N_2$  SPS and  $N_2$  FNS [51]. Here, electron temperature in low energy region was determined by using population ratio between  $N_2(C^3\Pi_u, \nu = 4)$  and  $N_2(C^3\Pi_u, \nu = 0)$  states. The tail of EEDF was determined by using population ratio between  $N_2^+(B^2\Sigma_u^+, \nu = 0)$  and  $N_2(C^3\Pi_u, \nu = 0)$  states. Electric field (E-field) and relative electron density ( $n_e(x,t)/n_{e,max}$  where  $x$ =position) of atmospheric dielectric barrier discharge (AP-DBD) was determined by using population ratio between  $N_2^+(B^2\Sigma_u^+, \nu = 0)$  and  $N_2(C^3\Pi_u, \nu = 0)$  states [52]. Also, E-field and electron density of DC glow discharge and microwave discharge (0.5-10 Torr) was determined by using VDF of  $N_2(C^3\Pi_u, \nu = 0-4)$  states and Boltzmann equation [53]. The electron density and electron temperature of pulsed DC glow discharge (2-4 Torr) was determined by using population ratio

between  $N_2^+(B^2\Sigma_u^+, \nu = 0)$  and  $N_2(C^3\Pi_u, \nu = 0)$  with one calibration point of electron density and electron temperature which had been determined by using Langmuir probe [54]. A CRM was proposed to determine electron density and electron temperature in wide pressure range (0.01-760Torr), although experimental validation was only performed in the limited range [50]. The idea was that the population ratio between  $N_2(C^3\Pi_u, \nu = 1)$  and  $N_2(C^3\Pi_u, \nu = 0)$  is sensitive to the variation of electron density because the population ratio is affected by VDF of  $N_2(X^1\Sigma_g^+, \nu)$  state which is a sensitive function of electron density. The study also used the fact that the total population ratio between  $N_2(C^3\Pi_u, \nu = 0-4)$  and  $N_2(B^3\Pi_g, \nu' = 0-21)$  states are sensitive to electron temperature due to their large difference of threshold energy.

There are some limitations in previous studies to monitor the variation of PI variables in plasma-assisted process for semiconductor manufacturing. First, the studies used  $N_2$  FNS without considering step-excitation from ground state of  $N_2^+$  ion. It degrades the reliability of emission model because the step-excitation from  $N_2^+$  ion obviously causes the variation of emission intensity as shown in Figure 4-7. Second, total population of  $N_2(B^3\Pi_g, \nu' = 0-21)$  state is practically hard to determine in plasma-assisted process, because superposition of emission intensities with emissions from other gases makes it difficult to independently detect 22 different emissions (from different vibrational number,  $\nu' = 0-21$ ).

In this thesis, VDF of  $N_2(C^3\Pi_u, \nu = 0-4)$  states is used to determine electron density and temperature as a solution for the problem of measuring the total population of  $N_2(B^3\Pi_g, \nu' = 0-21)$  state. Also, relatively large intensity and small radiation trapping effect of  $N_2$  SPS helps the simplification of CRM. Figure 4-16 and Table 4-2 show used line-intensities and their information, respectively. The line-intensities from different upper energy levels are selected because their different threshold energy offer different sensitivity to electron density and electron temperature. Especially, the population ratio between  $N_2(C^3\Pi_u, \nu = 1)$  and  $N_2(C^3\Pi_u, \nu$

= 0) is relatively insensitive to electron temperature, because of their small energy difference. On the other hand, the population ratio between  $N_2(C^3\Pi_u, \nu = 4)$  and  $N_2(C^3\Pi_u, \nu = 0)$  is relatively sensitive to the electron temperature due to their relatively large energy difference.

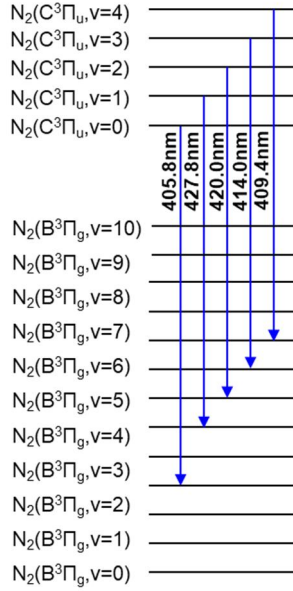


**Figure 4-16.** Wavelengths of  $N_2$  SPS to determine  $PI_{Volume}$ .

**Table 4-2.** Information about line-intensities used to monitor  $PI_{Volume}$ . Headings are the same as for Table 4-1.

Again, all information is based on [42]

<b>Transition</b>	<b><math>\lambda</math> (nm)</b>	<b><math>A_{pk}</math> (<math>10^6 s^{-1}</math>)</b>
$N_2(C^3\Pi_u, \nu=0) \rightarrow N_2(B^3\Pi_g, \nu=3)$	405.8	1.10
$N_2(C^3\Pi_u, \nu=1) \rightarrow N_2(B^3\Pi_g, \nu=5)$	426.8	0.898
$N_2(C^3\Pi_u, \nu=2) \rightarrow N_2(B^3\Pi_g, \nu=6)$	420.0	1.57
$N_2(C^3\Pi_u, \nu=3) \rightarrow N_2(B^3\Pi_g, \nu=7)$	414.0	2.01
$N_2(C^3\Pi_u, \nu=4) \rightarrow N_2(B^3\Pi_g, \nu=8)$	409.4	2.09

The electron density and electron temperature (defined as  $PI_{\text{Volume}}$  in this thesis) can be determined by analyzing the VDF of  $N_2(C^3\Pi_u, \nu = 0-4)$  states whose excitation rate have different function depending on electron density and electron temperature. In low-pressure and low-temperature plasma,  $N_2(C^3\Pi_u, \nu = 0-4)$  states are produced by the electron-impact excitation from vibrationally excited ground states,  $N_2(X^1\Sigma_g^+, \nu)$ , and from vibrationally excited metastable states,  $N_2(A^3\Sigma_u^+, \nu)$ . Also,  $N_2(X^1\Sigma_g^+, \nu)-N_2(A^3\Sigma_u^+, \nu)$  and  $N_2(A^3\Sigma_u^+, \nu)-N_2(A^3\Sigma_u^+, \nu)$  reactions produces  $N_2(C^3\Pi_u, \nu = 0-4)$  states. Then the excited  $N_2(C^3\Pi_u, \nu = 0-4)$  states are destructed by radiative decay and collisional quenching by ground states. That is, to expect VDF of  $N_2(C^3\Pi_u, \nu = 0-4)$  states depending on electron density and electron temperature, VDF of ground and metastable state of  $N_2$  should be determined simultaneously (Figure 4-17).

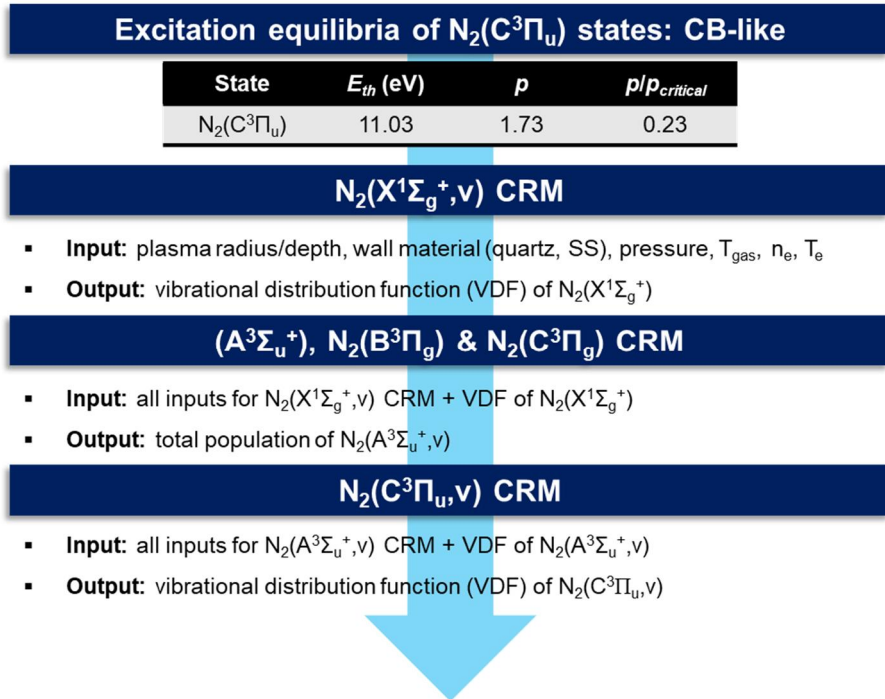


**Figure 4-17.** Flow chart of  $N_2$  CRM to determine PI variables.

VDF of ground state is influenced by electron impact vibrational excitation/de-excitation, vibrational energy transfer, and wall deactivation. Note that vibrational energy transfer and wall deactivation reactions are important for vibrational excited ground states because they are non-radiative state. Metastable states are generated by electron-impact excitation from ground state, radiative decay, and collisional quenching from  $N_2(B^3\Pi_g, \nu)$  states. They are destructed by wall deactivation, collisional quenching with  $N_2(X^1\Sigma_g^+, \nu)$ , metastable pooling reactions which means collision reactions between  $N_2(A^3\Sigma_u^+, \nu)$  states.

The major processes considered in  $N_2$  CRM are described in Table 4-3. Particle balance for each vibrational state of  $N_2(X^1\Sigma_g^+)$  can be expressed as:

$$\begin{aligned}
& n_e \sum_{\nu \neq \nu'} n_{X,\nu'} Q_{e-N_2}^{\nu' \rightarrow \nu} + n_{X,\nu-1} \sum_{\nu \neq \nu'} n_{X,\nu'} Q_{N_2(X)-N_2(X)}^{\nu-1, \nu'+1 \rightarrow \nu, \nu'} + n_{X,\nu+1} \sum_{\nu \neq \nu'} n_{X,\nu'} Q_{N_2(X)-N_2(X)}^{\nu+1, \nu' \rightarrow \nu, \nu'+1} + K_{wall}^{\nu+1 \rightarrow \nu} n_{X,\nu+1} \\
& = n_e n_{X,\nu} \sum_{\nu \neq \nu'} Q_{e-N_2}^{\nu \rightarrow \nu'} + n_{X,\nu} \sum_{\nu'} n_{X,\nu'+1} Q_{N_2(X)-N_2(X)}^{\nu, \nu'+1 \rightarrow \nu+1, \nu'} + n_{X,\nu} \sum_{\nu'} n_{X,\nu'} Q_{N_2(X)-N_2(X)}^{\nu, \nu' \rightarrow \nu-1, \nu'+1} + K_{wall}^{\nu \rightarrow \nu-1} n_{X,\nu}
\end{aligned} \tag{4.10}$$

where,  $n_e$  is the electron density;  $n_{X,\nu}$  is  $N_2$  ground state density with vibrational number  $\nu$ , and meaning of all rate constants are described in Table 4-3. The terms in LHS and RHS of equation (4.10) represent electron-impact vibrational excitation/de-excitation (1<sup>st</sup> term), ground state vibrational energy transfer (2<sup>nd</sup>, 3<sup>rd</sup> terms), and wall deactivation (4<sup>th</sup> term), respectively. Note that 41 vibrational states ( $\nu=0-40$ ) are considered in this calculation; that rate constant for electron-impact reaction has the same form with equation (4.4); and that all notation without vibrational quantum number represent sum of all vibrational states in specific electronic state. Total particle density of  $N_2$  molecule is assumed as a sum of vibrationally excited ground states, because low-pressure/temperature plasma has very small density of electronic excited states:

$$n_{N_2, total} = P_{N_2} / kT_{gas} = \sum_v n_{X,v} , \quad (4.11)$$

where,  $n_{N_2, total}$  is total particle density of  $N_2$  molecule,  $P_{N_2}$  is partial pressure of  $N_2$  (Torr),  $k$  is Boltzmann constant,  $T_{gas}$  is gas temperature (Kelvin). Above equations (4.10) and (4.11) can determine VDF of  $N_2(X^1\Sigma_g^+)$  state as a function of plasma dimension (radius or depth), property of wall material, partial pressure of  $N_2$ , gas temperature, electron density and electron temperature. The reason the plasma dimension and property of wall material is a part of input variables will be discussed with reaction rates.

Then total population of  $N_2(A^3\Sigma_u^+)$ ,  $N_2(B^3\Pi_g)$  and  $N_2(C^3\Pi_u)$  states are described by using VDF of grounds state determined from equation (4.10) and (4.11) with given electron density and electron temperature:

$$\begin{pmatrix} K_{wall}^{A \rightarrow X} + Q_{N_2(A)-N_2(X)} n_{X,v} & -A_B - Q_{N_2(B)-N_2(X)} n_X & 0 \\ -Q_{N_2(A)-N_2(X)} n_{X,v} & A_B + Q_{N_2(B)-N_2(X)} n_X & -A_C \\ 0 & 0 & A_C + Q_{N_2(C)-N_2(X)} n_X \end{pmatrix} \begin{pmatrix} n_A \\ n_B \\ n_C \end{pmatrix} \quad (4.12)$$

$$= n_e n_X \begin{pmatrix} Q_A \\ Q_B \\ Q_C \end{pmatrix} - n_A n_A \begin{pmatrix} 2(Q_{N_2(B)-N_2(X)} + Q_{N_2(C)-N_2(X)}) \\ -Q_{N_2(A)-N_2(A)B} \\ -Q_{N_2(C)-N_2(A)} \end{pmatrix}$$

where meaning of all rate constants are described in Table 4-3. In the development of equation (4.12), it is assumed that metastable state is mainly generated by electron-impact excitation; by radiative decay and collisional quenching from  $N_2(B^3\Pi_g)$  state. Wall-deactivation and metastable pooling reactions destruct the metastable state.  $N_2(B^3\Pi_g)$  state is generated by electron-impact excitation; by radiative decay from  $N_2(C^3\Pi_u)$ ; by excitation transfer; and by metastable pooling reaction. Then  $N_2(B^3\Pi_g)$  state is destructed by radiative decay and collisional quenching.  $N_2(C^3\Pi_u)$  state is generated by electron-impact excitation and metastable pooling reactions. Then  $N_2(C^3\Pi_u)$  state is destructed dominantly radiative decay with small contribution of collisional quenching. Above equation (4.12) can determine the

total population of  $N_2(A^3\Sigma_u^+)$ ,  $N_2(B^3\Pi_{g,2})$  and  $N_2(C^3\Pi_u)$  states as a function of VDF of  $N_2(X^1\Sigma_g^+)$  states, plasma dimension, property of wall material, partial pressure of  $N_2$ , gas temperature, electron density and electron temperature.

Table 4-3. Used reaction rates for N<sub>2</sub> CRM.

Classification	Formula	Notation	Note
Electron-impact vibrational excitation/de-excitation (ground)	$e+N_2(X^1\Sigma_g^+, v) \leftrightarrow e+N_2(X^1\Sigma_g^+, v')$	$Q_{e-N_2}^{v \rightarrow v'}$	[57]
Electron-impact electronic excitation/de-excitation (ground)	$e+N_2(X^1\Sigma_g^+, v) \leftrightarrow e+N_2(B^3\Pi_g^-/C^3\Pi_u, v')$	$Q_{e-N_2}^{X,v \rightarrow B/C,v'}$	[58]
Electron-impact electronic excitation/de-excitation (metastable)	$e+N_2(A^3\Sigma_u^+, v) \leftrightarrow e+N_2(C^3\Pi_u, v')$	$Q_{e-N_2(A)}^{A,v \rightarrow C,v'}$	[59]
Ground state vibrational energy transfer	$N_2(X^1\Sigma_g^+, v) + N_2(X^1\Sigma_g^+, v') \leftrightarrow N_2(X^1\Sigma_g^+, v-1) + N_2(X^1\Sigma_g^+, v'+1)$	$Q_{N_2(X)-N_2(X)}^{v,v' \rightarrow v-1,v'+1}$	[60]
Wall deactivation (ground)	$N_2(X^1\Sigma_g^+, v) \rightarrow N_2(X^1\Sigma_g^+, v-1)$	$K_{wall}^{v \rightarrow v-1}$	SUS [61] Quartz [62]
Wall deactivation (metastable)	$N_2(A^3\Sigma_u^+, v) \rightarrow N_2(A^3\Sigma_u^+, v-1)$	$K_{wall}^{A \rightarrow X}$	[50]
Excitation transfer	$N_2(A^3\Sigma_u^+) + N_2(X^1\Sigma_g^+, 5 \leq v \leq 14) \rightarrow N_2(B^3\Pi_g^-) + N_2$	$Q_{N_2(A)-N_2(X)}$	[63]
Collisional quenching of N <sub>2</sub> (B <sup>3</sup> Π <sub>g</sub> )	$N_2(B^3\Pi_g^-) + N_2 \rightarrow N_2(A^3\Sigma_u^+) + N_2$	$Q_{N_2(B)-N_2(X)}$	[63]
Collisional quenching of N <sub>2</sub> (C <sup>3</sup> Π <sub>u</sub> , v)	$N_2(C^3\Pi_u, v) + N_2 \rightarrow N_2(B^3\Pi_g^-/A^3\Sigma_u^+) + N_2$	$Q_{N_2(C)-N_2(X)}$ or $Q_{N_2(C)-N_2(X)}^v$	[64]
Radiative decay from N <sub>2</sub> (B <sup>3</sup> Π <sub>g</sub> , v)	$N_2(B^3\Pi_g^-) \rightarrow N_2(A^3\Sigma_u^+) + hc/\lambda$	$A_B$ or $A_B^{v \rightarrow v'}$	[63]
Radiative decay from N <sub>2</sub> (C <sup>3</sup> Π <sub>u</sub> , v)	$N_2(C^3\Pi_u) \rightarrow N_2(B^3\Pi_g^-) + hc/\lambda$	$A_C$ or $A_C^{v \rightarrow v'}$	[63]
Metastable pooling to N <sub>2</sub> (B <sup>3</sup> Π <sub>g</sub> , v)	$N_2(A^3\Sigma_u^+) + N_2(A^3\Sigma_u^+) \rightarrow N_2(B^3\Pi_g^-) + N_2(X^1\Sigma_g^+, v=8)$	$Q_{N_2(A)-N_2(A)}^{N_2(B)-N_2(X)}$	[63]
Metastable pooling to N <sub>2</sub> (C <sup>3</sup> Π <sub>u</sub> , v)	$N_2(A^3\Sigma_u^+) + N_2(A^3\Sigma_u^+) \rightarrow N_2(C^3\Pi_u) + N_2(X^1\Sigma_g^+, v=2)$	$Q_{N_2(A)-N_2(A)}^{N_2(C)-N_2(X)}$	[63]

(vibrationally resolved) Metastable	$N_2(A^3\Sigma_u^+, \omega) + N_2(A^3\Sigma_u^+, \omega')$	$Q_{N_2(A)-N_2(A)}^{C,v}$	[65]
pooling to $N_2(C^3\Pi_u, v)$	$\rightarrow N_2(C^3\Pi_u, v) + N_2$		

Finally, population of each vibrational state of  $N_2(C^3\Pi_u, v)$  states can be described by using its particle balance:

$$\begin{aligned}
& n_{C,v} \left( \sum_{v'} A_C^{v \rightarrow v'} + Q_{N_2(C)-N_2(X)}^v \right) \\
& = n_e \sum_{v'} n_{X,v'} Q_{e-N_2}^{X,v' \rightarrow C,v} + n_e \sum_{\omega} n_{A,\omega} Q_{e-N_2(A)}^{A,\omega \rightarrow C,v} + \sum_{\omega, \omega'} n_{A,\omega} n_{A,\omega'} Q_{N_2(A)-N_2(A)}^{C,v} \quad (4.13)
\end{aligned}$$

The terms in LHS represent radiative decay and collisional quenching, respectively. The terms in RHS represent electron-impact excitation from ground and metastable state, and metastable pooling reaction, respectively. Equation (4.13) can describe VDF of  $N_2(C^3\Pi_u)$  states as a function of function of VDF of  $N_2(A^3\Sigma_u^+)$  states, VDF of  $N_2(X^1\Sigma_g^+)$  states, plasma dimension, property of wall material, partial pressure of  $N_2$ , gas temperature, electron density and electron temperature. That is, VDF of  $N_2(A^3\Sigma_u^+)$  state should be determined to describe VDF of  $N_2(C^3\Pi_u)$  states as a function of electron density and electron temperature, although equation (4.12) can only determine total population of  $N_2(A^3\Sigma_u^+)$  state. As will be described later again, this thesis assumed vibrational temperature of  $N_2(A^3\Sigma_u^+)$  state to represent total population of  $N_2(A^3\Sigma_u^+)$  state as VDF of  $N_2(A^3\Sigma_u^+)$  state.

Among rate constant in Table 4-3, vibrational energy transfer was determined as follows. The vibrational energy transfer can be described as [60]:

$$\begin{aligned}
& Q_{N_2(X)-N_2(X)}^{v,v' \rightarrow v-1,v'+1} \\
& = Z \cdot z(v) \cdot z(v'+1) \cdot \exp\left(-\frac{\Delta E}{2kT_{gas}}\right) \cdot \left\{ a(T_{gas}) \cdot T_{gas} \cdot f(y) + \frac{b(T_{gas})}{T_{gas}} \cdot \exp\left(\frac{\Delta E^2}{CkT_{gas}}\right) \right\} \quad (4.14)
\end{aligned}$$

where  $Z$  is gas kinetic collision rate constant ( $\text{cm}^3/\text{s}$ );  $z(v)$  is a dimensionless variable (Equation (4.17));  $\Delta E$  is the energy mismatch of the transition (K);  $k$  is Boltzmann constant

(J·s);  $a(T_{gas})$  and  $b(T_{gas})$  are temperature-dependent variable;  $f(y)$  is adiabatic function (Equation (4.19));  $y$  is a dimensionless variable;  $C$  is effective width of the resonant function (K). Here,  $Z$  is described as:

$$Z = \pi \sigma^2 V_M, \quad (4.15)$$

where  $\sigma$  is gas kinetic collision cross section ( $\text{cm}^2$ );  $V_M$  is average translational velocity ( $\text{cm/s}$ ) defined as:

$$V_M = \sqrt{\frac{8kT_{gas}}{\pi M_R}} \times 100 \text{ [cm/s]}, \quad (4.16)$$

where  $M_R$  is reduced mass. A dimensionless variable,  $z(v)$ , is defined as:

$$z(v) = \frac{v}{1 - v \cdot \delta}, \quad (4.17)$$

where  $\delta$  is anharmonicity, well-known as  $\chi_e$  in various literatures.  $\Delta E$  is defined as:

$$\Delta E = E_{th}(v) + E_{th}(v') - E_{th}(v-1) - E_{th}(v'+1), \quad (4.18)$$

where  $E_{th}$  is threshold energy from  $\text{N}_2(\text{X}^1\Sigma_g^+, v=0)$ . Also,  $f(y)$  is defined as:

$$\begin{aligned} f(y) &= 0.5 \cdot \exp(-2y/3) \cdot \{3 - \exp(-2y/3)\}, \text{ for } y < 21.622 \\ f(y) &= 8 \cdot (\pi/3)^{1/2} y^{7/2} \exp(-3y^{2/3}), \text{ for } y \geq 21.622 \end{aligned}, \quad (4.19)$$

where  $y$  is defined as:

$$y = l_{ST} \cdot |\Delta E| \cdot \pi^2 \sqrt{\frac{2M_R k}{h^2 T_{gas}}}, \quad (4.20)$$

where  $l_{ST}$  is specific length of the SR exponential repulsive potential  $\exp(-x/l_{ST})$  in SSH theory (m);  $h$  is Planck constant ( $\text{JK}^{-1}$ ). However, in the previous study [60], constants are not explicitly presented, and units are not matched reasonably. Therefore, this thesis changed the equation (4.14) as:

$$Q_{N_2(X) \rightarrow N_2(X)}^{v, v' \rightarrow v-1, v'+1} = Z \cdot z(v) \cdot z(v'+1) \cdot \exp\left(\frac{\Delta E}{2T_{gas}}\right) \cdot \left\{ a(T_{gas}) \cdot T_{gas} \cdot f(y) + \frac{b(T_{gas})}{T_{gas}} \cdot \exp\left(\frac{\Delta E^2}{CT_{gas}}\right) \right\} \quad (4.21)$$

Also, this thesis used the constants as follows:  $\sigma = 3.82 \times 10^{-15} \text{ cm}^2$ ,  $M_R = 2.33 \times 10^{-26} \text{ kg}$ ,  $\delta = 0.006126$  [66]. Wall deactivation rate constant is defined as [33]:

$$K_{wall} = \left[ \frac{\Lambda_0^2}{D_0} + \frac{2V(2-\gamma)}{A\bar{v}_{N_2}\gamma} \right]^{-1}, \quad (4.22)$$

where  $\Lambda_0$  is the effective diffusion length,  $D_0$  is the neutral diffusion coefficient, and  $V$  is plasma volume,  $A$  is surface area for loss,  $\bar{v}_{N_2}$  is mean velocity of  $N_2$  molecule,  $\gamma$  is reaction probability at surface (in this case, deactivation probability). Here,  $\Lambda_0$  is expressed as:

$$\Lambda_0 = \left[ \left(\frac{\pi}{L}\right)^2 + \left(\frac{2.405}{R}\right)^2 \right]^{-1/2}, \quad (4.23)$$

where  $L$  is depth and  $R$  is radius of plasma (cylindrical). Also,  $D_0$  can be expressed for  $N_2$  molecule in  $N_2$  environment [67]:

$$D_0 = \frac{eT_{gas}\lambda_{N_2}}{\bar{v}_{N_2}m_{N_2}} \rightarrow D_{N_2-N_2} \approx \frac{7 \times 10^{18}}{n_{N_2}} \left(\frac{T_{gas}}{300}\right)^{0.92} [\text{cm}^2\text{s}^{-1}]. \quad (4.24)$$

Equation (4.22) represents loss rate of reactive species through transport to reactor wall. Specifically, the first term represents the inverse of diffusion rate for transport of molecules to the reactor wall, and the second term represents the inverse of the loss rate at walls. That is, loss rate of reactive species is influenced by operating pressure which determines diffusion rate, dimension of reactor or plasma volume, and reaction rate at reactor wall. Therefore, the plasma dimension and property of wall material is important part of input variables to determine VDF of non-radiative states, such as  $N_2(X^1\Sigma_g^+)$  and  $N_2(A^3\Sigma_u^+)$  states.

To solve equation (4.10) through (4.13), some important assumptions are required. This thesis assumed followings:

- (1) Gas temperature is same as the hottest boundary. (Heater temperature)
- (2) Vibrational temperature of  $N_2(A^3\Sigma_u^+)$  state is 2000 K (following [65]).
- (3) EEDF is Maxwellian.

These assumptions can be loosened through detailed analysis of additional emissions. For example, gas temperature can be determined by analyzing rotational spectrum of  $N_2$  SPS, FPS or FNS [56]. Assumption about vibrational temperature can be removed by solving vibrational resolved kinetic equations, although uncertainty of cross sections is much larger than unresolved cross sections. Development of monitoring method for gas temperature, vibrational resolved kinetic model, and non-Maxwellian EEDF can be the subject of future studies.

Substituting equation (4.13) into equation (4.1) after relative intensity calibration of spectroscopic system and correction of transmittance, line-intensity from specific vibrational state of  $N_2(C^3\Pi_u, \nu)$  is described as a function of its population density:

$$\begin{aligned}
I_{C,\nu} &\propto n_{C,\nu} A_C^{\nu \rightarrow \nu'} \\
&= \frac{A_C^{\nu \rightarrow \nu'}}{\sum_{\nu'} A_C^{\nu \rightarrow \nu'} + Q_{N_2(C)-N_2(X)}^\nu} \left( n_e \sum_{\nu'} n_{X,\nu'} Q_{e-N_2}^{X,\nu' \rightarrow C,\nu} + n_e \sum_{\omega} n_{A,\omega} Q_{e-N_2(A)}^{A,\omega \rightarrow C,\nu} \right) \cdot \quad (4.25) \\
&\quad + \sum_{\omega,\omega'} n_{A,\omega} n_{A,\omega'} Q_{N_2(A)-N_2(A)}^{C,\nu}
\end{aligned}$$

Then, intensity-ratio between  $N_2(C^3\Pi_u, \nu)$  and  $N_2(C^3\Pi_u, \nu=0)$  is described as follows:

$$\begin{aligned}
\frac{I_{C,\nu}}{I_{C,\nu=0 \rightarrow B,\nu=3}} &= \frac{\sum_{\nu'} A_C^{0 \rightarrow \nu'} + Q_{N_2(C)-N_2(X)}^0}{A_C^{0 \rightarrow 3}} \frac{A_C^{\nu \rightarrow \nu'}}{\sum_{\nu'} A_C^{\nu \rightarrow \nu'} + Q_{N_2(C)-N_2(X)}^\nu} \\
&\quad \frac{n_e \sum_{\nu'} n_{X,\nu'} Q_{e-N_2}^{X,\nu' \rightarrow C,\nu} + n_e \sum_{\omega} n_{A,\omega} Q_{e-N_2(A)}^{A,\omega \rightarrow C,\nu} + \sum_{\omega,\omega'} n_{A,\omega} n_{A,\omega'} Q_{N_2(A)-N_2(A)}^{C,\nu}}{n_e \sum_{\nu'} n_{X,\nu'} Q_{e-N_2}^{X,\nu' \rightarrow C,0} + n_e \sum_{\omega} n_{A,\omega} Q_{e-N_2(A)}^{A,\omega \rightarrow C,0} + \sum_{\omega,\omega'} n_{A,\omega} n_{A,\omega'} Q_{N_2(A)-N_2(A)}^{C,0}} \quad (4.26)
\end{aligned}$$

VDF of  $N_2(C^3\Pi_u)$  states depending on electron density and temperature is obtained numerically. Then electron density, electron temperature, and  $N_2$  metastable density are

determined numerically to minimize the absolute error (AE) between measured and expected intensity ratios:

$$AE = \sum_v \left| 1 - \left( \frac{I_{C,v}}{I_{C,v=0 \rightarrow B,v=3}} \right)_{\text{expected}} / \left( \frac{I_{C,v}}{I_{C,v=0 \rightarrow B,v=3}} \right)_{\text{Measured}} \right|. \quad (4.27)$$

Figure 4-18 shows a sample of expectation by using N<sub>2</sub> CRM (1<sup>st</sup> layer at wafer #175). Figure 4-18(a) shows that N<sub>2</sub> CRM well describes the measured VDF of N<sub>2</sub>(C<sup>3</sup>Π<sub>u</sub>) state. In Figure 4-18(b), one can see that each vibrational state has different weighting of production mechanism. Specifically, N<sub>2</sub>(C<sup>3</sup>Π<sub>u</sub>, v=0) and N<sub>2</sub>(C<sup>3</sup>Π<sub>u</sub>, v=1) states are mainly produced by electron-impact excitation mechanism. As vibrational number increases, excitation from metastable state has large percentage of production due to its high threshold energy. These properties directly show that line-intensity ratio from different vibrational state can determine electron density and temperature because of followings: (1) The population ratio between N<sub>2</sub>(C<sup>3</sup>Π<sub>u</sub>, v=0) and N<sub>2</sub>(C<sup>3</sup>Π<sub>u</sub>, v=1) state is sensitive to electron density but insensitive to electron temperature because the difference of threshold energy is small. (2) The population ratio between N<sub>2</sub>(C<sup>3</sup>Π<sub>u</sub>, v=0) and higher vibrational states are sensitive to electron temperature because higher vibrational states are mainly produced by ‘eA’ or ‘AA’ reactions while N<sub>2</sub>(C<sup>3</sup>Π<sub>u</sub>, v=0) state is mainly produced by ‘eV’ reaction.

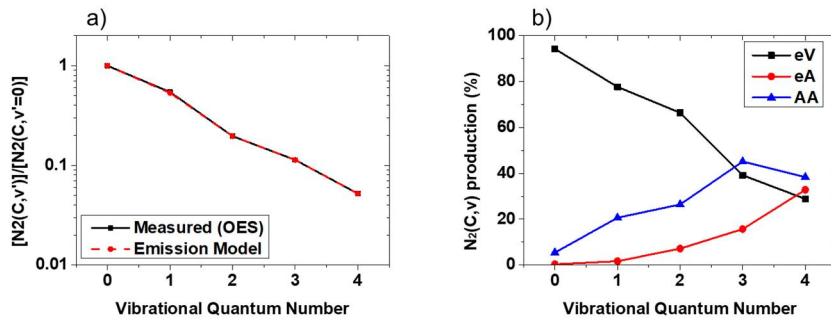


**Figure 4-18.** Determination of PI<sub>Volume</sub> by using N<sub>2</sub> CRM for 1<sup>st</sup> layer at wafer #175. a) Determined VDF by using emission model. b) Percentage of production for each vibrational state. ‘eV’, ‘eA’, and ‘AA’ represent electron-impact

excitation from ground state, that from metastable state, and metastable pooling reaction, respectively.

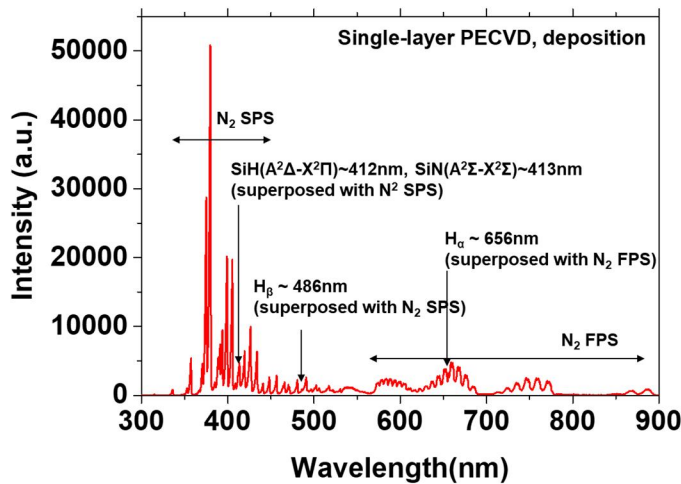
## Chapter 5 . Application of PI-VM to Predict the Property of Nitride Film

PI-VM is developed to predict the property of nitride film on silicon wafer. As mentioned earlier, it is chosen due to following reasons: (1) Severe process drift can exist due to larger amount of deposition on reactor-wall during the process than that of etching process. (2)  $N_2$  gas in nitride PECVD can offer reliable reaction cross sections to determine PI variables. (3)  $N_2$  plasma is used in a wide pressure range from low-pressure to atmospheric pressure [43-49].

In this chapter, PI-VM for nitride PECVD is constructed based on PI variables determined in Chapter 4. The meaning of PI variables on the property of nitride film deposition can be analyzed by using PI-VM for single-layer PECVD and the growth mechanism of nitride film:  $SiN_xH_y$  film is grown by the nitridation of a thin a-Si:H layer and refractive index has a positive correlation with Si/N ratio [68]. Finally, PI-VM is applied to predict layer-to-layer nitride film thickness in nitride/oxide multi-layer PECVD for the mass production. The performance of PI-VM is evaluated by using equation (3.1) - (3.4).

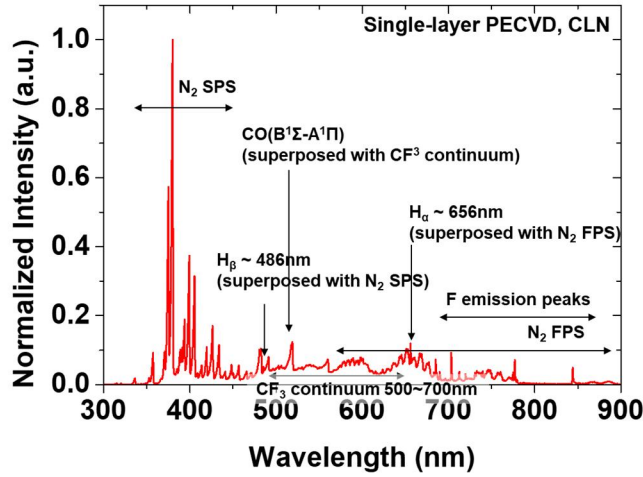
## 5.1 PI-VM for nitride film in single-layer PECVD

Figure 5-1 shows an example of measured emission spectrum of deposition step in single-layer PECVD. Emissions from nitrogen molecule ( $N_2$  SPS,  $N_2$  FPS) are most intensive lines in spectrum.  $SiH_4$  and  $NH_3$  gases induce hydrogen ( $H_\alpha$ ,  $H_\beta$ ),  $SiH$  ( $A^2\Delta-X^2\Pi$ ), and  $SiN$  ( $A^2\Sigma-X^2\Sigma$ ) emissions. Note that these emissions are superposed with nitrogen emissions.



**Figure 5-1.** Measured emission spectrum of deposition step in single-layer nitride PECVD (4 Torr, 13.56 MHz 720 W, and  $N_2$  3000sccm).

Figure 5-2 shows example of measured emission spectrum of cleaning step in single-layer nitride PECVD. Like Figure 5-1, emissions from nitrogen molecule ( $N_2$  SPS,  $N_2$  FPS) are most intensive in spectrum with hydrogen ( $H_\alpha$ ,  $H_\beta$ ) emissions.  $CF_4$  gas for etching deposited wall induces  $CF_3$  continuum band (500-700nm), atomic F lines, and CO band.



**Figure 5-2.** Measured emission spectrum of cleaning step in single-layer nitride PECVD.

Figure 5-3 shows wafer-averaged nitride thickness (THK), refractive index ( $n$ ), and extinction coefficient ( $k$ ) depending on recipe. Here,  $n$  and  $k$  are measured at 633nm. From Figure 5-3, it is confirmed that power, pressure, and  $N_2$  flow rate offer a positive influence on the thickness of nitride film while negative influence on both refractive index and extinction coefficient. On the other hand, deposition time only increases nitride thickness without affecting refractive index. Note that refractive index will be used in analyzing the composition of nitride film based on following equation [69]:

$$\frac{[Si]}{[N]} = 0.278n^2 - 0.205n + 0.0719, \quad (5.1)$$

where a square bracket represents the concentration of each component in film. Equation (5.1) means that  $n$  of nitride film has positive correlation with Si/N ratio in film and its value is between 1.9 for  $Si_3N_4$  and 3.3 for a-Si:H while high H content in nitride film can also decrease  $n$ . It causes that  $n$  of nitride film increases from 1.9 to 3.3 as partial composition of N decreases.

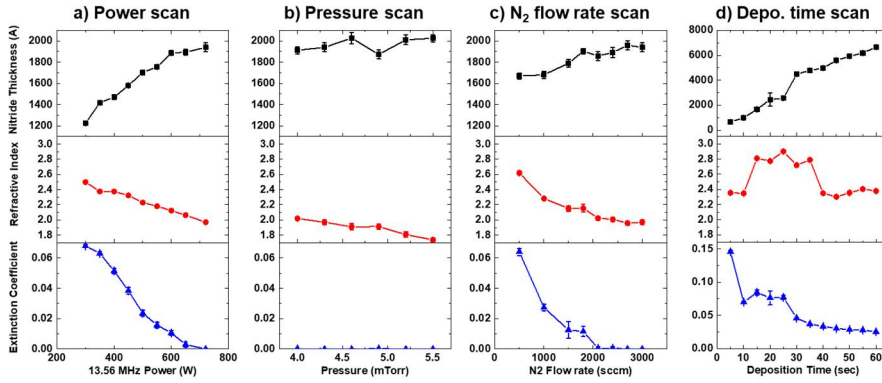


**Figure 5-3.** Wafer state variables depending on process condition. a) power scan. b) pressure scan. c)  $N_2$  flow rate scan. d) deposition time scan. Values in figure are wafer-averaged. Detailed recipes are shown in Table 3-2.

Figure 5-4 shows uniformity of THK and  $n$  depending on recipe. Here, all values are normalized by that of wafer center-position (measurement position=1). The nitride THK is the highest in the center position and the uniformity remains within 5%. As wafer-averaged values, the nitride THK and refractive index has opposite trend because the film is deposited by the nitridation of thin a-Si:H layer [68]. It implies that increasing the deposition thickness reduces [Si]/[N] ratio and increases the refractive index.

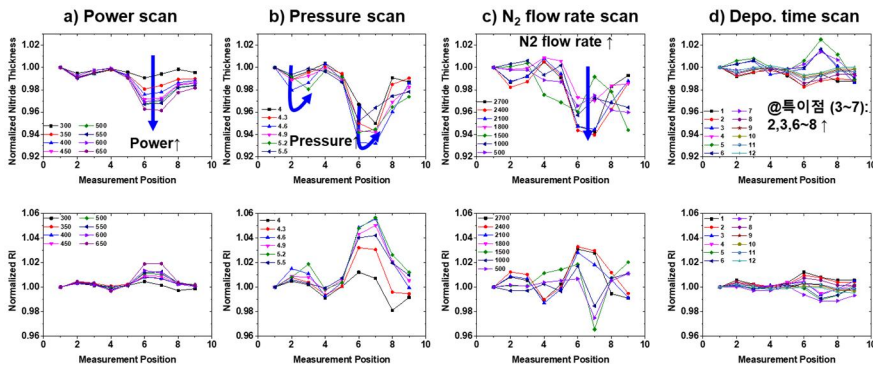


**Figure 5-4.** Uniformity of wafer state variables depending on process condition. a) power scan. b) pressure scan. c)  $N_2$  flow rate scan. d) deposition time scan. Values in figure are normalized by that of wafer center position.

The developed PI-VM will predict mean nitride THK, mean  $n$ , uniformity of THK, and uniformity of  $n$  will be developed. The uniformity is defined the ratio of measurement position 7 over measurement position 1. In PI-VM, recipe variables, such as pressure and power, and monitored line-intensities are used as the input variables of VM. The list of monitored line-intensities are summarized in Table 5-1.

**Table 5-1.** Monitored line-intensities to develop PI-VM for single-layer nitride PECVD.

<b>Step</b>	<b>Monitored line-intensities</b>
Deposition	$H_a(656nm)/N_2(406nm)$ , $SiN(412nm)/N_2(406nm)$ , and $SiH(413nm)/N_2(406nm)$ , $N_2(399nm)/N_2(406nm) \propto n_e$ , $N_2^+(391nm)/N_2(406nm) \propto T_e$
Cleaning	$CO(519nm)/N_2(406nm)$ , $H(656nm)/N_2(406nm)$ , $O(844nm)/N_2(406nm)$ , $PI_{wall}(N_2(380.4nm)/N_2(357.6nm))$

A relatively simple linear model was used for regression, because the major purpose of this study is the proposal of a novel methodology to obtain PI variables. As mentioned in Chapter 2, PLSR was chosen as the regression model, because it is more robust for noise and correlation between variables than PCR [23]. The total of 3 PLS components was selected with the following rule of thumb; at least 10 records are required to obtain a PLS component. Here, Five-fold cross-validation was used when regression was conducted. It creates a five-fold partition of data. Then modeling and validation are performed five times. For each modeling and validation, only four-folds are used as training sets and one different fold is used for validation set.

Among process state variables, power, pressure,  $SiN(412nm)/N_2(406nm)$ ,  $SiH(413nm)/N_2(406nm)$ ,  $N_2^+(391nm)/N_2(406nm)$ , and  $PI_{wall}$  are selected as input variables for development of PI-VM based on exhaustive search. Note that  $SiN(412nm)$  and  $SiH(413nm)$

are partially correlated with each other since low resolution of spectrometer and superposition of sub-bands;  $H_{\alpha}(656\text{nm})/N_2(406\text{nm})$  at deposition step is neglected due to large correlation with  $N_2^+(391\text{nm})/N_2(406\text{nm})$ ;  $CO(519\text{nm})/N_2(406\text{nm})$ ,  $H(656\text{nm})/N_2(406\text{nm})$ ,  $O(844\text{nm})/N_2(406\text{nm})$  at cleaning step are neglected due to small correlation with wafer state variables; and  $N_2(399\text{nm})/N_2(406\text{nm})$  is neglected due to large correlation with power and  $PI_{\text{Wall}}$ .

Figure 5-5 shows prediction result using PI-VM. Black rectangles and red circles represent measured and predicted property of nitride film, respectively. The predicted value explains well the actual value. The evaluated performance of VM (Table 5-2) shows that PI-VM for single-layer nitride PECVD is trustworthy because  $R^2$  and  $Q^2$  are bigger than 0.5. It will discuss the meaning of PI variables on the flux of reactive species in nitride PECVD by using VIP of PI-VM.

**Table 5-2.** Performance evaluation of PI-VM for single-layer nitride PECVD.

<b>Wafer state variable</b>	<b><math>R^2</math></b>	<b><math>Q^2</math></b>	<b>MAPE (%)</b>
Mean THK	0.93	0.81	2.3
Mean $n$	0.98	0.95	1.9
Uniformity of THK	0.94	0.86	0.5
Uniformity of $n$	0.91	0.81	0.4

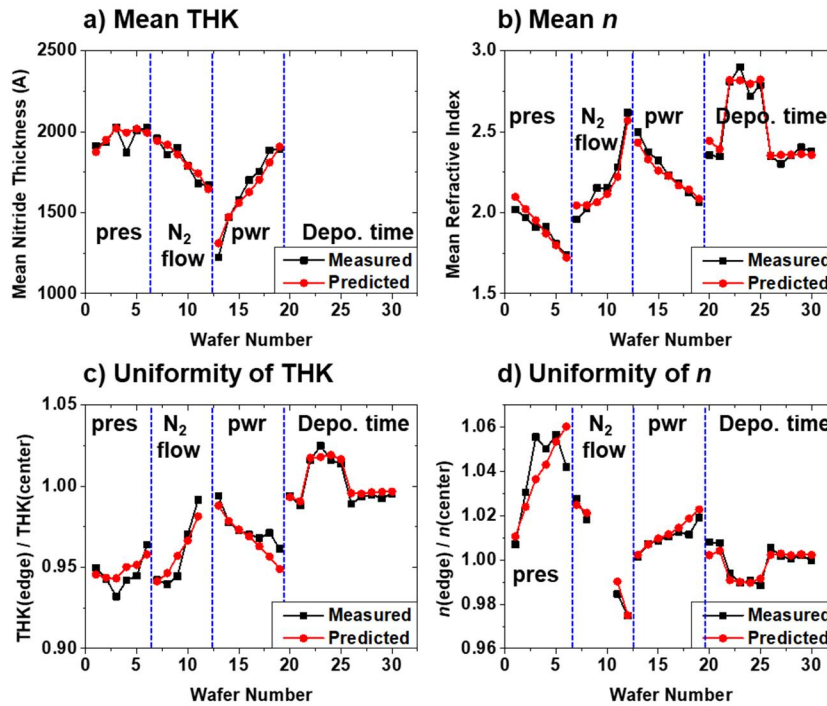


**Figure 5-5.** Prediction result of PI-VM for single-layer PECVD. Black rectangles and red circles represent measured and predicted property of nitride film, respectively. a) Mean thickness. b) Mean refractive index. c) Uniformity of thickness. d) Uniformity of refractive index. The vertical dash lines are inserted to distinguish condition of recipe scan.

The meaning of PI variables on reactive species on wafer are investigated by using VIP of PI-VM with considering sign of each variable on wafer state variable. Here, the positive sign of variable indicates a positive correlation with specific wafer state variable. For visibility, this dissertation defines ‘contribution’ of variable  $k$  as:

$$\text{contribution}(k) = (\text{sign}) \times \frac{\text{VIP}(k)}{\sum_k \text{VIP}(k)} \times 100 (\%). \quad (5.2)$$

The threshold energy of NH<sub>3</sub> dissociation and SiH<sub>4</sub> is 5.6 eV and 8.75 eV, respectively [70-71]. SiN(412nm)/N<sub>2</sub>(406nm) and SiH(413nm)/N<sub>2</sub>(406nm) ratio represent the degree of NH<sub>3</sub> dissociation and SiH<sub>4</sub> dissociation, respectively. It implies that SiH(413nm)/N<sub>2</sub>(406nm) is changed more sensitively depending on electron temperature than SiN(412nm)/N<sub>2</sub>(406nm) because threshold energy of SiH<sub>4</sub> dissociation is larger than that of NH<sub>3</sub> dissociation.

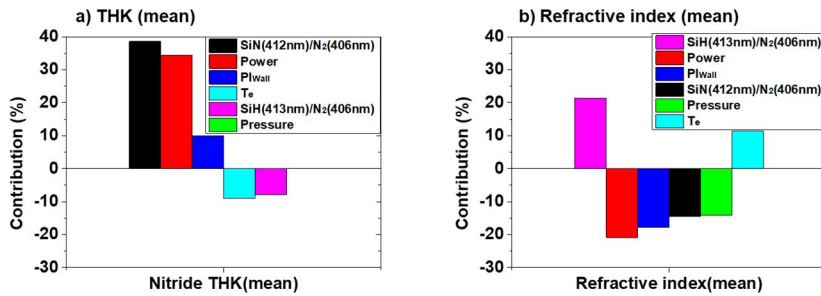
Figure 5-6 shows the contribution of variables on mean wafer states: mean nitride thickness and mean refractive index. Figure 5-6(a) shows that mean nitride thickness has positive correlation with electron density (power) and the dissociation of NH<sub>3</sub> whereas electron temperature and the dissociation of SiH<sub>4</sub> does not have a large effect. It is originated from that the growth of silicon nitride film is limited by nitridation reaction meaning that the dissociation of NH<sub>3</sub> increase is major contributor for thickness. Also, small influence of electron temperature and the dissociation of SiH<sub>4</sub> on mean thickness confirms that increase of SiH<sub>x</sub>/NH<sub>y</sub> ratio in plasma is hardly influence on the nitride reaction on a-Si:H layer.

Figure 5-6(b) shows that increase of the dissociation of SiH<sub>4</sub> directly increases mean refractive index ( $n_{\text{a-Si}}=3.3 > n_{\text{Si}_3\text{N}_4}=1.9$ ). The electron temperature also increases the refractive index because it enhances the dissociation of SiH<sub>4</sub> rather than that of NH<sub>3</sub>. In the similar way, increase of pressure decreases the refractive index by decreasing the electron temperature. While the increase of electron density (power) and the dissociation of NH<sub>3</sub> decreases the refractive index by decreasing Si/N ratio in the nitride film.

From Figure 5-6, meaning of PI<sub>Volume</sub> on reactive species on wafer can be interpreted as follows. The electron density enhances the electron-impact collision reactions with low threshold energy, such as dissociation of NH<sub>3</sub> in nitride PECVD, delivering nitrogen containing precursors to the a-Si:H layer. Consequently, the electron density increases the

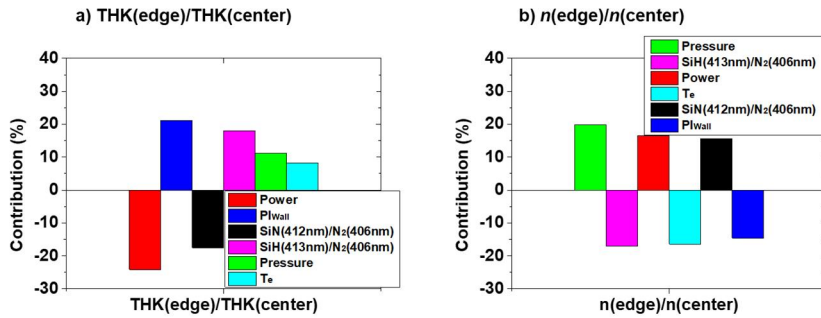
nitride thickness while decreases refractive index. The electron temperature enhances the electron-impact collision reactions with high threshold energy, like dissociation of  $\text{SiH}_4$  in nitride PECVD. It results in increasing  $\text{SiH}_4/\text{NH}_3$  dissociation ratio in nitride PECVD.

On the other hand,  $\text{PI}_{\text{Wall}}$  has relatively small contribution than  $\text{PI}_{\text{Volume}}$  on thickness. However, it offers the positive influence on mean nitride thickness as the dissociation of  $\text{NH}_3$  (Figure 5-6(a)) and it is one of high contributor to determine the refractive index (Figure 5-6(b)). Consequently,  $\text{PI}_{\text{Wall}}$  decreases Si/N ratio in nitride film meaning that it increases N containing radicals in plasma.



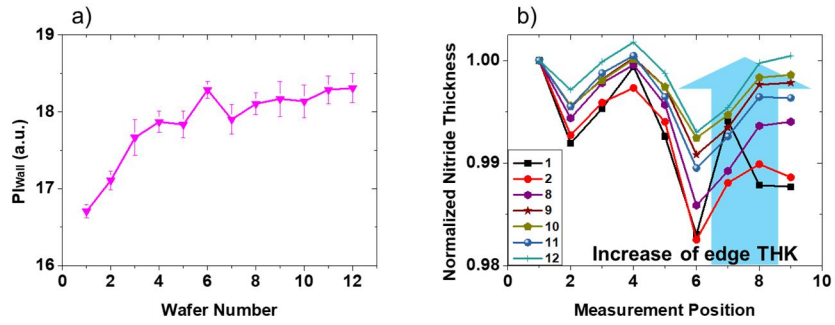
**Figure 5-6.** Contribution of variables on wafer state. a) Contribution on mean nitride thickness. b) Contribution on mean refractive index

Figure 5-7 shows the contribution of variables on the uniformity of wafer states. The influence of recipe variables and radical densities on the uniformity are hard to analyze. Instead, the meaning of  $\text{PI}_{\text{Wall}}$  can be estimated from the result that it increases edge thickness and decreases edge refractive index.



**Figure 5-7.** Contribution of variables on the uniformity of wafer state. a) Contribution on the uniformity of nitride thickness. b) Contribution on the uniformity of refractive index.

Figure 5-8 clearly shows the influence of reactor-wall condition on the nitride film. As  $PI_{Wall}$  increases (Figure 5-8(a)), the edge thickness increases at the fixed recipe (Figure 5-8(b)). From Figure 5-6 to Figure 5-8, it is confirmed that  $PI_{Wall}$  increases the density of N containing radicals by changing deactivation of reactive species at reactor-wall. Especially, the influence of reactor-wall on reactive radicals are stronger near the reactor-wall (wafer-edge) than wafer-center region. As shown in Figure 4-12, the deposited film-thickness on reactor-wall increases as with deposition time (or step) and the deposited film has very small N content and constant O/Si ratio. It implies that desorption from reactor wall is a minor cause of variation in plasma volume. It is expected that the drift of nitride plasma is caused by the variation of recombination probability of N containing radicals due to temperature increase of reactor-wall [72] or thick oxide film that reduces N recombination sites on the surface [62].



**Figure 5-8.** Influence of reactor wall condition on the uniformity of nitride film. a) W2W variation of  $PI_{Wall}$  depending on wafer number. b) W2W variation of uniformity depending on wafer number. The plotted data was originated from the deposition time scan recipe.

## 5.2 PI-VM for the nitride film in multi-layer PECVD

Figure 5-9 shows the measured thicknesses of nitride film depending on L2L and W2W variations. The trend of film thickness increases as the layer number increases. In W2W process, the drift of film thickness increases as equipment time increases, leading to the requirement of a stronger cleaning process to maintain the reactor-wall condition consistently.

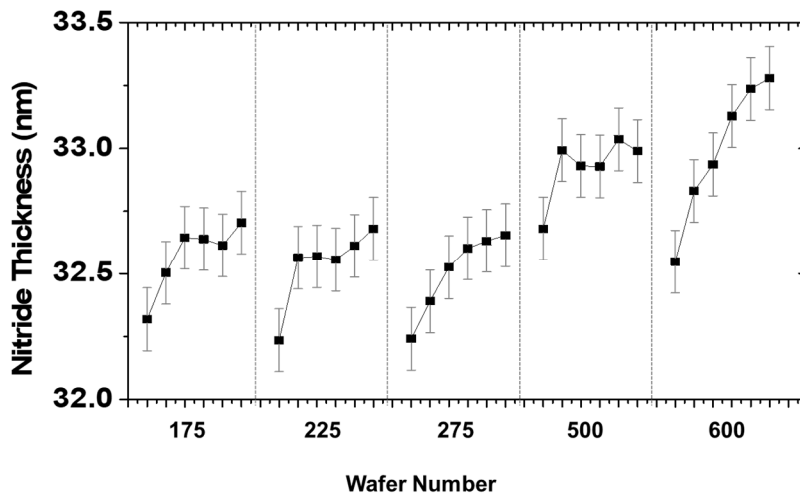


**Figure 5-9.** L2L and W2W variation of nitride film thickness (wafer state variable). The vertical dash lines are inserted to distinguish each wafer. The error bar in the measured thickness originates from the pixel resolution of STEM image.

Figure 5-10 shows L2L and W2W variation of process state variables. The figures from b) to h) were sorted in descending order of correlation with measured film thickness. It indicates that  $PI_{Wall}$  has most strong correlation with measured film thickness. Figure 5-10(b) shows that  $PI_{Wall}$  illustrates well the L2L and W2W trend of measured film thickness. In L2L scale, film

thickness increases as film deposition on reactor-wall increases. Also, the variation of reactor-wall condition induces variation of VAT (vacuum valve) position resulting in the increase of reactive species in plasma. It finally induces the variation of plasma density and temperature.

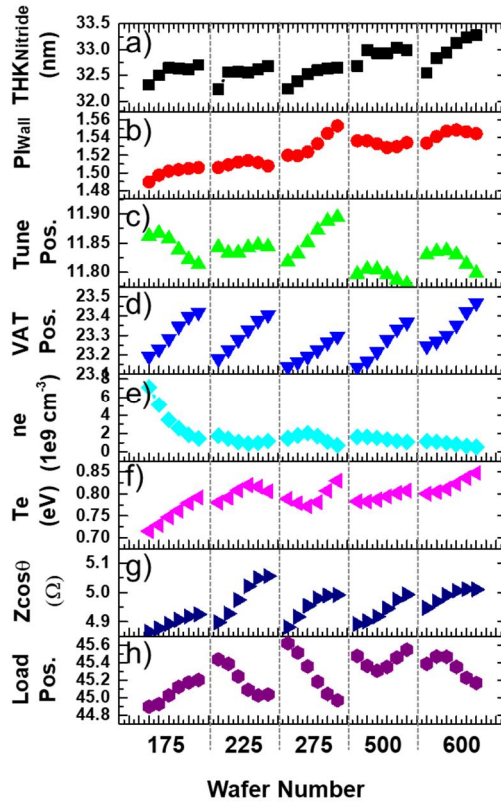


**Figure 5-10.** L2L and W2W variation of wafer and process state variables. a) measured film thickness. b)  $PI_{wall}$ . c) Tune position of matcher. d) VAT position. e) Electron density. f) Electron temperature. g) Resistance measured at matcher. h) Load position of matcher. The figures were sorted in descending order of correlation with measured film thickness.

As mentioned previously, PLSR with five-fold cross-validation was chosen as the regression model and the total of 3 PLS components was selected with the following rule of

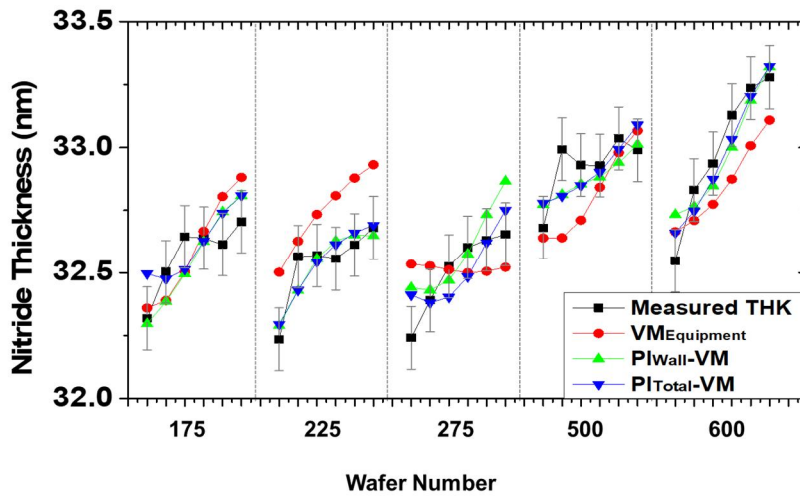
thumb; at least 10 records are required per PLS component. Table 5-3 is a summary of the variable sets for the regression model. Note that ‘Equipment’ variable set was determined using the conventional exhaustive search among equipment variables in Table 3-1. The name was set to ‘Equipment’ because the components of this variable set are mostly equipment variables (except for  $Z\cos\theta$ ). Three VM models (Table 5-3) was constructed to evaluate the performance improvement of VM depending on the inclusion of PI variables. These models were named  $VM_{\text{Equipment}}$ ,  $PI_{\text{Wall}}\text{-VM}$ , and  $PI_{\text{Total}}\text{-VM}$ , depending on the adopted variable sets of ‘Equipment’, ‘Equipment +  $PI_{\text{Wall}}$ ’, and ‘Equipment +  $PI_{\text{Wall}}$  +  $PI_{\text{Volume}}$ ’, respectively. Note that all VM input variables are applied to VM after normalization.

**Table 5-3.** Determined variables set depending on the inclusion on PI variables.  $Z$  means magnitude of impedance measured at RF matcher.

<b>Variable set</b>	<b>Used variables</b>	<b>VM model</b>
Equipment	Load/tune position of matcher, operating pressure, throttle-valve position, $Z\cos\theta$ from PIM sensor	$VM_{\text{Equipment}}$
Equipment+ $PI_{\text{Wall}}$	All variables in Equipment set + $PI_{\text{Wall}}$	$PI_{\text{Wall}}\text{-VM}$
Equipment+ $PI_{\text{Wall}}$ + $PI_{\text{Volume}}$	All variables in Equipment set + $PI_{\text{Wall}}$ + $PI_{\text{Volume}}$	$PI_{\text{Total}}\text{-VM}$

Figure 5-11 shows the measured and predicted thicknesses of nitride film depending on L2L and W2W variations. The black rectangles indicate the measured nitride thickness by using STEM. The red circles, green upper triangles, and blue lower triangles represent the predicted thicknesses from three models,  $VM_{\text{Equipment}}$ ,  $PI_{\text{Wall}}\text{-VM}$ , and  $PI_{\text{Total}}\text{-VM}$ , respectively. Compared with measured thickness,  $VM_{\text{Equipment}}$  predicts L2L trend for the wafer 3 in the opposite direction. It not only overestimates the thickness for the wafers 1 and 2, but also underestimates the thickness for the wafers 4 and 5. It implies that the accuracy of prediction

become worsened for the long-term process because  $VM_{\text{Equipment}}$  cannot recognize the drift of reactor-wall condition. It is deduced from the general characteristics of process state variables in plasma-assisted process. The raw process state variables are hard to take meaningful information about reactive species in plasma because they are coupled with the mixture of system and plasma. For example, VAT position mainly indicates the pressure, but the collisionality in plasma is more delicate due to coupling of pressure with plasma. Therefore, the raw process state variables do not sensitively monitor the drift caused by reactor-wall condition. It results in the degradation of prediction reliability. On the other hand, the results of PI-VM are well agree with the measured thickness.



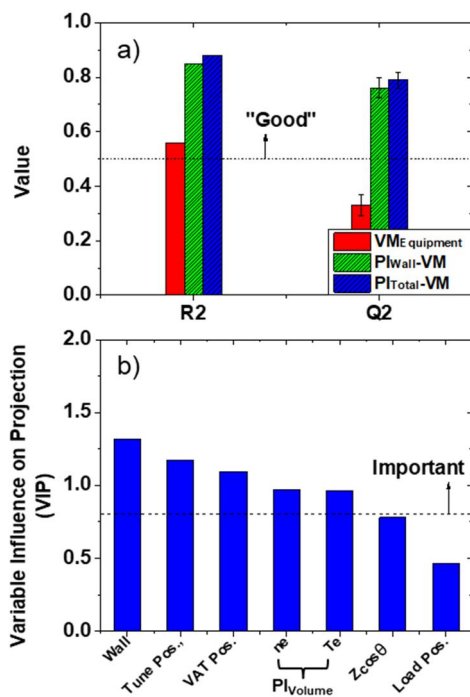
**Figure 5-11.** Comparison of three VM models. Black rectangles show the measured thickness. Red circles, green upper triangles, and blue lower triangles represent  $VM_{\text{Equipment}}$ ,  $PI_{\text{Wall-VM}}$ , and  $PI_{\text{Total-VM}}$ , respectively. The vertical dash lines are inserted to distinguish each wafer. The error bar in the measured thickness originates from the pixel resolution of STEM image.

Figure 5-12(a) shows  $R^2$  and  $Q^2$  of three VM models as red bar, a green dense-hatch pattern, and a blue sparse-hatch pattern, representing the values of  $VM_{\text{Equipment}}$ ,  $PI_{\text{VM}_{\text{Wall}}}$ , and

PI-VM<sub>Total</sub>, respectively.  $R^2$ ,  $Q^2$  and MAPE are summarized in Table 5-4. Note that p-value of all  $R^2$  and  $Q^2$  is less than  $10^{-6}$  which value is much less than significance level, indicated by 0.05.  $R^2$ ,  $Q^2$ , and MAPE of VM<sub>Equipment</sub> are 0.56, 0.33, and 0.59% respectively, and the difference between  $R^2$  and  $Q^2$  is 0.23. By including PI<sub>Wall</sub>,  $R^2$ ,  $Q^2$ , and MAPE are not only improved to 0.85, 0.76 and 0.34%, but also, the difference between  $R^2$  and  $Q^2$  is reduced to 0.09. The inclusion of PI<sub>Volume</sub> additionally improved  $R^2$ ,  $Q^2$ , and MAPE to 0.88, 0.79 and 0.33%, respectively, without affecting the difference between  $R^2$  and  $Q^2$ . VIP of PI-VM<sub>Total</sub> in Figure 5-12(b) shows that PI<sub>Wall</sub> is the highest contributing variable, and that PI<sub>Volume</sub> is also an important variable to improve the prediction reliability. From Figure 5-12, it can be confirmed that the influence of PI<sub>Volume</sub> is relatively smaller than that of PI<sub>Wall</sub> in the case of intermediate-pressure plasma with fixed RF power and pressure, as in this study. It implies that the variation of reactive species diffused from the reactor-wall plays a dominant role in the drift of PECVD.

**Table 5-4.** Performance evaluation of PI-VM for multi-layer nitride PECVD.

<b>VM model</b>	<b><math>R^2</math></b>	<b><math>Q^2</math></b>	<b>MAPE (%)</b>
VM <sub>Equipment</sub>	0.56	0.33	0.59
PI <sub>Wall</sub> -VM	0.85	0.76	0.34
PI <sub>Total</sub> -VM	0.88	0.79	0.33



**Figure 5-12.** Performance evaluation of VM models. (a) Comparison of  $R^2$  and  $Q^2$  depending on the inclusion of PI variables on VM. A value larger than 0.5 represents a sound VM model. (b) Variable influence on projection (VIP) of PI-VM<sub>Total</sub>. A VIP larger than 0.8 means that the variable is important.

In Figure 5-13,  $R^2$  values of VM models were compared depending on the region of layers to check the meaning of PI<sub>Volume</sub> on VM model. In the first-half layers (layers 2–4), the inclusion of PI<sub>Wall</sub> is the only PI that increased  $R^2$ , while the inclusion of PI<sub>Volume</sub> in the latter half of layers (layers 5–7) increased  $R^2$  by 0.05. It deduces that PI<sub>Volume</sub> further enhanced VM performance and the variation of plasma state become important with increasing layers. Note that it is very difficult to perform monitoring using the external power or the pressure gauge after the reactor-wall condition has been changed. It is expected that the influence of PI<sub>Volume</sub> further enhanced as required number of nitride/oxide pairs increases.

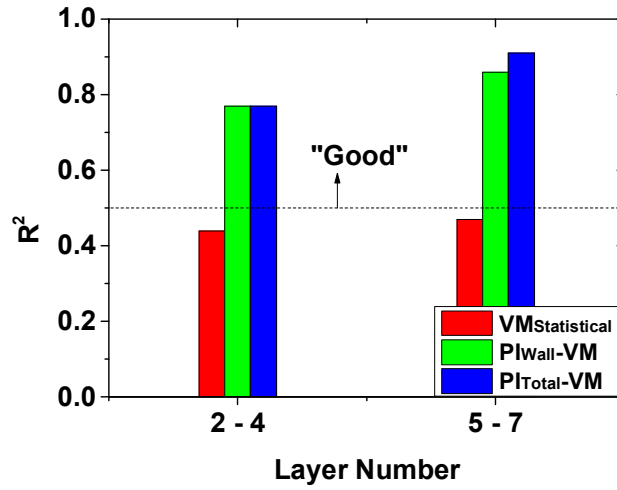


**Figure 5-13.**  $R^2$  of VM Models depending on the region of layers. Left figure:  $R^2$  of the first half-layers; right figure:  $R^2$  of the remaining half-layers.

## Chapter 6 . Conclusion

Through the consideration on the factors affecting the flux of reactive species on wafer of plasma-assisted processes, plasma-information (PI) variables are developed with evaluating light transmittance at contaminated window. It is confirmed that PI-VM improves the prediction reliability at high values even for drifting process. This method promotes the application of plasma spectroscopy as sensor technology, improvement of data mining techniques, and in-depth of process plasma which can classify the fault in process and find the control knobs for process maintain

PI for the film buildup on reactor-wall (named  $PI_{\text{wall}}$ ) is determined by using the light transmittance at the contaminated window through line-intensity ratios from same upper energy level. PI for the electron-impact collisions in plasma (named  $PI_{\text{volume}}$ ) is determined by analyzing line-intensity ratios from different upper energy levels based on collisional-radiative model (CRM), after correcting the transmittance variation depending on wavelength caused from the window contamination.

The developed PI-VM is adopted to predict the property of nitride film made by PECVD. PI-VM well predicts the variation of wafer state. The 'contribution' of variables on PI-VM shows that the electron density enhances low threshold reactions, such as dissociation of  $\text{NH}_3$ , while the electron temperature enhances high threshold reactions, such as dissociation of  $\text{SiH}_4$ . It also shows that the film buildup on reactor-wall increases the formation of N containing species, especially near the reactor-wall, through reducing deactivation rate at the reactor-wall. In multi-layer PECVD used in mass production-line,  $PI_{\text{wall}}$  is the highest contributing variable,

implying that the wafer state variables of nitride/oxide multi-layer PECVD are mainly deviated due to the drift of reaction rate at reactor-wall. The high influence of  $PI_{\text{Volume}}$  in latter region of layers implies that the electron-impact collisions additionally changed N containing radicals in latter layers. In the trend increasing the number of layers to maximize the density of chips, variable influence on projection (VIP) analysis of PI-VM suggests the phenomena of plasma to be managed: electron-impact collisions in plasma volume and film deposition on reactor wall.

PI-VM develops a framework that applies the plasma spectroscopy, one of the basic plasma diagnostics technology to the plasma-assisted process in the semiconductor and display manufacturing. Specifically, PI-VM not only provides a monitoring method for reactor-wall condition but also enables to interpret the cause of process drift individually. These advantages can provide the fundamentals to develop advanced process control (APC), fault detection and classification (FDC) for plasma-assisted processes.

# Appendix A: Theoretical background of plasma spectroscopy

The atomic/molecular physics for plasma spectroscopy can be found in the many standard books [26,27,31]. Here, this dissertation briefly describes the atomic/molecular energy levels and excitation equilibria in plasma based on [30,32,33,73,75].

## A.1 Atomic and molecular energy levels

The atomic or molecular structure is strongly related to emission or absorption spectra. For light atom, the electronic energy level has its spectroscopic notation (or term symbol) called LS notation:

$$nl^w \ ^{2S+1}L_{L+S}, \quad (\text{A.1})$$

where  $n$  is the principal quantum number;  $l$  is the angular momentum quantum number;  $w$  is the number of electrons in the shell;  $S$  is the spin;  $2S+1$  is the multiplicity; and  $J=L+S$  is the total angular momentum quantum number. Levels with different  $L$  values are known as S, P, D, and F levels for  $L=0, 1, 2,$  and  $3,$  respectively. The degeneracy for a level with a given  $L$  and  $S$  is  $(2L+1)(2S+1)$ . Part of the degeneracy is usually removed by weak magnetic interactions between the spin and orbital motions, giving rise to additional small splitting of the degenerate energy levels, the so-called fine structure. The remaining degeneracy for each level with a given  $L, S,$  and  $J$  is  $2J+1$ .

Then the electric dipole radiation (optically allowed transitions) is permitted between two states only if the selection rules are satisfied:

$$\begin{aligned}\Delta L &= \pm 1 \\ \Delta J &= 0, \pm 1 \quad (J=0 \rightarrow J=0 \text{ forbidden})\end{aligned}\tag{A.2}$$

For light atoms, the additional rules must be satisfied:

$$\begin{aligned}\Delta L &= 0, \pm 1 \quad (L=0 \rightarrow L=0 \text{ forbidden}) \\ \Delta S &= 0\end{aligned}\tag{A.3}$$

As an example of light atom, Figure A- 1 shows the energy level diagram for helium which have two electrons. The levels are separated into two multiplet systems: a singlet and a triplet system. Following Pauli's principle, the spin of two electrons in the ground state is arranged anti-parallel resulting in the  $1s\ 1^1S$  state. The fine structure is indicated only for the  $2^3P$  state. Certain excited states cannot satisfy the selection rules for electric dipole radiation. While other radiative transitions may occur, such as electric quadrupole or magnetic dipole radiation, or radiationless transitions may occur, to states of nearly equal energy that subsequently do radiate, these mechanisms are generally weak, leading to transition times that can be long compared to the collision times. The energy levels where electric dipole radiation is forbidden are called metastable, and the excited atoms are called metastable states ( $2^3S$  and  $2^1S$ ). Also, transitions which are linked directly to the ground state are called resonant transitions and excited atoms are called resonance states. The corresponding transition probability is high; hence the radiation is very intense. But radiation tapping also high for these levels leading to considerable densities. Therefore, metastable and resonance states are often present at considerable densities in low-pressure/low-temperature plasma leading to considerable step-



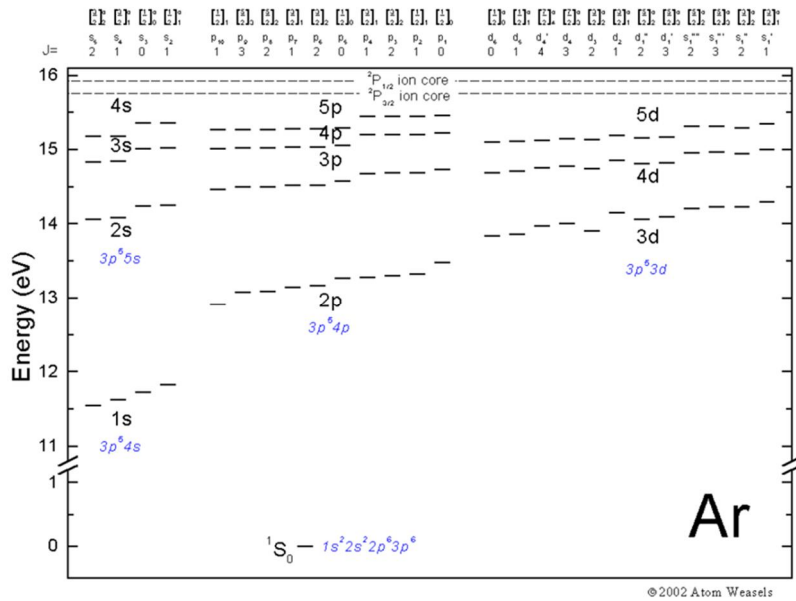


**Figure A-2.** Energy level diagram of argon atom [74].

Paschen's notation is strictly empirical: the lowest energy  $np^5(n+1)s$  level is called the  $1s_5$ , the second highest  $1s_4$ , etc. The next configuration  $np^5(n+1)p$  consists of ten levels, nine of which are mixed  $LS$ -levels of the same  $J$  starting from  $^1S_0$ ,  $^3S_1$ ,  $^1P_1$ ,  $^3P_0$ ,  $^3P_1$ ,  $^3P_2$ ,  $^1D_2$ ,  $^3D_1$ ,  $^3D_2$  and one pure  $LS$ -level, the  $^3D_3$ . In Paschen's notation these are designated (from highest to lowest energy) the  $2p_1$  to  $2p_{10}$  levels.

Racah's notation is based upon labelling  $p^5nl$  excited levels by means of the  $jK$  coupling scheme. The  $p^5$  core has a core orbital angular momentum ( $l_c = 1$ ) which first couples together with the core spin ( $s_c = 1/2$ ) to form the core angular momentum, either  $j_c = 1/2$  or  $3/2$ . The next step is to couple  $j_c$  with the 'outer' electron's orbital ( $l_o = l$ ) angular momentum to form the intermediate vector  $K$ . Finally,  $K$  is coupled to the 'outer' electron's spin ( $s_o$ ) angular

momentum to form the total angular momentum  $J$ . Thus, a level with  $j_c = 1/2$  would be designated as  $n^l[K]_J$ , and a level with  $j_c = 3/2$  would be designated as  $n^l[K]_J$ .

For molecular, the energy levels of molecules are more complicated for two reasons. First, molecules have additional vibrational and rotational degrees of freedom due to the motions of their nuclei, with corresponding quantized energies  $E_v$  and  $E_J$ . Note that  $J$  for molecular structure means rotational quantum number, not the total angular momentum quantum number for atomic structure. Second, the energy  $E_e$  of each electronic state depends on the instantaneous configuration of the nuclei.

For a diatomic molecule,  $E_e$  depends on a single coordinate  $R$ , the spacing between the two nuclei. Since the nuclear motions are slow compared to the electronic motions, the electronic state can be determined for any fixed spacing (Born-Oppenheimer approximation). Therefore, each quantized electronic level can be represented as a frozen set of nuclear positions (Figure A-3). For a molecule to be stable, the ground (minimum energy) electronic state must have a minimum at some value  $\overline{R}_1$  corresponding to the mean intermolecular separation (curve 1). In this case, energy must be supplied to separate the atoms ( $R \rightarrow \infty$ ). An excited electronic state can either have a minimum ( $\overline{R}_2$  for curve 2) or not (curve 3). Note that  $\overline{R}_1$  and  $\overline{R}_2$  do not generally coincide. As for atoms, excited states may be short lived (unstable to electric dipole radiation) or may be metastable. Various electronic levels may tend to the same energy in the unbound ( $R \rightarrow \infty$ ) limit.

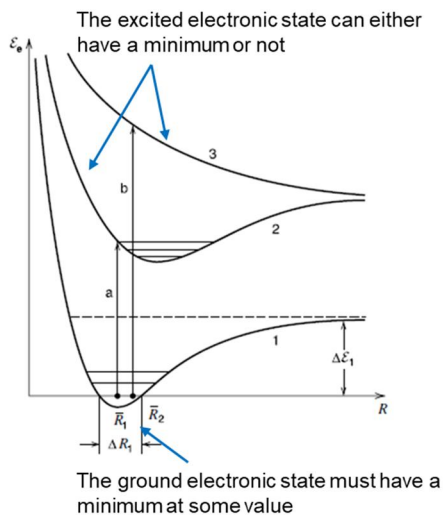


**Figure A- 3.** Potential energy curves for diatomic molecule [33].

Again, the two electrons cause a splitting into a singlet and a triplet system. In molecules the electronic energy levels are usually abbreviated by upper- and lower-case letters, where  $X$  is the ground state. Due to the additional degrees of freedom, each electronic state has vibrational levels (quantum number  $v$ ) and each vibrational level has rotational levels (quantum number  $J$ ) which appear with decreasing energy distances. For diatomic molecule, the electronic energy level has its term symbol like the case of atom:

$$^{2S+1}\Lambda_{g/u}^{+/-} \tag{A.4}$$

where  $\Lambda$  is the total orbital angular momentum along the internuclear axis, with the symbols S, P, D, and F corresponding to  $\Lambda = 0, \pm 1, \pm 2,$  and  $\pm 3$  in analogy with atomic nomenclature. All but the  $\Sigma$  states are doubly degenerate in  $\Lambda$ . For  $\Sigma$  states, + and - superscripts are often used to denote whether the wave function is symmetric or antisymmetric with respect to reflection at any plane through the internuclear axis. The total electron spin angular momentum  $S$  is also

specified, with the multiplicity  $2S+1$  written as a prefixed superscript, as for atomic states. Finally, for homonuclear molecules ( $H_2$ ,  $N_2$ ,  $O_2$ , etc.) the subscripts g or u are written to denote whether the wave function is symmetric or antisymmetric with respect to interchange of the nuclei.

The transition intensity or radiation intensity is proportional to the square of the transition dipole moment. This transition dipole moment is the product of electronic transition dipole moment and Franck-Condon factor (square of the vibrational overlap integral).

The electronic transition dipole moment offers selection rules (for Hund's case (a) and (b)):

$$\begin{aligned} \Delta\Lambda &= 0, \pm 1 \\ \Delta S &= 0 \end{aligned} \quad (A.5)$$

For transitions between  $\Sigma$  states, the allowed transitions are  $\Sigma^+ \rightarrow \Sigma^+$  and  $\Sigma^- \rightarrow \Sigma^-$ . For homonuclear molecules, the allowed transitions are g $\rightarrow$ u and u $\rightarrow$ g. That is, Homonuclear diatomic molecules do not have a pure vibrational or rotational spectrum. Also, there is no selection rules for vibrational transition while the rotational lines must follow  $\Delta J=0, \pm 1$ , forming so-called *P*-, *Q*- and *R*-branches. Therefore, radiation in the visible spectral range appear in the spectrum as ro-vibrational bands. The intensity of each band is determined by Franck-Condon factor meaning that the transition probability has high value if maxima of two wave functions at similar separation  $R$ .

## A.2 Excitation equilibria in plasmas

As briefly mentioned in Chapter 4, the dominant population and de-population reaction for  $p$  state are a function of the excitation equilibrium of corresponding energy state. At first, thermodynamic equilibrium (TE) or complete thermodynamic equilibrium (CTE) is defined as the collection of ‘proper balances’ all-in equilibrium. Here, ‘balance’ means ‘two+scale’ and ‘equilibrium’ means ‘equal+weight (or rate)’. There are four ‘proper balance’ types relevant to atomic state distribution function (ASDF) as described in Table A- 1.

**Table A- 1.** The four types of proper balances.  $At_p$ ,  $E$ ,  $E_{hp}$ ,  $|E_p|$  refer to an atom in energy level  $p$ , the kinetic energy of the particle, the increase of internal energy, and ionization potential, respectively.

Balance	Formula	Description
Maxwell balance	$X + Y \leftrightarrow X + Y$ $E_X + E_Y = (E_X + \Delta E) + (E_Y - \Delta E)$	Kinetic energy exchange ( $\Delta E$ ) and conservation
Boltzmann balance	$X + At_l + (E_{hl}) \leftrightarrow X + At_u$	Balance between excitation and de-excitation
Saha balance	$X + At_p + ( E_p ) \leftrightarrow X + At_l + e$	Balance between ionization and recombination
Planck balance	$At_u \leftrightarrow At_l + h\nu$ $At_u + h\nu \leftrightarrow At_l + 2h\nu$	Balance between absorption, spontaneous and stimulated emission

However, TE is an imaginary state in real world. In many plasmas, the departure from TE exists and it can be described by the presence of one or more ‘improper balances’ consisting of forward and backward processes not being each other’s inverses. If radiation escapes from a plasma this affects Planck’s distribution law. But this leak of energy can disturb other balances as well. However, if the loss of radiative energy is small compared to the energy exchange

between material particles, it is possible that the balances of Boltzmann, Saha and Maxwell are in equilibrium and that atoms, ions and electrons have the same temperature. The limitation in space which causes the escape of radiation is accompanied by the presence of gradients so that the balances are locally in equilibrium. Slow variations in the plasma conditions are also permitted the balances. At this stage of equilibrium, known as local thermal equilibrium (LTE), thermodynamic properties must be specified locally and instantaneously. Characteristics of LTE is that the matter and radiation are decoupled from each other. Apart from that, also spatial and temporal decoupling are allowed in LTE. In LTE, all particles, such as neutrals, excited species, ions, and electrons, have same temperature.

Further departure from TE can be realized if different particles are subjected to different forces. Many laboratory plasmas are created by electromagnetic heating of the electrons while the atoms are cooled by wall collisions. Since the rate of energy transfer from the electrons to the heavy particles is not very effective due to the small mass ratio, the Maxwellization within the same particles is much faster than that between different particles. This situation is often referred to as a two-temperature plasma and the ASDF is the result of competition between Boltzmann and Saha balances regulated by electrons.

Further TE-departures can be expected if the gradients become larger and the transport of particles significant. The transport of charged particles out of an active plasma region will disturb the local Saha balance of ground state atoms because the electrons and ions leaving the system cannot contribute to recombination. The plasma region is ionizing. However, this does not necessarily mean that all the Saha balances are out of equilibrium. In the upper part of the atomic energy scheme, where levels are close to the continuum, the ionization rates are effective. This situation is characterized by electron-ruled-partial-local-Saha-equilibrium pLSE. The energy gaps between the lower lying levels and the continuum are usually too large to retain the equilibrium of Saha balances at the bottom of the system. In this way the

atomic energy scheme is decoupled in an upper and a lower part; a bottom and a top in pLS<sub>e</sub>E.

The population of lower excited levels is not according to Saha and Boltzmann but still determined by balances of elementary processes only, which balance each other in an improper way within a time much smaller than that associated with the growth or decay of the plasma. There are four possible improper balances: corona balance (CB) and excitation saturation balance (ESB) for ionizing plasma; capture radiative cascade (CRC) and de-excitation saturation balance (DSB) for recombining plasma (Figure A- 4).

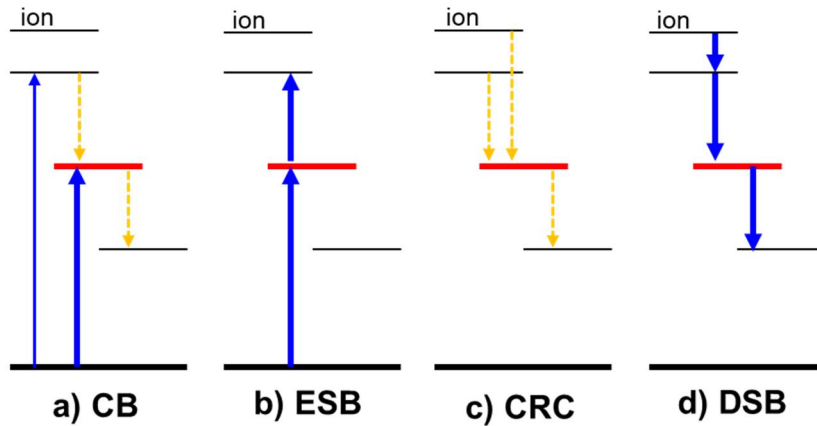


**Figure A- 4.** Schematic diagram of improper balances. a) CB. b) ESB. c) CRC. d) DSB. Blue and yellow dashed arrows represent electron-impact collisions and radiative decay reactions, respectively.

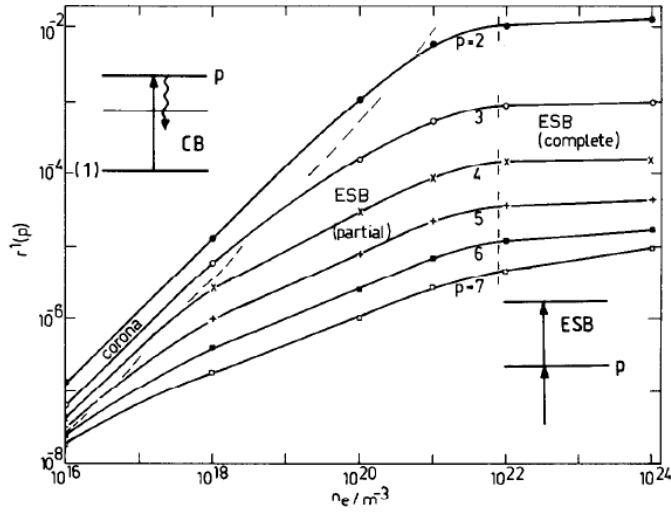
In CB, collisional destructions are very weak compared to radiative ones. Consequently, the excited levels are destroyed by radiative decay and generated by electron-impact excitations. As the collisional process become stronger, the excited levels are both generated and destroyed by electron-impact collisions in ESB. In CRC, the excited levels are destroyed by radiative decay, and generated by capture/cascade reaction. Also, in DSB, the excited levels are both generated and destroyed by electron-impact collisions.

Figure A- 5 shows the relative population density of excited level  $p$  depending on the

electron density. At low electron density, the population density is linearly proportional to the electron density. This is the characteristics of CB as expressed follows:

$$n_e n_g K_p = n_p A_p \Rightarrow n_p = n_e n_g K_p / A_p, \quad (\text{A.6})$$

where  $K_p$  and  $A_p$  represent total collisional destruction and decay coefficient, respectively.



**Figure A-5.** Variation of for an optically thin hydrogen plasma as a function of electron density [76]. Here,  $T_e=2.75$  eV and  $r_l(p)$  is relative density of  $p$  level to density of  $p$  level at Boltzmann distribution. The state of plasma changes from CB to ESB as the electron density increases.

On the other hand, at high electron density, the population density is independent to the electron density. This is the characteristics of ESB as expressed follows:

$$n_e n_g K_{ex}^{lower} = n_e n_p K_{ex}^{upper} \Rightarrow n_p = n_g K_{ex}^{lower} / K_{ex}^{upper}, \quad (\text{A.7})$$

where  $K_{ex}^{lower}$  and  $K_{ex}^{upper}$  represent electron-impact generation from lower state and destruction to upper state, respectively. Note that the collisional-radiative model should be used in the electron density region between CB and ESB ( $10^{18} - 10^{22} \text{ m}^{-3}$  in Figure A-5).

The important boundary is the boundary between CE and ESB regime. The boundary can

be determined where the electron-impact destruction equals the radiative decay:

$$n_{eC}K(p_{cr}) = A(p_{cr}), \quad (\text{A.8})$$

where  $n_{eC}$  is critical electron density for CB and ESB boundary,  $p_{cr}$  is the critical effective quantum number as described in Chapter 4. Then the approximated boundary is given as equation (4.2) with assumption of  $T_e^* = T_e / Z^2 = 1\text{eV}$ . From equation (4.2), one can determine the characteristics of specific energy level  $p^*$  by comparing it with  $p_{cr}$ . If  $p^*$  is much smaller than  $p_{cr}$ , the energy state belongs to CB. Reversely, if  $p^*$  is much larger than  $p_{cr}$ , the energy state belongs to ESB. The remaining region belongs to CR region (or partial ESB region in Figure A- 5).

## Appendix B: Diagnostics of $PI_{\text{Volume}}$ in non-Maxwellian plasmas

As mentioned in Chapter 4, the nature of plasma spectroscopy is optimization problem to minimize the error between measured and expected line-intensities. To efficiently converge the optimization problem, reasonable determination of EEDF, emission model, and reaction data is required after intensity calibration. In this chapter, the method to determine non-Maxwellian EEDFs will be presented based on the analytical EEDF functions and Ar CRM.

### B.1 Analytical EEDF functions

Electron energy distribution function (EEDF),  $f(E)$ , is defined as the portion of electrons inside the energy space  $[E, E+dE]$ . EEDF has mean energy  $\bar{E}$ :

$$\bar{E} = \int_0^{\infty} E f(E) dE , \quad (\text{A.9})$$

where  $f(E)$  is normalized such that

$$\int_0^{\infty} f(E) dE = 1 . \quad (\text{A.10})$$

In thermodynamic equilibrium, EEDF has Maxwellian distribution,  $f_{\text{Max}}(E)$ :

$$f_{\text{Max}}(E) = \frac{2}{\sqrt{\pi}} T_e^{-3/2} \sqrt{E} \exp\left(-\frac{E}{T_e}\right), \quad (\text{A.11})$$

where the electron temperature,  $T_e$  satisfies  $\bar{E}=3/2T_e$ .

However, the concept of temperature is only valid for a Maxwellian distribution, and low-pressure/low-temperature plasmas typically are strongly non-equilibrium. In non-equilibrium plasmas, the extension of temperature to non-Maxwellian distributions is by defining an ‘effective’ temperature,  $T_{\text{eff}}$ , whereby  $\bar{E}=3/2T_{\text{eff}}$ .

The generalized Druvesteyn distribution is an analytic function using two parameters, ( $x, T_x$ ) that represents EEDF with depleted high-energy tail [77]:

$$f_x(E) = c_1' T_x^{-3/2} \sqrt{E} \exp\left[-c_2' \left(\frac{E}{T_x}\right)^x\right], \quad (\text{A.12})$$

where

$$c_1' = x \left(\frac{2}{3}\right)^{3/2} \frac{[\Gamma(5/2x)]^{3/2}}{[\Gamma(3/2x)]^{5/2}}, \quad (\text{A.13})$$

$$c_2' = \left(\frac{2}{3}\right)^x \left[\frac{\Gamma(5/2x)}{\Gamma(3/2x)}\right]^x, \quad (\text{A.14})$$

with  $\Gamma(y)$  is a Gamma function. Here,  $T_x$  is equal to effective electron temperature. The distribution is equivalent to Maxwellian when  $x = 1$  and Druvesteyn when  $x = 2$ .

Figure B- 1 shows sample electron energy probability function (EEDF) depending on the variation of  $x$ -parameter. Here, EEDF, defined as  $f_p(E)=E^{-1/2}f(E)$ , has a linear dependence on electron energy for Maxwellian distribution in log scale ( $x=1$ ). The generalized Druvesteyn distribution describes depletion of high-energy tail as  $x$ -parameter increases.

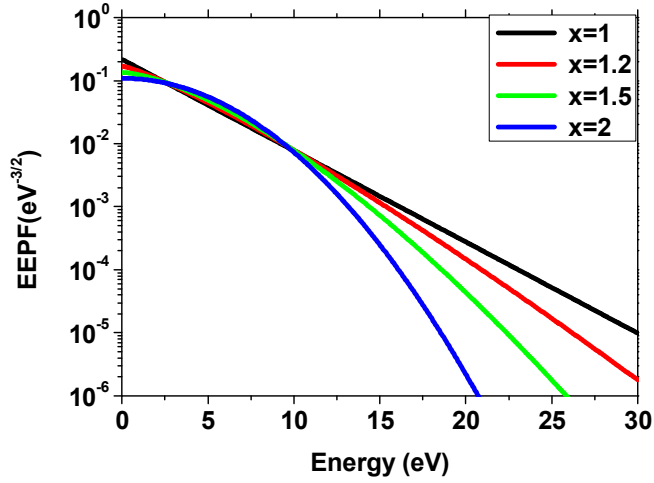


**Figure B-1.** Sample EEDFs depending on the  $x$  parameter. Here, effective electron temperature is fixed at 3 eV.

For tail-enhanced EEDF, authors often use analytic function with high-energy electrons added to Maxwellian distribution:

$$f(E) = \left(1 - \frac{\alpha}{100}\right) f_{\text{Max}}(E) + \frac{\alpha}{100} f_{\text{tail}}(E), \quad (\text{A.15})$$

where  $\alpha$  describes the fraction of high-energy electron group (%) and  $f_{\text{tail}}(E)$  is EEDF function of high-energy electrons. For bi-Maxwellian EEDF,  $f_{\text{tail}}(E)$  is defined as another Maxwellian distribution with different electron temperature from that of bulk electron. Also, shifted-Maxwellian EEDF can be used to describe beam-like electrons in very-high-frequency (VHF) CCP [22,78]:

$$f_{\text{shifted}}(E) = \left(1 - \frac{\tau}{T_{RF}}\right) f_{\text{Max}}(E) + \frac{\tau}{T_{RF}} \frac{1}{\sqrt{\pi}} T_e^{-1/2} \sqrt{E} \exp\left(-\frac{E + E_0}{T_e}\right) \frac{\exp(2\sqrt{EE_0}/T_e) - 1}{2\sqrt{EE_0}}, \quad (\text{A.16})$$

where the time factor,  $\tau/T_{RF}$ , is the fraction of time for which the beam-like electrons exist at the measurement position of OES,  $E_0$  is the mean energy of beam-like electrons. Then the analytical EEDF for CCP can be described as:

$$f(E) = \left(1 - \frac{\alpha}{100} \frac{\tau}{T_{RF}}\right) f_{\text{Max}}(E) + \frac{\alpha}{100} \frac{\tau}{T_{RF}} \frac{1}{\sqrt{\pi}} T_e^{-1/2} \sqrt{E} \exp\left(-\frac{E + E_0}{T_e}\right) \frac{\exp(2\sqrt{EE_0}/T_e) - 1}{2\sqrt{EE_0}} \quad (\text{A.17})$$

Figure B- 2 shows a sample curve of analytic EEDF for VHF-CCP. The curve describes the tail-enhanced EEDF with increase of  $\alpha$  and  $E_0$ .

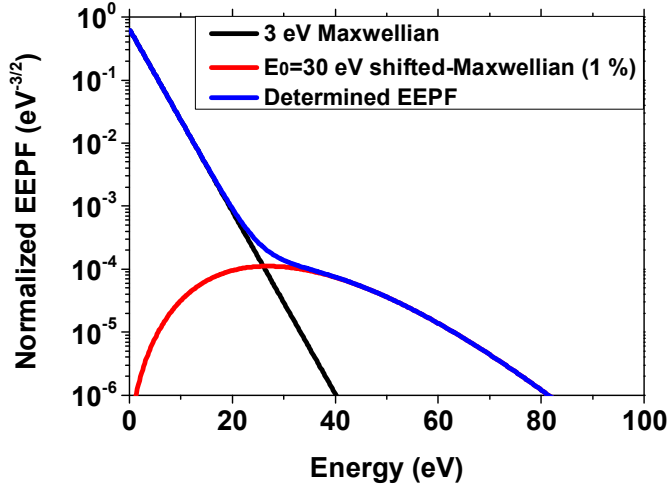


**Figure B- 2.** Sample EEPFs depending on the  $\alpha$  parameter. Here, effective electron temperature is fixed at 3 eV. Example of the analytical EEPF model for narrow-gap VHF-CCP. Black dashed and red dotted lines represent the Maxwellian and shifted Maxwellian EEPFs, respectively.  $T_e = 3$  eV,  $E_0 = 30$  eV, and  $\alpha = 1\%$  were assumed.

## B.2 Argon CRM

At first, this dissertation selected emission intensities as described in Table B-1.  $p_{cr}$  is  $\sim 6.8$  when  $n_e$  is  $3.0 \times 10^{10} \text{ cm}^{-3}$ , which is the maximum  $n_e$  in our study. Therefore, the destruction mechanism of selected intensities or energy states can be described as CB-like emissions.

**Table B-1.** The argon lines used to determine the densities of 1s states and EEDF. All information is based on NIST atomic spectroscopy databases [80].  $E_{th}$  is the excitation threshold energy from the ground state,  $A_{pk}$  is the radiative decay coefficient, and  $p^*$  is the effective quantum number.

Target	$\lambda$ (nm)	Transition	$E_{th}$ (eV)	$A_{pk}$ ( $10^6 \text{ s}^{-1}$ )	$p^*$	Note
1s densities	696.5	$2p_2 \rightarrow 1s_5$	13.33	6.39	2.37	
	706.7	$2p_3 \rightarrow 1s_5$	13.30	2.00	2.35	
	727.3	$2p_2 \rightarrow 1s_4$	13.33	1.83	2.37	
	738.4	$2p_3 \rightarrow 1s_4$	13.30	8.47	2.35	
	794.8	$2p_4 \rightarrow 1s_3$	13.28	18.6	2.34	
	826.5	$2p_2 \rightarrow 1s_2$	13.33	15.3	2.37	
	852.1	$2p_4 \rightarrow 1s_2$	13.28	13.9	2.34	
EEDF	425.9	$3p_1 \rightarrow 1s_2$	14.74	3.98	3.65	Dipole- forbidden
	603.2	$5d_4' \rightarrow 2p_9$	15.13	2.46	4.65	Spin- forbidden
	750.4	$2p_1 \rightarrow 1s_2$	13.48	44.5	2.44	Dipole-

However, in low-pressure/low-temperature plasma for semiconductor manufacturing, it is difficult to describe the population of excited state based on pure CB due to the existence of a substantial number of metastable and resonance states. For argon discharge, substantial number of  $1s$  states ( $1s_2$ - $1s_5$ ) exists ( $n_{1s}/n_{\text{ground}}=10^{-6}$ - $10^{-4}$ ). They affect the population and depopulation through electron-impact excitation and radiation trapping. Therefore, the line-intensities measured at low-pressure/low-temperature plasma should be interpreted based on modified CB model as shown in Figure B- 3.

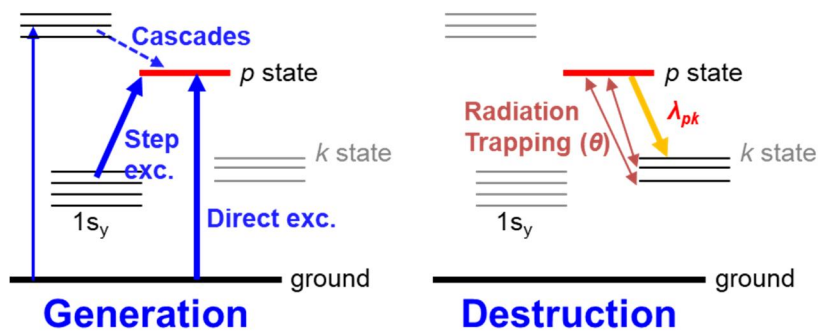


**Figure B- 3.** Description of the generation and destruction in modified CB model.

The model assumes that the excitation from the ground state and long-lived  $1s$  states with consideration of the cascade effect from high-lying states are the dominant population processes for the  $p$  state. Also, the destruction is governed mainly the radiative decay with consideration of the radiation trapping:

$$n_e \sum_i n_i Q_{ip}^{app} = n_p \sum_{l < p} \theta_{pl} A_{pl} , \quad (\text{A.18})$$

where the subscript  $i$  describes the ground state and  $1s$  states, and  $l$  is all optically allowed states lower than the  $p$  state.  $Q_{ip}^{app}$  is the apparent excitation rate coefficient ( $\text{cm}^3 \text{s}^{-1}$ ). Here, ‘apparent’ represent the sum of the direct and cascade process as defined in [79].

Then, the line-intensity from  $p$  state to  $k$  state can be expressed as:

$$I_{pk} = \frac{\theta_{pk} A_{pk}}{\sum_{l < p} \theta_{pl} A_{pl}} n_e \sum_i n_i Q_{ip}^{app} = \Gamma_{pk}^{eff} n_e \sum_i n_i Q_{ip}^{app} , \quad (\text{A.19})$$

where  $\Gamma_{pk}^{eff}$  is the effective branching fraction of the  $p \rightarrow k$  transition [79]. The escape factor is a function of the reabsorption coefficient and the characteristic scale length of the source, such as plasma depth or radius. The expression for escape factor can be selected considering the characteristics of target discharge. For uniform source, Mewe’s approximation can be used [81]:

$$\theta_{pk} \approx \frac{2 - \exp(-10^{-3} k_{ij} \rho)}{1 + k_{ij} \rho} , \quad (\text{A.20})$$

where  $k_{ij}$  is the reabsorption coefficient and  $\rho$  is the characteristic scale length of the source. The plasma source which has small depth, such as CCP, mono-directional escape factor can be used [82]:

$$\theta_{pk}^M = \frac{1}{\sqrt{\pi} k_{ij} \rho} \int_{-\infty}^{\infty} [1 - \exp\{-k_{ij} \rho \exp(-v^2)\}] dv . \quad (\text{A.21})$$

Also, for a Doppler broadened line, the reabsorption coefficient is expressed as:

$$k_{ij} = \frac{\lambda_{ij}^3}{8\pi^{3/2}} \frac{g_i}{g_j} n_j A_{ij} \sqrt{\frac{M}{2RT_g}}, \quad (\text{A.22})$$

where  $g_i$  and  $g_j$  are the statistical weights of upper ( $i$ ) and lower ( $j$ ) states,  $n_j$  is the density of the lower state,  $T_g$  is the gas temperature,  $M$  is the atomic mass, and  $R$  is the gas constant. The line-intensity ratio from the same upper state can be described as:

$$\frac{I_{pk}}{I_{pr}} = \frac{\theta_{pk} A_{pk}}{\theta_{pr} A_{pr}}, \quad (\text{A.23})$$

Therefore, the line-intensity ratio from the same upper state is a function of the escape factor meaning that the ratio is function of the density of the lower states, when the length of the line-of-sight is fixed. In this work,  $\rho$  is fixed to the diameter of the chamber wall. From the emission lines in Table B- 1, four line-intensity ratios are used to determine the density of the  $1s$  states:  $I_{696.5\text{nm}}/I_{727.3\text{nm}}$ ,  $I_{706.7\text{nm}}/I_{738.4\text{nm}}$ ,  $I_{696.5\text{nm}}/I_{826.5\text{nm}}$ , and  $I_{852.1\text{nm}}/I_{794.8\text{nm}}$ .

Then, the parameters for EEDF are determined by using the line-intensity ratio from the different upper state described as:

$$\frac{I_{pk}}{I_{qr}} = \frac{\Gamma_{pk}^{\text{eff}} \sum_i n_i Q_{ip}^{\text{app}}}{\Gamma_{qr}^{\text{eff}} \sum_i n_i Q_{iq}^{\text{app}}}. \quad (\text{A.24})$$

The line intensity ratios used are  $I_{425.9\text{nm}}/I_{750.4\text{nm}}$  and  $I_{603.2\text{nm}}/I_{750.4\text{nm}}$ . Note that the key to the line selection is the difference of excitation threshold energy and the energy dependence of the excitation cross-section from the ground state. Figure B- 4 shows the ground excitation cross-sections of the selected lines. The excitation cross-sections of the  $3p_1$  (425.9 nm) and  $2p_1$  (750.4 nm) states are of the dipole-forbidden type, and that of the  $5d_4$  (603.2 nm) state is of the

spin-forbidden type. The excitation cross-section of the dipole-forbidden type has a relatively moderate peak width, with a peak near 20 eV. On the other hand, the excitation cross-section of the spin-forbidden type decreases rapidly with increased energy after a peak near 20 eV, since the excitation of the spin-forbidden type is based on electron-exchange interaction [79]. For tail-depleted EEDF, the cross-section near threshold energy (Figure B- 4(b)) governs the excitation rate constant, because there are few electrons in the energy region above 20 eV. For EEDFs with a highly populated tail, however, the dependence of the excitation cross-section after peak energy is also important, because their energies are larger than the threshold energy of excitation. Consequently, the difference of threshold energy is used to determine tail-depleted EEDF, and the difference of the spin- and dipole-forbidden lines is used to determine tail-enhanced EEDF.

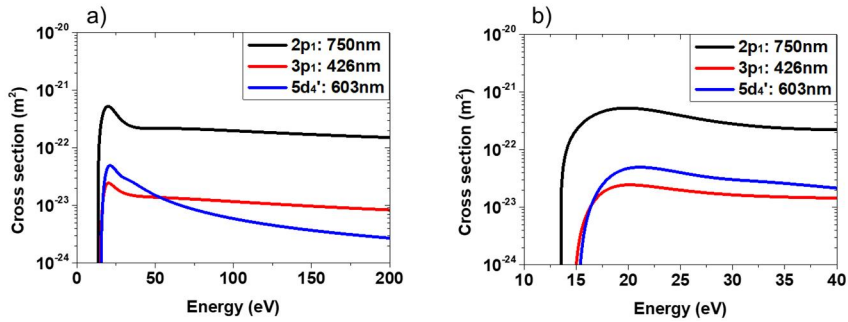


**Figure B- 4.** Electron-impact excitation cross-section from the ground state [79]. a) Full curve. b) Near threshold energy. Black solid and red dashed lines represent the excitation cross-sections of the  $2p_1$  and  $3p_1$  states, respectively. They are the dipole-forbidden type of excitation. The blue dotted line represents the excitation cross-section of the  $5d_4'$  state, which is the spin-forbidden type of excitation.

By using these properties, the parameters of analytic EEDF function, such as  $(x, T_x)$  in generalized Druvesteyn and  $(\alpha, E_0)$  of shifted-Maxwellian, are determined to minimize the difference between the measured intensity ratios and expected intensity ratios from the modified CB model. To achieve this, the absolute error (AE) was introduced to create a data map as a function of the parameters of analytic EEDF function:

$$AE = \left| 1 - \left( \frac{J_{pk}^{expected}}{J_{qr}^{expected}} \right) / \left( \frac{J_{pk}^{measured}}{J_{qr}^{measured}} \right) \right|. \quad (A.25)$$

This dissertation defined the point in data map as candidates of solution when the point satisfies  $AE < 0.01$ . Here the criterion 0.01 was chosen with consideration of the fact that the uncertainty of the measured line-intensity was about 1%. Finally, the parameters of analytic EEDF function are determined from the cross-point of the solution curves.

Table B- 2 summarizes the information of the cross-sections used in this analysis. Excitation from  $1s$  states to  $2p_1$  and  $3p_1$  states was determined by using the excitation rate coefficient and assuming the Maxwellian EEDF. It assumes that the excitation from  $1s$  states to  $2p_1$  or  $3p_1$  states is governed by the Maxwellian EEDF of bulk electrons, since the excitation threshold energy is small ( $\sim 2$  eV). Further, the excitation from  $1s$  states to the  $5d_4'$  state is assumed to be zero, since not only is there no experimental cross-section, but the excitation is also spin-forbidden with  $1s$  states.

**Table B- 2.** Reaction rate set to determine EEDF

<b>Classification</b>	<b>Formula</b>	<b>Reaction rate (<math>\text{m}^3/\text{s}</math>)</b>	<b>Uncertainty (%)</b>
Electron-impact excitation from ground state [79]	$e+\text{Ar} \rightarrow$ $e+\text{Ar} (2p_1, 3p_1, 5d_4')$	Figure B- 4	$\sim 12$
		$1s_2 \rightarrow 2p_1: 4.9 \times 10^{-8} \exp(-1.71/T_e)$	
		$1s_3 \rightarrow 2p_1: 1.3 \times 10^{-8} \exp(-1.79/T_e)$	
Electron-impact excitation from $1s$ states [83-85]	$e+\text{Ar} (1s_x) \rightarrow$ $e+\text{Ar} (2p_1, 3p_1, 5d_4')$	$1s_5 \rightarrow 2p_1: 2.5 \times 10^{-9} \exp(-1.93/T_e)$ $1s_2 \rightarrow 3p_1: 2.0 \times 10^{-9} \exp(-3/T_e)$ $1s_3 \rightarrow 3p_1: 3.1 \times 10^{-9} \exp(-3/T_e)$ $1s_4 \rightarrow 3p_1: 8.8 \times 10^{-10} \exp(-3/T_e)$ $1s_5 \rightarrow 3p_1: 2.0 \times 10^{-10} \exp(-3/T_e)$	$\sim 40 (2p_1)$ $\sim 30 (3p_1)$

### B.3 Diagnostics of tail-depleted EEDF

Low pressure ICP is used to validate the emission model for tail-depleted EEDF. In low pressure ICP, several studies reported that the EEDF is nearly Maxwellian in lower energy than the threshold energy for inelastic collision. On the other hand, the high-energy tails of low pressure ICP are often depleted due to the electron loss to the chamber wall and energy loss through inelastic collisions [86].

In plasma spectroscopy, bi-Maxwellian or generalized Druyvesteyn EEDF is often used to describe tail-depleted EEDF [86-90]. *Boffard et al.* used the emission intensities from argon  $2p$  states and generalized Druyvesteyn EEDF to describe the variation of EEDF depending on power, pressure, and the fraction of  $N_2$  mixture [86,87]. However, this method has a limit of sensitivity caused by small energy difference between argon  $2p$  states. *Donnelly* proposed using trace rare gas OES (TRG-OES), which employs the line-intensity ratios from trace rare gases to determine the time-averaged bi-Maxwellian EEDF by expanding the effective energy regime [88]. This method maximized the difference of  $E_{th}$  between emission lines by inserting five trace rare gases (He, Ne, Ar, Kr, and Xe), which occupied about 5% of the total pressure. *Zhu et al.* proposed line-intensity ratio with bi-Maxwellian EEDF and they maximized the difference of  $E_{th}$  by using argon and krypton emissions [90].

This dissertation proposes a method to determine tail-depleted EEDF by using argon emissions in Table B- 1. Unlike previous studies, the method increases the difference of  $E_{th}$  by using the emissions from high-lying states ( $3p_1, 5d_4'$ ). This method improves the sensitivity of emission model while maintaining the non-invasiveness of OES because the method does not

use the additional trace gases. The determined EEDF from OES is compared with that of Langmuir probe depending on operating pressure to validate the emission model.

Experiments were performed in an inductively coupled plasma source, as illustrated in Figure B- 5. A 500 mm single turn coil was connected to a 13.56 MHz power supply via an L-type matching network. A 500 mm diameter, 650 mm grounded cylindrical stainless-steel chamber was placed next to the quartz. In experiment, 13.56 MHz power was delivered to 500 W, and the operating pressure was varied from 2 mTorr to 50 mTorr (2, 5, 10, 20, 30, 50 mTorr).

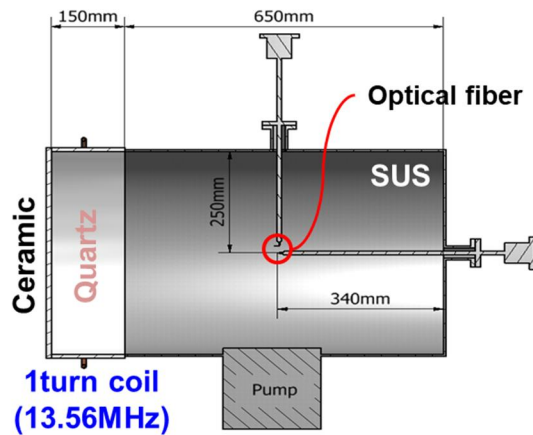


**Figure B- 5.** Schematic diagram of the ICP chamber. Two Langmuir probes are located 340 mm away from the right wall in z-axis.

The Langmuir probe was located at the radial center position 340 mm away from the right wall in z-axis. The probe tip was 0.3 mm in diameter and 10 mm in length. This geometry of the Langmuir probes satisfied the ‘small probe assumption’ in our experiment conditions [91].

To compensate for RF fluctuation, a reference tip and RF choke filters were adapted. The reference tip was 9.53 mm in diameter and 11.5 mm in length. A 470-pF capacitor connected the reference tip and the measurement tip. The impedance of each RF choke filter is shown in Figure B- 6. Since the impedance of the RF choke filter is in almost  $M\Omega$  order at the harmonics of 13.56 MHz, it satisfies Godyak's conditions of RF compensation [91].

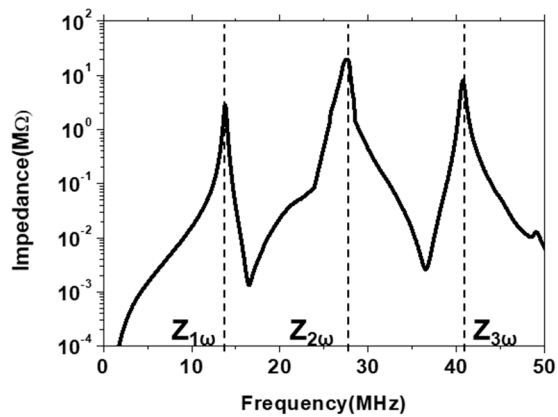


**Figure B- 6.** Impedance of the RF choke filter. Here,  $\omega$  corresponds to 13.56 MHz.

The volume-averaged emission spectra of argon plasma at 200–1100 nm wavelength were observed through an optical fiber (Korea Spectral Products, SM245), which was located at an axially central position. The spectrum was measured by setting the integration time of the spectrometer as 200 ms with  $10\times$  average for 5/10/20 mTorr, and 300 ms with  $10\times$  average for 2/30/50 mTorr. A tungsten-halogen light source (Avantes, AvaLight-DH-CAL) was used for relative intensity calibration depending on the wavelength. The mean wavelength interval was about 0.4 nm and the line width in the full width at half maximum (FWHM) was about 0.8 nm. The mean intensity for 200 nm–250 nm wavelength, where no emission was

observed in this study, was used to subtract background noise in the measured spectrum. Linear interpolation (with a 0.01 nm interval) was conducted near the peak position to estimate the line intensity. The line intensity was then estimated by using trapezoidal numerical integration of the linear interpolated data after subtraction of the residual background noise, which equaled the area of the trapezoid comprising the left and right ends in the interpolation region. If the emission line was not isolated, multi-peak Gaussian fitting was performed to estimate the line intensity.

Figure B- 7(a) compares the EEPFs measured by Langmuir probe and OES analysis. Scatters and lines represent the result of Langmuir probe and OES, respectively. Figure B- 7(b) and (c) shows the effective electron temperature and x-factor depending on operating pressure. The error bar is originated from the criterion of the solution. The overall trend shows that the determination of EEDF based on OES works properly.

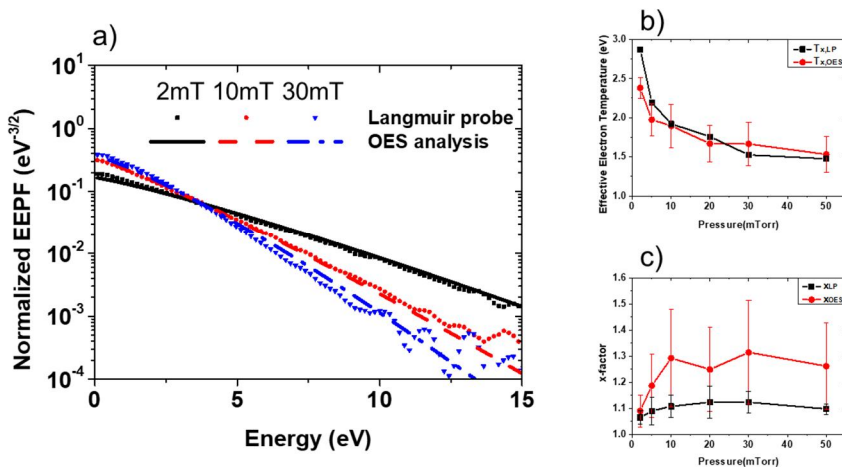


**Figure B- 7.** Variation of EEDF depending on pressure. a) Sample of EEPFs. Black rectangles, red circles, blue triangles represent measured EEPF by Langmuir probe at 2, 10, 30 mTorr, respectively. Black, red dashed, blue dash

dot lines represent measured EEPF by OES at 2, 10, 30 mTorr, respectively. b) Effective electron temperature. c) Shape factor  $x$ . Black rectangles and red circles in b) and c) represent parameters from Langmuir probe and OES, respectively.

Note that relative large error bar in Figure B- 7(b) and (c) is originated from the cross-correlation between  $x$  and  $T_x$  parameters [86]. As an example, Figure B- 8 shows two EEPFs and excitation cross sections from ground state. For tail-depleted EEDF, the population of electrons from threshold energy to 20 eV mainly governs the reaction rate. If the difference of threshold energy between two states is small, practically infinite set of  $(T_x, x)$  can satisfy same intensity ratio. That is, a generalized Druyvesteyn EEDF which have a lower value of  $x$  combined with a low  $T_x$ , and another generalized Druyvesteyn EEDF which have a higher value of  $x$  combined with a high  $T_x$ , practically same population of electrons near threshold energy inducing large error bar of determined  $T_x$  and  $x$  values, although the excitation from ground state is not the only generation path.

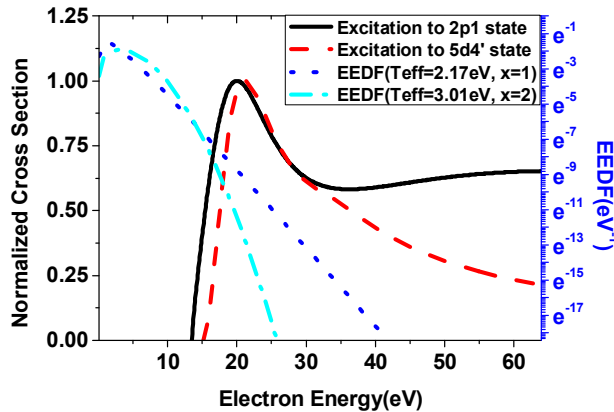


**Figure B- 8.** Cross-correlation issue of tail-depleted EEDF. Black solid and red dashed lines represent excitation cross section from ground state to  $2p_1$  and  $5d_4'$  state, respectively (left axis). Blue dotted and cyan dash-dot lines represent two EEPFs with different effective electron temperature and  $x$  parameter.

On the other hand, the determined effective electron temperatures in low pressure region (under 10 mTorr) have relatively poor accuracy than higher pressure region (Figure B- 7(b)). Figure B- 9(a) shows the fractional generation of argon  $2p_1$  state. In the pressure below 10 mTorr,  $2p_1$  state is mainly produced by electron-impact from ground state due to relatively high electron temperature (Figure B- 7(b)). Referring Figure B- 9(b) where the density ratio between  $1s_2$  and ground state equals  $10^4$ , it is confirmed that the proposed emission model can determine EEDF reasonably where electron-impact excitation from ground state and  $1s$  state has relatively similar contribution.

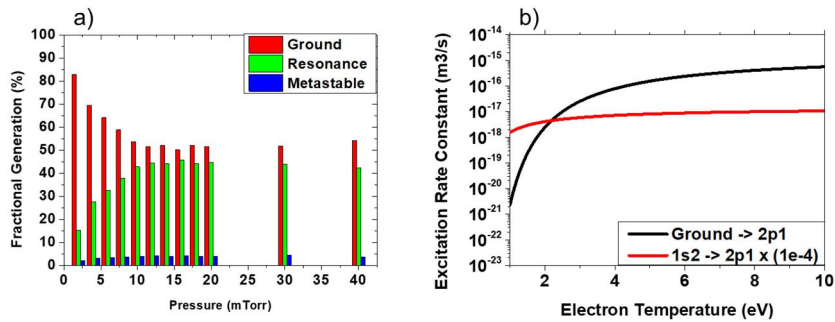


**Figure B- 9.** Variation of excitation process of argon  $2p_1$  state. a) Fractional generation of argon  $2p_1$  state. b) Variation rate coefficient depending on electron temperature.

## B.4 Diagnostics of tail-enhanced EEDF

Low pressure VHF-CCP is used to validate the emission model for tail-enhanced EEDF. In VHF-CCP, it was reported that the energetic beam-like electrons generated by stochastic heating can increase the population of the EEDF tail in low-pressure [93]. If the beam-like electrons generated in one sheath hit the opposite sheath when the sheath voltage is sufficient, the beam-like electrons can be reflected back to the bulk plasma, resulting in the increase of the population of the EEDF tail. Further, if electron bounce-resonance heating (BRH) occurs, in which the beam-like electrons bounce back and forth between two expanding sheaths, the population of the EEDF tail can increase further [93,94]. Thus, the EEDF has a special form that represents the highly populated tail of the EEDF generated by beam-like electrons [78], which has a different shape than high-temperature Maxwellian distribution.

In this section, a novel method is proposed to determine a volume- and time-averaged non-equilibrium EEDF containing a highly populated tail that mainly originated from beam-like electrons ( $>20$  eV). This method utilized a combination of Langmuir probe measurement and the line-intensity ratio method of OES. The determined EEDF is compared with the previous particle-in-cell (PIC) Monte Carlo collision (MCC) simulation result from Liu *et al* for a similar VHF-CCP [93]. Finally, the applicable range of the method is evaluated by considering the excitation kinetics and the uncertainty from diagnostic tools.

Figure B- 10 shows a schematic diagram of the narrow-gap VHF-CCP chamber. The showerhead electrode was connected to a 60 MHz or 100 MHz power supply via a matching network. The interelectrode gap size and diameter of the chamber wall were 25 mm and 590

mm, respectively. Table B- 3 shows a summary of the experimental conditions in this work and the simulation conditions in Liu’s work [93]. The performance of the proposed model was evaluated by comparing the EEDFs of this work and the previous study at 10 mTorr argon discharge, when 60 MHz power was delivered to 500 W. The trend depending on the momentum collision frequency was evaluated by varying the operating pressure from 10 to 50 mTorr, and the trend depending on the driving frequency was evaluated by comparing the 60 MHz and 100 MHz cases. Finally, the 60 MHz source power was varied from 500 to 800 W at 20 mTorr to determine the applicable electron density range of the proposed method.

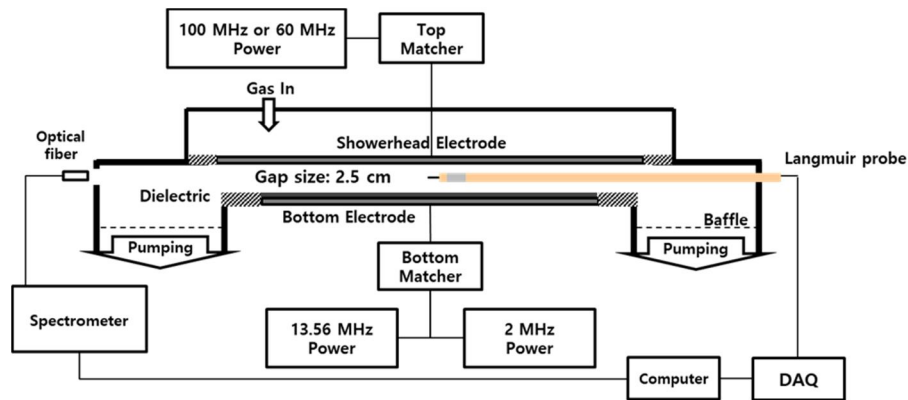


**Figure B- 10.** Schematic diagram of the narrow-gap VHF-CCP chamber. The gap size is 25 mm and the diameter of the chamber wall is 590 mm. 60 MHz or 100 MHz power is delivered to the top electrode through a matching network.

The RF-compensated cylindrical Langmuir probe shown was located at the radially and axially central position to determine the electron temperature and the density of the bulk electrons. A passive-RF compensation method was used with a reference tip and RF choke filter. The ceramic tube was used as the body of the probe holder to reduce the perturbation of

the plasma due to the probe system. The tungsten wire (0.1 mm in diameter and 2 mm in length) was used for a single probe tip. It was connected to the RF choke filter via gold-coated wire. A SUS reference tip (9.6 mm in diameter and 11.5 mm in length) was electrically connected to the gold-coated wire of the single probe tip through a 470pF capacitor. The RF choke filter was followed by coaxial in-vacuum wire (MDC, KAP5), which went to the DAQ system through a BNC cable. Here, we only compensated the fundamental harmonic of 60 MHz because it was the major component of plasma potential oscillation in our case. The impedance of the RF choke filter at 60 MHz was 40 k $\Omega$ . The data acquisition system (DAQ) measured the  $I$ - $V$  characteristics by averaging ten curves with 7 Hz sampling frequency to reduce the effect of 60 Hz noise.

**Table B- 3.** Experiment conditions.

<b>Classification</b>	<b>This dissertation</b>	<b>Liu et al. [93]</b>
Gas	Ar	Ar
Pressure (mTorr)	10-50	5, 10
Gap size (mm)	25	12.5–60
RF power (W)	500–800 (60 or 100 MHz)	50 (60 MHz)
$n_e$ ( $10^{10}$ cm $^{-3}$ )	1 - 3	1 - 2.5
$T_e$ (eV)	2.9–3.3	~3.2

The volume- and time-averaged emission spectra of argon plasma at 200–1100 nm wavelength were observed through an optical fiber (Korea Spectral Products, SM245), which was located at an axially central position. Here, we assumed that the time- and volume-averaged spectra could offer a reliable interpretation of the beam-like electrons for two reasons. (1) Generally, the mean-free path of beam-like electrons in low-pressure plasma is larger than the interelectrode gap size and its mean energy is much larger than the ambipolar potential in bulk plasma [92]. Therefore, the population of beam-like electrons is expected to be relatively uniform in the axial direction. (2) It has also been reported that the population of beam-like electrons is relatively uniform in the radial direction within the interelectrode [95].

Figure B- 11 shows an emission spectrum measured from an argon discharge (10 mTorr, 60 MHz 500 W). To reduce the perturbation originating from the Langmuir probe, the spectrum was measured after the Langmuir probe was removed from the interelectrode region. It was also measured by setting the integration time of the spectrometer as 10 ms with  $20\times$  average, and the uncertainty of the measured line-intensity was about 1%. A tungsten-halogen light source (Avantes, AvaLight-DH-CAL) was used for relative intensity calibration depending on the wavelength. The mean wavelength interval was about 0.4 nm and the line width in the full width at half maximum (FWHM) was about 0.8 nm. The mean intensity for 200 nm–250 nm wavelength, where no emission was observed in this study, was used to subtract background noise in the measured spectrum. Linear interpolation (with a 0.01 nm interval) was conducted near the peak position to estimate the line intensity. The line intensity was then estimated by using trapezoidal numerical integration of the linear interpolated data after subtraction of the residual background noise, which equaled the area of the trapezoid comprising the left and

right ends in the interpolation region. If the emission line of interest was not isolated, multi-peak Gaussian fitting was performed to estimate the line intensity.

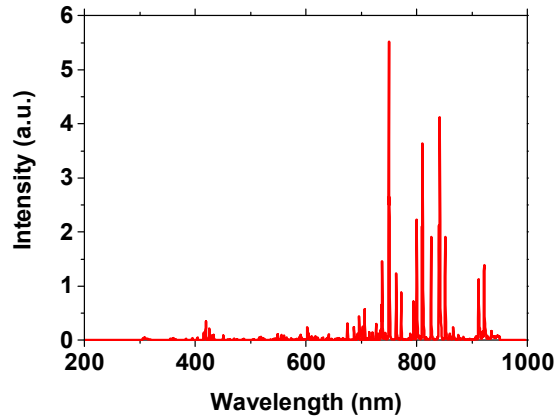


**Figure B- 11.** OES spectrum in 10 mTorr argon discharge. 60 MHz power was delivered to 500 W.

In the proposed method, the analytical EEDF model is assumed to be an EEDF with a highly populated tail that consists of a Maxwellian for the bulk electrons and a shifted Maxwellian for the beam-like electrons, with consideration of the heating and inelastic collision phenomena of narrow-gap VHF-CCP. The variables for the analytical EEDF model are the effective fraction of the beam-like electrons in the RF period, the mean energy of the beam-like electrons, and  $T_e$ . Here, the effective fraction of beam-like electrons in the RF period is defined as the product of  $\alpha$  and  $\tau/T_{RF}$ , while the mean energy of the beam-like electrons ( $E_0$ ) equals  $0.5m_e v_0^2$ .  $T_e$  is determined by using Langmuir probe. Then Ar CRM determines the effective fraction in the RF period and the mean energy of the beam-like. The difference of the spin- and dipole-forbidden lines is used to reduce the cross-correlation between the effective fraction in the RF period and the mean energy of the beam-like electrons.

The detailed procedure of the proposed method will be shown by using emissions in 10 mTorr case, before comparing the determined EEDF with the result of the simulation. In 10 mTorr, determined  $T_e$  and the densities of the  $1s$  states are as follows:  $T_e$ , 3.3 eV;  $n_{1s2}$ ,  $1.2 \times 10^{10} \text{ cm}^{-3}$ ;  $n_{1s3}$ ,  $2.1 \times 10^{10} \text{ cm}^{-3}$ ;  $n_{1s4}$ ,  $2.2 \times 10^{10} \text{ cm}^{-3}$ ; and  $n_{1s5}$ ,  $1.3 \times 10^{11} \text{ cm}^{-3}$ . Figure B-12 shows the expected line intensity ratios depending on  $\alpha$  and  $E_0$ . Figure B-12(a) shows the expected  $I_{425.9\text{nm}}/I_{750.4\text{nm}}$ , which is the line-intensity ratio of the dipole-forbidden lines, while Figure B-12(b) shows the expected  $I_{603.2\text{nm}}/I_{750.4\text{nm}}$ , which is the line-intensity ratio between the spin- and dipole-forbidden lines. The two expected line-intensity ratios show different trends, depending on  $\alpha$  and  $E_0$ , due to the different excitation type, as stated. The expected  $I_{425.9\text{nm}}/I_{750.4\text{nm}}$  saturates in the high-energy and large-fraction ranges, since the shape of the cross-sections of the  $3p_1$  and  $2p_1$  states is almost the same. On the other hand, the expected  $I_{603.2\text{nm}}/I_{750.4\text{nm}}$  drastically decreases in the high-energy range according to the mean energy of the beam-like electrons, since the excitation cross-section of the  $5d_4'$  state decreases more drastically, depending on the energy, than that of the  $2p_1$  state.

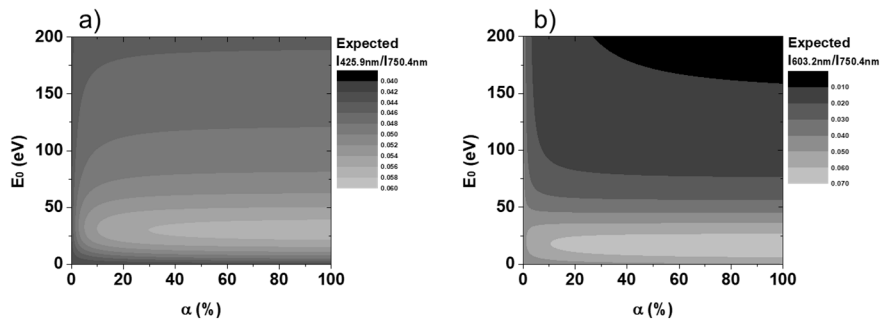


**Figure B-12.** Expected line intensity ratio depending on the fraction ( $\alpha$ ) and mean energy ( $E_0$ ) of beam-like electrons in the 10 mTorr case. (a) Expected  $I_{425.9\text{nm}}/I_{750.4\text{nm}}$  intensity ratio. (b) Expected  $I_{603.2\text{nm}}/I_{750.4\text{nm}}$  intensity ratio

Figure B- 13 shows the solution curves determined by using the criterion of AE ( $AE < 0.01$ ) in the 10 mTorr case. The solution curve of  $I_{603.2\text{nm}}/I_{750.4\text{nm}}$  is sharper than that of  $I_{425.9\text{nm}}/I_{750.4\text{nm}}$  nm, since  $I_{603.2\text{nm}}/I_{750.4\text{nm}}$  has a sharper expected intensity ratio, depending on the mean energy of the beam-like electrons, as can be deduced from Figure B- 12. Then, the fraction and mean energy of beam-like electrons can be determined from the intersection of the two solution curves. In the 10 mTorr case, the fraction is  $3.3 \pm 0.3\%$  and the mean energy is  $31.6 \pm 0.5$  eV. The uncertainty of each value originates from the criterion of the solution, 0.01.

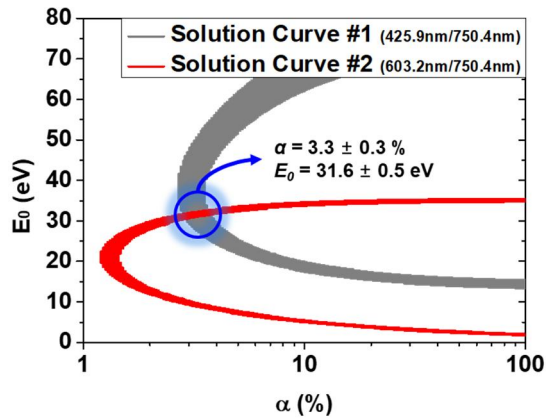


**Figure B- 13.** Solution curves for two line-intensity ratios. The fraction and mean energy of the beam-like electrons are determined from the intersection of the two solution curves.

Figure B- 14 compares the time- and volume-averaged EEPFs determined from Figure B- 13 and Liu's work [93]. Black solid and red dashed lines represent the EEPFs determined in Liu's work and this work, respectively. Table B- 4 describes the detailed conditions and EEDF. The other experimental conditions are the same as in Table B- 3.  $E_{\min}$  and  $E_{\max}$  in Figure B- 14 and Table B- 4 represent the minimum and maximum energy of the beam-like electrons,

which appear at the point where the slope changes in the EEPF. Table B- 4 confirms that the determined  $\alpha$ ,  $E_{\min}$ , and  $E_{\max}$  based on the proposed method produce a value of the same order as in Liu’s work [93], demonstrating that this method works properly.

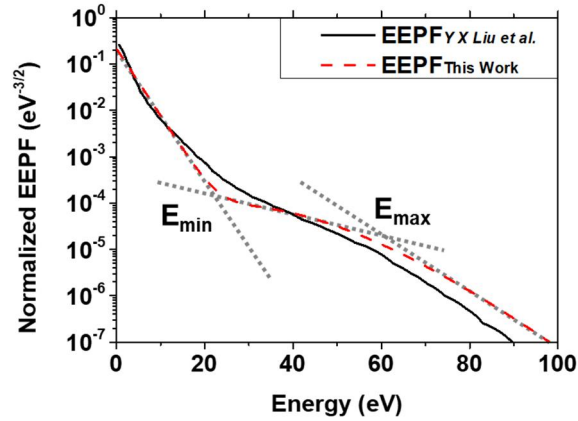


**Figure B- 14.** The determined EEPF in 10 mTorr argon discharge. Table 5 describes the detailed experiment conditions and EEPF. Black and red dashed lines represent the EEPFs determined by Liu’s work [93] and this work, respectively.

**Table B- 4.** Comparison with previous study in 10 mTorr argon discharge.

Classification	This dissertation	Liu et al. [93]
Gap size (mm)	25	22.5
60 MHz power (W)	500	50
$n_e$ ( $10^{10} \text{ cm}^{-3}$ )	1.7	2.6
$T_e$ (eV)	$3.3 \pm 0.5$	3.2
$\alpha$ (%)	$3.3 \pm 0.7$	1.3
$E_{\min} / E_{\max}$ (eV)	$\sim 23 / \sim 57$	$\sim 26 / \sim 58$

The variation of the EEPF depending on the operating pressure is shown in Figure B- 15(a), while the corresponding  $\alpha$ , and  $E_{\min}$  are shown in Figure B- 15(b). Here, we compared  $E_{\min}$ , because it means the minimum energy for an electron to join resonance, which is a function of ambipolar potential and collisionality. In Figure B- 15(b),  $\alpha$  decreases from 3% at 10 mTorr to 0.3% at 50 mTorr, and  $E_{\min}$  increases from 23 eV at 10 mTorr to 30 eV at 50 mTorr. In a previous study, it was noted that the collisional scattering of beam-like electrons and the enhancement of ambipolar potential due to increased operating pressure induced depletion of the fraction of beam-like electrons and increase of  $E_{\min}$ , respectively [93,94].

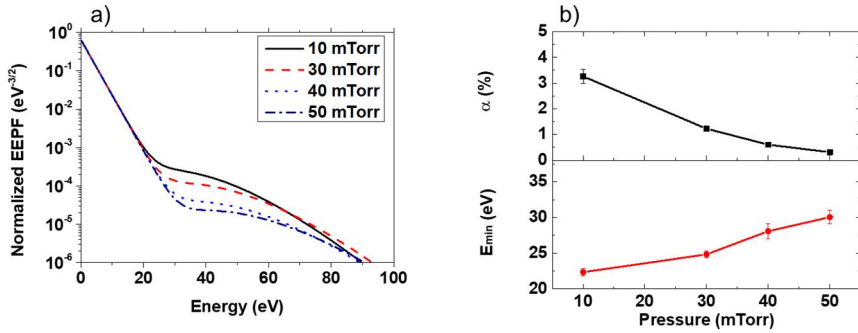


**Figure B- 15.** The variation of EEPF,  $\alpha$ , and  $E_{\min}$  depending on the operating pressure. (a) EEPFs. (b)  $\alpha$  and  $E_{\min}$ . The black rectangles and red circles in (b) represent the  $\alpha$  and  $E_{\min}$  of the beam-like electrons, respectively. The error bar originates from the criterion of the solution, 0.01.

The variation of the EEPF depending on the driving frequency is shown in Figure B- 16(a), while the corresponding  $\alpha$ , and  $E_0$  are shown in Figure B- 16(b). In Figure B- 16(b), the fraction of beam-like electrons decreases from 3% at 60 MHz to 1.6% at 100 MHz, and  $E_0$  increases from 31.6 eV at 60 MHz to 43.5 eV at 100 MHz. In a previous study, it was noted that the driving frequency has a positive correlation with  $E_0$  to satisfy the requirement that the

beam-like electrons should propagate between two sheaths of each electrode during half an RF period, or its odd times [93,94].

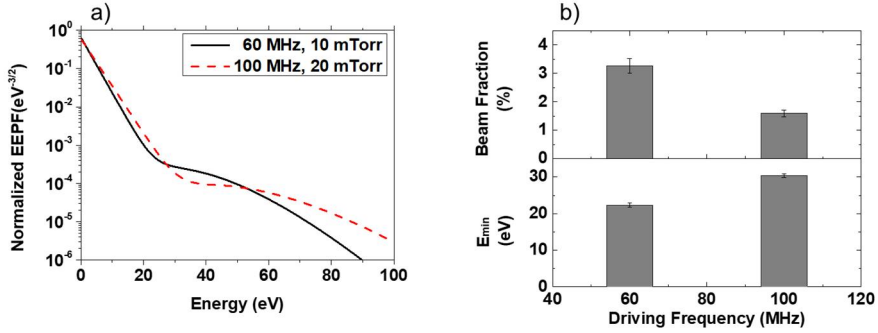


**Figure B-16.** The variation of EEPF,  $\alpha$ , and  $E_0$  depending on the driving frequency. (a) EEPFs. (b)  $\alpha$  and  $E_0$ . The error bar originates from the criterion of the solution, 0.01.

To determine the applicable plasma conditions for the proposed method, this dissertation considers the possible restrictions, such as the excitation kinetics in the emission model and the effect of uncertainty from the diagnostic systems. First, the emission model assumed that radiative decay is the dominant depopulation mechanism for each excited state. However, collisional depopulation by electron impact can be comparable to radiative decay for the  $5d_4'$  and  $3p_1$  states, because they have a long lifetime of the order of several hundred nanoseconds. Therefore,  $n_e$ , proportional to the collisional depopulation, is a key factor that limits the assumption of the modified CB model. The line intensity can be described as follows by considering the effective electron impact transition rate coefficient ( $Q_{\text{eff}}$ ):

$$I_{pk} = \frac{\theta_{pk} A_{pk}}{\sum_{l < p} \theta_{pl} A_{pl} + n_e Q_{eff}^p} n_e \sum_i n_i Q_{ip}^{app}. \quad (\text{A.26})$$

Then, the critical electron density ( $n_{eC}$ ) in Appendix A can be described as the ratio of radiative decay to the collisional depopulation by electron impact:

$$n_{eC} = \frac{\sum_{l < p} \theta_{pl} A_{pl}}{n_e Q_{eff}^p}. \quad (\text{A.27})$$

Reminding the concept of the critical electron density, the radiative decay is the dominant depopulation mechanism, such as in CB when  $n_e$  is sufficiently smaller than  $n_{eC}$ . While  $n_e$  is sufficiently larger than  $n_{eC}$ , electron-impact loss is the dominant depopulation mechanism, such as in ESB, LTE or PLTE.

The relation between  $I_{pk}^{-1}$  and  $n_e^{-1}$  can be described by inserting equation (A.27) into equation (A.26):

$$I_{pk}^{-1} = (\Gamma_{pk}^{eff} \sum_i n_i Q_{ip}^{app})^{-1} (n_e^{-1} + n_{eC}^{-1}) = (\text{slope})(n_e^{-1} + n_{eC}^{-1}). \quad (\text{A.28})$$

That is, the reciprocal of the characteristic electron density can be determined by using the y-intercept of the linear fitted graph between  $n_e^{-1}$  and  $I_{pk}^{-1}/(\text{slope})$ .

Figure B- 17 shows the linear fitted graph between  $n_e^{-1}$  and the  $I_{pk}^{-1}/(\text{slope})$  of the  $3p_1$  and  $5d_4'$  states by varying 60 MHz power from 500 to 800 W at 20 mTorr argon discharge. The black solid line and the red dashed line represent the fitted graphs of the  $3p_1$  (425.9 nm) and  $5d_4'$  (603.2 nm) states, respectively. It is confirmed that the  $n_{eC}$  of the  $3p_1$  and  $5d_4'$  states are  $5.2 \times 10^{11}$  and  $3.5 \times 10^{11} \text{ cm}^{-3}$ , respectively. Therefore, the  $5d_4'$  state, which has the highest energy level among the line intensities used, determines the applicable  $n_e$  range of the method.

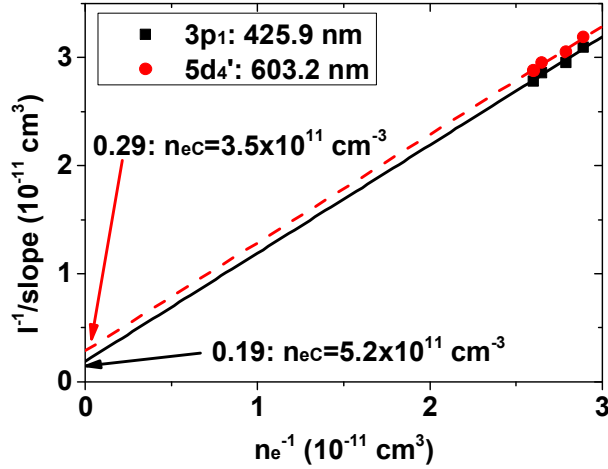


**Figure B- 17.** Dependence of  $n_e^{-1}$  and  $I_{pk}^{-1}/(\text{slope})$ . Black solid and red dashed lines represent the linear fitted graphs of the  $3p_1$  (425.9 nm) and  $5d_4^1$  (603.2 nm) states, respectively. Black rectangles and red dots represent measured values. Black solid and red dashed lines represent linear fitted lines.

The applicable  $n_e$  range of the method is defined as  $n_e/n_{eC} = 40\%$ , considering that the maximum uncertainty of the used cross-section in Table B- 2 is about 40%. That is, the method can be used when the electron density is lower than  $10^{11} \text{ cm}^{-3}$  ( $\sim 0.4 \times 3.5 \times 10^{11} \text{ cm}^{-3}$ ).

Furthermore, uncertainties from the diagnostic tools affect the accuracy of the determined EEDF. Among these, the uncertainty of the  $T_e$  measured by the Langmuir probe is most critical, because its general uncertainty is about 10%, whereas the uncertainty of the line-intensities is maintained at about 1%. In addition, the uncertainty of the measured  $T_e$  is projected to the uncertainty of the determined  $\alpha$ , since the excitation is not only a function of the beam-like electrons, but also the Maxwellian bulk electrons. Therefore, the uncertainty of measurement by Langmuir probe determines the applicable map of the method depending on

$T_e$  and the fraction of beam-like electrons. In this context, the uncertainty of the determined  $\alpha$  should be smaller than 40%, considering the maximum uncertainty of the cross-section used ( $\sim 40\%$ ). To achieve this criterion, the fraction of excitation by beam-like electrons against total excitation (defined as  $F_{\text{beam}}$ ) should be larger by at least 20% to make the uncertainty of excitation by the Maxwellian EEDF for bulk electrons induced by that of the measured  $T_e$  about 8%. In this case, the corresponding uncertainty is 40% ( $=8/20 \times 100\%$ ) of the total excitation from beam-like electrons.

Figure B- 18 shows the  $F_{\text{beam}}$  of the  $5d_4'$  state when the fraction of beam-like electrons is 1%.  $F_{\text{beam}}$  decreases as  $T_e$  increases, due to the increase of excitation by the bulk electrons. In addition, there is an optimum energy between 20–30 eV where  $F_{\text{beam}}$  is maximum, since the excitation cross-section has a maximum near 20 eV. The applicable  $T_e$  regime in Figure B- 18 is roughly under 4.5 eV, which is the maximum  $T_e$  satisfying  $F_{\text{beam}} = 20\%$ .

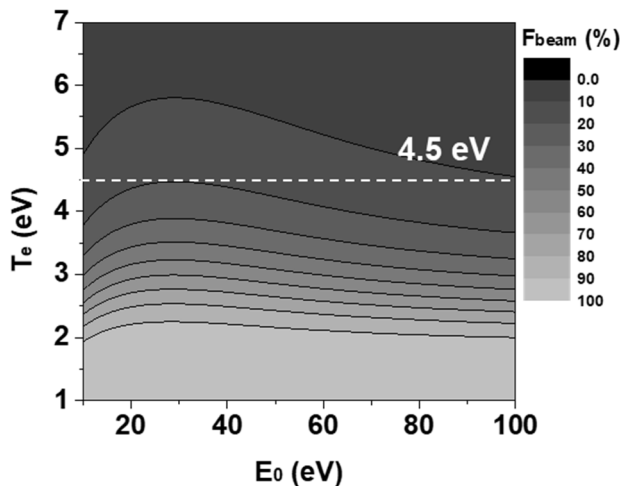


**Figure B- 18.** The fraction of beam-like electrons against the total excitation ( $F_{\text{beam}}$ ) of the  $5d_4'$  state when the fraction of beam-like electrons is 1%. The white dashed line represents the maximum  $T_e$  ( $=4.5$  eV) that satisfies  $F_{\text{beam}} =$

20%.

In the same way, the applicable regime depending on  $\alpha$  and  $T_e$  is determined as the white regime of Figure B- 19. That is, utilization of the proposed model should consider  $T_e$  carefully when the plasma has very few beam-like electrons. Conceptually, the gray range in Figure B- 19 shows the region where the line-intensity ratio method to determine Maxwellian-like or tail-depleted EEDF, described in Appendix B.3.

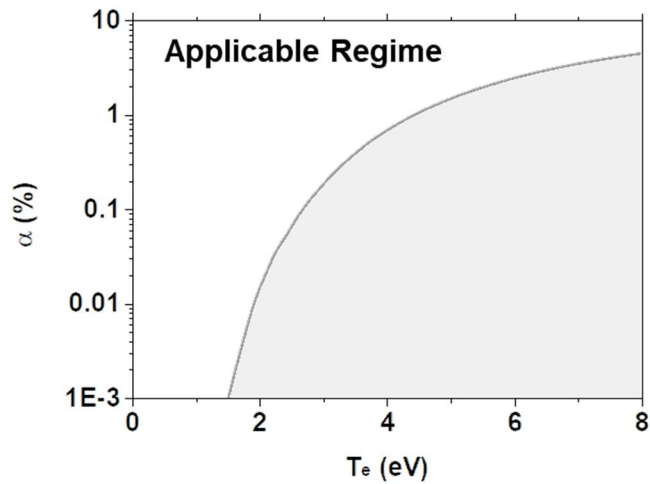


**Figure B- 19.** The applicable regime of the proposed model depending on  $\alpha$  and  $T_e$  of the plasma

## Bibliography

1. Khan, A. A., Moyne, J. R., & Tilbury, D. M. (2008). Virtual metrology and feedback control for semiconductor manufacturing processes using recursive partial least squares. *Journal of Process Control*, 18(10), 961-974.
2. Moyne, J. R., Hajj, H., Beatty, K., & Lewandowski, R. (2007). SEMI E133—The Process Control System Standard: Deriving a Software Interoperability Standard for Advanced Process Control in Semiconductor Manufacturing. *IEEE Transactions on Semiconductor Manufacturing*, 20(4), 408-420.
3. Lin, T. H., Hung, M. H., Lin, R. C., & Cheng, F. T. (2006, May). A virtual metrology scheme for predicting CVD thickness in semiconductor manufacturing. In *Robotics and Automation, 2006. ICRA 2006. Proceedings 2006 IEEE International Conference on* (pp. 1054-1059). IEEE.
4. Lynn, S. A., Ringwood, J., & MacGearailt, N. (2012). Global and local virtual metrology models for a plasma etch process. *IEEE Transactions on Semiconductor Manufacturing*, 25(1), 94-103.
5. Khan, A. A., Moyne, J. R., & Tilbury, D. M. (2007). An approach for factory-wide control utilizing virtual metrology. *IEEE Transactions on semiconductor Manufacturing*, 20(4), 364-375.
6. Ragnoli, E., McLoone, S., Lynn, S., Ringwood, J., & Macgearailt, N. (2009, May). Identifying key process characteristics and predicting etch rate from high-dimension datasets. In *Advanced Semiconductor Manufacturing Conference, 2009. ASMC'09. IEEE/SEMI* (pp. 106-111). IEEE.

7. Zeng, D., & Spanos, C. J. (2009). Virtual metrology modeling for plasma etch operations. *IEEE Transactions on Semiconductor Manufacturing*, 22(4), 419-431.
8. Kang, S., Kim, D., & Cho, S. (2016). Efficient feature selection-based on random forward search for virtual metrology modeling. *IEEE Transactions on Semiconductor Manufacturing*, 29(4), 391-398.
9. Chen, R., Huang, H., Spanos, C. J., & Gatto, M. (1996). Plasma etch modeling using optical emission spectroscopy. *Journal of Vacuum Science & Technology A: Vacuum, Surfaces, and Films*, 14(3), 1901-1906.
10. Kim, B., & Kim, S. (2004). Partial diagnostic data to plasma etch modeling using neural network. *Microelectronic engineering*, 75(4), 397-404.
11. Hong, S. J., May, G. S., & Park, D. C. (2003). Neural network modeling of reactive ion etching using optical emission spectroscopy data. *IEEE Transactions on Semiconductor Manufacturing*, 16(4), 598-608.
12. White, D. A., Boning, D., Butler, S. W., & Barna, G. G. (1997). Spatial characterization of wafer state using principal component analysis of optical emission spectra in plasma etch. *IEEE Transactions on Semiconductor Manufacturing*, 10(1), 52-61.
13. Card, J. P., Naimo, M., & Ziminsky, W. (1998). Run-to-run process control of a plasma etch process with neural network modelling. *Quality and Reliability Engineering International*, 14(4), 247-260.
14. Seni, G., & Elder, J. F. (2010). Ensemble methods in data mining: improving accuracy through combining predictions. *Synthesis Lectures on Data Mining and Knowledge Discovery*, 2(1), 1-126.
15. Park, S., Jeong, S., Jang, Y., Ryu, S., Roh, H. J., & Kim, G. H. (2015). Enhancement of the Virtual Metrology Performance for Plasma-Assisted Oxide Etching Processes

- by Using Plasma Information (PI) Parameters. *IEEE Transactions on Semiconductor Manufacturing*, 28(3), 241-246.
16. Spitzlsperger, G., Schmidt, C., Ernst, G., Strasser, H., & Speil, M. (2005). Fault detection for a via etch process using adaptive multivariate methods. *IEEE Transactions on Semiconductor Manufacturing*, 18(4), 528-533.
  17. Park, S. (2015). *Development of Plasma Information Based Virtual Metrology (PI-VM) for Plasma-assisted Processes*(Doctoral dissertation, Seoul National University).
  18. Godfrey, A. R., Ullal, S. J., Braly, L. B., Edelberg, E. A., Vahedi, V., & Aydil, E. S. (2001). New diagnostic method for monitoring plasma reactor walls: Multiple total internal reflection Fourier transform infrared surface probe. *Review of Scientific Instruments*, 72(8), 3260-3269.
  19. Kim, J. Y., & Chung, C. W. (2015). Real-time dielectric-film thickness measurement system for plasma processing chamber wall monitoring. *Review of Scientific Instruments*, 86(12), 123502.
  20. Bleakie, A., & Djurdjanovic, D. (2016). Growing Structure Multiple Model System for Quality Estimation in Manufacturing Processes. *IEEE Transactions on Semiconductor Manufacturing*, 29(2), 79-97.
  21. Suresh, S., & Sundaramoorthy, S. (2014). *Green Chemical Engineering: An introduction to catalysis, kinetics, and chemical processes*. CRC Press.
  22. Roh, H. J., Kim, N. K., Ryu, S., Jang, Y., & Kim, G. H. (2017). Optical diagnostics for the highly populated tail of an electron energy distribution function in very-high-frequency capacitively coupled plasma using spin-and dipole-forbidden lines. *Journal of Physics D: Applied Physics*, 50(22), 225201.

23. Kourti, T. (2005). Application of latent variable methods to process control and multivariate statistical process control in industry. *Int. J. Adapt. Contr. Signal Process*, 19(4), 213–246.
24. *Multivariate Data Analysis and Modelling Basic Course* (2002). Retrived from [http://metabolomics.se/Courses/MVA/MVA\\_Basic\\_Handouts\\_Exercises\\_Solutions\\_Mon-Tue.pdf](http://metabolomics.se/Courses/MVA/MVA_Basic_Handouts_Exercises_Solutions_Mon-Tue.pdf).
25. Cheng, F. T., & Chiu, Y. C. (2013). Applying the automatic virtual metrology system to obtain tube-to-tube control in a PECVD tool. *IIE Transactions*, 45(6), 670-681.
26. Cooper, J. (1966). Plasma spectroscopy. *Reports on Progress in Physics*, 29(1), 35.
27. Griem, H. R. (2005). *Principles of plasma spectroscopy* (Vol. 2). Cambridge University Press.
28. Oh, C., Ryoo, H., Lee, H., Kim, S. Y., Yi, H. J., & Hahn, J. W. (2010). Spatially resolvable optical emission spectrometer for analyzing density uniformity of semiconductor process plasma. *Review of Scientific Instruments*, 81(10), 103109.
29. Kim, I. J., & Yun, I. (2016). Plasma Process Uniformity Diagnosis Technique Using Optical Emission Spectroscopy With Spatially Resolved Ring Lens. *IEEE Transactions on Industrial Electronics*, 63(9), 5674-5681.
30. Fantz, U. (2006). Basics of plasma spectroscopy. *Plasma sources science and technology*, 15(4), S137.
31. Kunze, H. J. (2009). *Introduction to plasma spectroscopy* (Vol. 56). Springer Science & Business Media.
32. Van der Mullen, J. A. M. (1990). Excitation equilibria in plasmas; a classification. *Physics Reports*, 191(2-3), 109-220.
33. Lieberman, M. A., & Lichtenberg, A. J. (2005). *Principles of plasma discharges and materials processing*. John Wiley & Sons.

34. Kim, T. W., & Aydil, E. S. (2003). Effects of chamber wall conditions on Cl concentration and Si etch rate uniformity in plasma etching reactors. *Journal of The Electrochemical Society*, 150(7), G418-G427.
35. Cunge, G., Pelissier, B., Joubert, O., Ramos, R., & Maurice, C. (2005). New chamber walls conditioning and cleaning strategies to improve the stability of plasma processes. *Plasma Sources Science and Technology*, 14(3), 599.
36. Cunge, G., Kogelschatz, M., Joubert, O., & Sadeghi, N. (2005). Plasma-wall interactions during silicon etching processes in high-density HBr/Cl<sub>2</sub>/O<sub>2</sub> plasmas. *Plasma Sources Science and Technology*, 14(2), S42.
37. Cunge, G., Vempaire, D., Ramos, R., Touzeau, M., Joubert, O., Bodard, P., & Sadeghi, N. (2010). Radical surface interactions in industrial silicon plasma etch reactors. *Plasma Sources Science and Technology*, 19(3), 034017.
38. Agarwal, A., & Kushner, M. J. (2008). Seasoning of plasma etching reactors: Ion energy distributions to walls and real-time and run-to-run control strategies. *Journal of Vacuum Science & Technology A: Vacuum, Surfaces, and Films*, 26(3), 498-512.
39. Tinck, S., Boullart, W., & Bogaerts, A. (2011). Modeling Cl<sub>2</sub>/O<sub>2</sub>/Ar inductively coupled plasmas used for silicon etching: effects of SiO<sub>2</sub> chamber wall coating. *Plasma Sources Science and Technology*, 20(4), 045012.
40. Tinck, S., De Schepper, P., & Bogaerts, A. (2013). Numerical Investigation of Si O<sub>2</sub> Coating Deposition in Wafer Processing Reactors with Si C l<sub>4</sub>/O<sub>2</sub>/A r Inductively Coupled Plasmas. *Plasma Processes and Polymers*, 10(8), 714-730.
41. Schubert, E. F. (2004). Refractive index and extinction coefficient of materials. *Refractive index and extinction coefficient of materials*.
42. Gilmore, F. R., Laher, R. R., & Espy, P. J. (1992). Franck-Condon factors, r<sup>□</sup> centroids, electronic transition moments, and Einstein coefficients for many nitrogen

- and oxygen band systems. *Journal of physical and chemical reference data*, 21(5), 1005-1107.
43. Chamberlain, J. W. (2016). *Physics of the Aurora and Airglow: International Geophysics Series* (Vol. 2). Elsevier.
  44. High-resolution electron-impact emission spectra and vibrational emission cross sections from 330-1100 nm for N<sub>2</sub>. *The Astrophysical Journal Supplement Series*, 196(1), 13.
  45. Kubacki, R. M. (1995). Low temperature plasma deposition of silicon nitride to produce ultra-reliable, high performance, low cost sealed chip-on-board (SCOB) assemblies. *IEEE Transactions on Components, Packaging, and Manufacturing Technology: Part A*, 18(3), 471-477.
  46. Sanders, T. J., Caraway, E. L., Hall, C., Linn, J. H., Adkins, C., Deju, H., & Buschor, T. (1997, July). Silicon nitride deposition process for low cost microelectronics applications. In *University/Government/Industry Microelectronics Symposium, 1997., Proceedings of the Twelfth Biennial* (pp. 173-176). IEEE.
  47. Czerwicz, T., Greer, F., & Graves, D. B. (2005). Nitrogen dissociation in a low pressure cylindrical ICP discharge studied by actinometry and mass spectrometry. *Journal of Physics D: Applied Physics*, 38(24), 4278.
  48. Tao, K., Mao, D., & Hopwood, J. (2002). Ionized physical vapor deposition of titanium nitride: A global plasma model. *Journal of applied physics*, 91(7), 4040-4048.
  49. Niimi, H., & Lucovsky, G. (1999). Monolayer-level controlled incorporation of nitrogen in ultrathin gate dielectrics using remote plasma processing: Formation of stacked “N–O–N” gate dielectrics. *Journal of Vacuum Science & Technology B*:

*Microelectronics and Nanometer Structures Processing, Measurement, and Phenomena*, 17(6), 2610-2621.

50. Zhu, X. M., & Pu, Y. K. (2010). Optical emission spectroscopy in low-temperature plasmas containing argon and nitrogen: determination of the electron temperature and density by the line-ratio method. *Journal of Physics D: Applied Physics*, 43(40), 403001.
51. Bibinov, N. K., Kokh, D. B., Kolokolov, N. B., Kostenko, V. A., Meyer, D., Vinogradov, I. P., & Wiesemann, K. (1998). A comparative study of the electron distribution function in the positive columns in and/He dc glow discharges by optical spectroscopy and probes. *Plasma Sources Science and Technology*, 7(3), 298.
52. Kozlov, K. V., Wagner, H. E., Brandenburg, R., & Michel, P. (2001). Spatio-temporally resolved spectroscopic diagnostics of the barrier discharge in air at atmospheric pressure. *Journal of Physics D: Applied Physics*, 34(21), 3164.
53. Lebedev, Y. A., & Shakhatov, V. A. (2006). Diagnostics of a nonequilibrium nitrogen plasma from the emission spectra of the second positive system of N<sub>2</sub>. *Plasma Physics Reports*, 32(1), 56-71.
54. Isola, L. M., Gómez, B. J., & Guerra, V. (2009). Determination of the electron temperature and density in the negative glow of a nitrogen pulsed discharge using optical emission spectroscopy. *Journal of Physics D: Applied Physics*, 43(1), 015202.
55. Bernath, P. F. (2002). Electronic spectroscopy of diatomic molecules. *Handbook of Molecular Physics and Quantum Chemistry*, Wiley.
56. Šimek, M. (2014). Optical diagnostics of streamer discharges in atmospheric gases. *Journal of Physics D: Applied Physics*, 47(46), 463001.

57. Laporta, V., Little, D. A., Celiberto, R., & Tennyson, J. (2014). Electron-impact resonant vibrational excitation and dissociation processes involving vibrationally excited N<sub>2</sub> molecules. *Plasma Sources Science and Technology*, 23(6), 065002.
58. Annaloro, J., Bultel, A., & Omaly, P. (2014). Collisional-radiative modeling behind shock waves in nitrogen. *Journal of Thermophysics and Heat Transfer*, 28(4), 608-622.
59. Teulet, P., Sarrette, J. P., & Gomes, A. M. (1999). Calculation of electron impact inelastic cross sections and rate coefficients for diatomic molecules. Application to air molecules. *Journal of Quantitative Spectroscopy and Radiative Transfer*, 62(5), 549-569.
60. Kurnosov, A. K., Napartovich, A. P., Shnyrev, S. L., & Cacciatore, M. (2010). A database for V–V state-to-state rate constants in N<sub>2</sub>–N<sub>2</sub> and N<sub>2</sub>–CO collisions in a wide temperature range: dynamical calculations and analytical approximations. *Plasma Sources Science and Technology*, 19(4), 045015.
61. Thorsteinsson, E. G., & Gudmundsson, J. T. (2009). A global (volume averaged) model of a nitrogen discharge: I. Steady state. *Plasma Sources Science and Technology*, 18(4), 045001.
62. Marinov, D., Guaitella, O., de los Arcos, T., Von Keudell, A., & Rousseau, A. (2014). Adsorption and reactivity of nitrogen atoms on silica surface under plasma exposure. *Journal of Physics D: Applied Physics*, 47(47), 475204.
63. Guerra, V., Sá, P. A., & Loureiro, J. (2004). Kinetic modeling of low-pressure nitrogen discharges and post-discharges. *The European Physical Journal-Applied Physics*, 28(2), 125-152.
64. Simek, M., DeBenedictis, S., Dilecce, G., Babický, V., Clupek, M., & Sunka, P. (2002). Time and space resolved analysis of N<sub>2</sub> (C 3Π<sub>u</sub>) vibrational distributions in

- pulsed positive corona discharge. *Journal of Physics D: Applied Physics*, 35(16), 1981.
65. Annušová, A., Foissac, C., Krištof, J., Veis, P., & Supiot, P. (2012). Spectroscopic diagnostics and modelling of a N<sub>2</sub>–Ar mixture discharge created by an RF helical coupling device: II. Vibrational distribution of the N<sub>2</sub> (C 3Π<sub>u</sub>, v') state. *Plasma Sources Science and Technology*, 21(5), 055022.
  66. Cacciatore, M., Kurnosov, A., & Napartovich, A. (2005). Vibrational energy transfer in N<sub>2</sub>–N<sub>2</sub> collisions: A new semiclassical study. *The Journal of chemical physics*, 123(17), 174315.
  67. Gordiets, B., Ferreira, C. M., Pinheiro, M. J., & Ricard, A. (1998). Self-consistent kinetic model of low-pressure-flowing discharges: I. Volume processes. *Plasma Sources Science and Technology*, 7(3), 363.
  68. Kim, H. J., & Lee, H. J. (2016). 2D fluid model analysis for the effect of 3D gas flow on a capacitively coupled plasma deposition reactor. *Plasma Sources Science and Technology*, 25(3), 035006.
  69. Benoit, D., Morin, P., & Regolini, J. (2011). Determination of silicon nitride film chemical composition to study hydrogen desorption mechanisms. *Thin Solid Films*, 519(19), 6550-6553.
  70. Pitchford, L. C., Alves, L. L., Bartschat, K., Biagi, S. F., Bordage, M. C., Bray, I., ... & Chaudhury, B. (2017). LXCat: an Open Access, Web Based Platform for Data Needed for Modeling Low Temperature Plasmas. *Plasma Processes and Polymers*, 14(1-2).
  71. Kondo, M., & Matsuda, A. (2002). An approach to device grade amorphous and microcrystalline silicon thin films fabricated at higher deposition rates. *Current Opinion in Solid State and Materials Science*, 6(5), 445-453.

72. Kim, Y. C., & Boudant, M. (1991). recombination of O, N, and H atoms as Silica: Kinetics and mechanism, *hagemuir*, 7, 2999-3005 (1991), and L. Robbin Martin," Diamond film growth in a flowtube: A temperature: A temperature dependance study. *J. Appl. Phys*, 70, 5667-5674.
73. Boffard, J. B., Lin, C. C., & DeJoseph Jr, C. A. (2004). Application of excitation cross sections to optical plasma diagnostics. *Journal of Physics D: Applied Physics*, 37(12), R143.
74. *Argon energy level diagram*. Retrived from [raptor.physics.wisc.edu/data/Ar\\_energy.pdf](http://raptor.physics.wisc.edu/data/Ar_energy.pdf)
75. *Atomic and molecular spectroscopy*. Retrived from [mackenzie.chem.ox.ac.uk/teaching.html](http://mackenzie.chem.ox.ac.uk/teaching.html)
76. Drawin, H. W. (1977). HW Drawin and F. Emard, *Physica C* 85, 333 (1977). *Physica C*, 85, 333.
77. Behringer, K., & Fantz, U. (1994). Spectroscopic diagnostics of glow discharge plasmas with non-Maxwellian electron energy distributions. *Journal of Physics D: Applied Physics*, 27(10), 2128.
78. Schulze, J., Heil, B. G., Luggenhölscher, D., Brinkmann, R. P., & Czarnetzki, U. (2008). Stochastic heating in asymmetric capacitively coupled RF discharges. *Journal of Physics D: Applied Physics*, 41(19), 195212.
79. Boffard, J. B., Chiaro, B., Weber, T., & Lin, C. C. (2007). Electron-impact excitation of argon: Optical emission cross sections in the range of 300–2500 nm. *Atomic Data and Nuclear Data Tables*, 93(6), 831-863.
80. Kramida, A., Ralchenko, Y., & Reader, J. (2016). Team: NIST Atomic Spectra Database (version 5.4) [<http://physics.nist.gov/asd>]. National Institute of Standards and Technology, Gaithersburg.

81. Irons, F. E. (1979). The escape factor in plasma spectroscopy—I. The escape factor defined and evaluated. *Journal of Quantitative Spectroscopy and Radiative Transfer*, 22(1), 1-20.
82. Li, J., Liu, F. X., Zhu, X. M., & Pu, Y. K. (2011). The spatially resolved measurements of the atomic densities in argon Paschen 1s levels by OES in a capacitively coupled plasma. *Journal of Physics D: Applied Physics*, 44(29), 292001.
83. Cheng, Z. W., Zhu, X. M., Liu, F. X., & Pu, Y. K. (2014). Determination of the rate coefficients of the electron-impact excitation from the metastable states to 2p states of argon by the emission line ratios in an afterglow plasma. *Journal of Physics D: Applied Physics*, 47(27), 275203.
84. Cheng, Z. W., Zhu, X. M., Liu, F. X., & Pu, Y. K. (2015). Determination of the rate coefficient of the electron-impact excitation from the argon resonance states (1s2 and 1s4) to 2p states by the emission line ratio in an afterglow plasma. *Plasma Sources Science and Technology*, 24(2), 025025.
85. Cheng, Z. W., Zhu, X. M., Sadeghi, N., Guo, X. M., Liu, F. X., & Pu, Y. K. (2015). Measurement of the electron-impact excitation rate coefficients from argon 1s states to 3p states. *Journal of Physics D: Applied Physics*, 48(28), 285202.
86. Boffard, J. B., Jung, R. O., Lin, C. C., Aneskavich, L. E., & Wendt, A. E. (2011). Optical diagnostics for characterization of electron energy distributions: argon inductively coupled plasmas. *Plasma Sources Science and Technology*, 20(5), 055006.
87. Boffard, J. B., Jung, R. O., Lin, C. C., & Wendt, A. E. (2010). Optical emission measurements of electron energy distributions in low-pressure argon inductively coupled plasmas. *Plasma Sources Science and Technology*, 19(6), 065001.

88. Donnelly, V. M. (2004). Plasma electron temperatures and electron energy distributions measured by trace rare gases optical emission spectroscopy. *Journal of Physics D: Applied Physics*, 37(19), R217.
89. Gangwar, R. K., Srivastava, R., & Stauffer, A. D. (2013). Collisional-radiative model for non-Maxwellian inductively coupled argon plasmas using detailed fine-structure relativistic distorted-wave cross sections. *The European Physical Journal D*, 67(10), 203.
90. Zhu, X. M., Chen, W. C., Li, J., Cheng, Z. W., & Pu, Y. K. (2012). Spatial evolution of the electron energy distribution function in a low-pressure capacitively coupled plasma containing argon and krypton. *Plasma Sources Science and Technology*, 21(4), 045009.
91. Godyak, V. A., & Demidov, V. I. (2011). Probe measurements of electron-energy distributions in plasmas: what can we measure and how can we achieve reliable results?. *Journal of Physics D: Applied Physics*, 44(23), 233001.
92. Wilczek, S., Trieschmann, J., Schulze, J., Schuengel, E., Brinkmann, R. P., Derzsi, A., ... & Mussenbrock, T. (2015). The effect of the driving frequency on the confinement of beam electrons and plasma density in low-pressure capacitive discharges. *Plasma Sources Science and Technology*, 24(2), 024002.
93. Liu, Y. X., Zhang, Q. Z., Jiang, W., Hou, L. J., Jiang, X. Z., Lu, W. Q., & Wang, Y. N. (2011). Collisionless bounce resonance heating in dual-frequency capacitively coupled plasmas. *Physical review letters*, 107(5), 055002.
94. Liu, Y. X., Zhang, Q. Z., Jiang, W., Lu, W. Q., & Wang, Y. N. (2012). Experimental validation and simulation of collisionless bounce-resonance heating in capacitively coupled radio-frequency discharges. *Plasma Sources Science and Technology*, 21(3), 035010.

95. Zhenhua, B., Xiang, X., Yongxin, L., Xiangzhan, J., Wenqi, L., & Younian, W. (2011). Comparison of 2D Hybrid Simulational and Experimental Results for Dual-Frequency Capacitively Coupled Argon Plasmas. *Plasma Science and Technology*, 13(2), 181.

## 초 록

가상 계측 방법론(VM)은 웨이퍼의 공정 결과의 전수 조사를 가능하게 하므로 반도체 제조용 플라즈마 공정의 선행공정제어 (APC)를 위해 필수적이다. VM은 이전 스텝의 웨이퍼 상태 변수와 현 스텝의 공정 변수 (장비 변수, 센서 변수)를 통해 현 스텝의 웨이퍼 공정 결과를 예측하는 기술이다. 그러나 VM의 예측 신뢰도는 사용되는 데이터의 질과 데이터 마이닝 기술에 따라 매우 민감하여 APC 활용에 한계가 존재한다. 또한 반도체 소자의 선폭이 감소함에 따라 VM에 요구되는 예측 신뢰도가 증가하고 있어, 플라즈마 반응기의 정보를 포함할 수 있는 현상학 기반의 VM 개발이 필요하다.

플라즈마를 활용한 웨이퍼의 공정 결과는 반응종 (라디칼, 준안정종, 이온 등)의 웨이퍼로의 입자속에 의해 결정된다. 이 반응종들은 전자-충돌 반응에 의해 생성되고, 벽면에서의 반응에 의해 소멸된다. 따라서 웨이퍼 공정 결과는 플라즈마 내 반응율을 결정하는 전자에너지분포함수 (EEDF)와 벽면 반응을 지배하는 반응기 벽면 상태의 영향을 받는다.

플라즈마 공정은 운전 시간이 증가함에 따라 벽면에 쌓이는 불순물 등이 유발하는 현상에 의해 표류 (drift) 하게 된다. 이 벽면 상태의 표류는 벽면에서의 탈착 또는 반응종의 벽면에서의 손실율을 변화시킴으로써 반응종의 입자속에 영향을 미친다. 또한 반응기 벽면 상태의 표류는 플라즈마 내 가스 조성을 변화시킴으로써 EEDF의 변화를 야기시킨다. 변화된 EEDF는 반응종의 입자속에 추가적인 변화를 유발하게 된다. 따라서 신뢰성 있는 VM의 개발을 위해서는 EEDF와 반응기 벽면 상태를 변수로 포함하는 모델 개발이 필요하다.

플라즈마 정보 (PI) 변수는 반응종의 입자속에 영향을 미치는 플라즈마 공정

의 상태변수로 정의된다.  $PI_{Wall}$ 은 장비 벽면의 상태를 모니터링하는 변수으로써 반응기 내벽에 증착되는 박막의 두께를 의미한다.  $PI_{Volume}$ 은 전자밀도와 전자온도로 정의되어 플라즈마의 전자-충돌 반응을 나타낸다. PI 변수들은 플라즈마에서 방출된 빛을 여기 평형 상태를 기반으로 해석하는 플라즈마 분광학 (plasma spectroscopy)를 통해 결정된다.  $PI_{Wall}$ 은 동일한 에너지 준위에서 방출되는 서로 다른 파장의 세기 비율을 기반으로 시창구의 투과도를 해석함으로써 결정한다. 시창구에 쌓이는 박막 증착은 장비 벽면에 쌓이는 박막 증착과 양의 상관관계가 있음을 가정하였다.  $PI_{Volume}$ 은 충돌-방사 천이 모델 (CRM)을 기반으로 서로 다른 에너지 준위에서 방출되는 파장의 세기 비율을 해석함으로써 결정되었다.

단일 박막 질화막 PECVD의 공정 결과를 예측하는 PI-VM에서 각 PI 변수가 미치는 영향을 해석하여 실리콘 질화막 형성에서 PI 변수가 가지는 의미를 판단했다. 전자밀도는 낮은 활성화 에너지를 갖는 충돌 반응을 지배함으로써 플라즈마 내에 N을 포함하는 라디칼을 형성시킨다. 반면 전자온도는 높은 활성화 에너지를 갖는 충돌 반응을 지배함으로써 플라즈마 내에 Si를 포함하는 라디칼의 양을 증가시킨다. 벽면 상태는 벽면 근처에서 N을 포함하는 라디칼을 증가시키며, 그 영향은 확산에 의해 플라즈마 내 평균적인 라디칼도 증가시킨다.

PI-VM의 실공정 적용 가능성을 판단하기 위해 3D-NAND 제조를 위한 실리콘 질화막/산화막의 다중 박막(layer) 증착공정에서 질화막 두께를 예측하기 위한 PI-VM을 구축했다. 구축된 PI-VM에서 각 인자의 영향도를 평가한 결과,  $PI_{Wall}$ 이 가장 큰 중요도를 가지며,  $PI_{Volume}$ 은 후기 박막 증착에서 중요한 영향을 미침을 확인했다. 소자의 밀도 증가를 위해 박막수가 증가하는 현 추세에서 PI-VM은 반도체 공정이 관리해야 할 핵심적인 플라즈마 현상을 제공할 수 있음을 확인했다. 따라서 PI-VM은 플라즈마 진단 기술에 속하는 플라즈마 분광학을 응용분야인 플라즈마 공정에 활용하는 방법론으로써 APC 및 결함 감지/분류 (FDC) 기술을 위한 기반 기술로 활용될 수 있을 것으로 기대된다.